Nanoscale carbon coating for Multipactor protection of RF equipment's embedded in satellites

Alejandro Buitrago Bernal

To cite this version:

Alejandro Buitrago Bernal. Nanoscale carbon coating for Multipactor protection of RF equipment's embedded in satellites. Electronics. Université de Bretagne occidentale - Brest, 2022. English. NNT : 2022BRES0071 . tel-04016284

HAL Id: tel-04016284

https://theses.hal.science/tel-04016284

Submitted on 6 Mar 2023

THESE DE DOCTORAT DE

L'UNIVERSITE
DE BRETAGNE OCCIDENTALE

ECOLE DOCTORALE N° 601
Mathématiques et Sciences et Technologies
de l'Information et de la Communication
Spécialité : *Electronique, Télécommunications*

Par
Alejandro BUITRAGO BERNAL

Revêtements carbones nanométriques pour la protection multipactor d'équipements RF embarqués dans les satellites

Nanoscale carbon coating for Multipactor protection of RF equipment's embedded in satellites

Thèse présentée et soutenue à Brest, le 26 octobre 2022
Unité de recherche Lab-STICC, UMR CNRS 6285

Rapporteurs avant soutenance :

Serge VERDEYME	Professeur des Universités, XLIM, CNRS UMR 7252
Eric KERHERVE	Professeur des Universités, IMS, CNRS UMR 5218

Composition du Jury :

Président :	Xavier CASTEL	Professeur des Universités, IETR, CNRS UMR 6164
Examinateurs :	Serge VERDEYME	Professeur des Universités, XLIM, CNRS UMR 7252
	Eric KERHERVE	Professeur des Universités, IMS, CNRS UMR 5218
	Damien PACAUD	Ingénieur Hyperfréquences, Thales Alenia Space France
	Mohamed BELHAJ	Ingénieur de Recherche, ONERA
	Jessica BENEDICTO	Maître de conférences, Lab-STICC, CNRS UMR 6285, UBO
Dir. de thèse :	Eric RIUS	Professeur des Universités, Lab-STICC, CNRS UMR 6285, UBO
Co-dir. de thèse :	Jean-François FAVENNEC	Maître de conférences, HDR, Lab-STICC, CNRS UMR 6285, ENIB

Invité :

Denis PAYAN	Expert Sénior Effets de Puissance RF, CNES

Acknowledgments

I would like to express my deepest appreciation to my advisors Eric Rius, Jean-François Favennec, and Jessica Benedicto for their support, patience, and feedback during these last years. It was a pleasure working with them. I must also thank the members of CNES, ONERA, Thales Alenia Space, and our Singaporean colleagues from NTU/CINTRA for their advice throughout the project.

I also want to thank current and past graduates, post-doctoral fellows, and professors at Lab-STICC who created an environment in which I was pleased to learn and work.

Finally, I want to thank my family, who without this would not have been possible. Their constant support helped me maintain my confidence and persistence until the last day.

Preamble

This thesis was funded by the Université de Bretagne Occidentale (UBO) and Région Bretagne. Ph.D. PhD has also benefited indirectly from an R&T project funded by the Centre National d'Études Spatiales (CNES).

CNES, ONERA, Thales Alenia, Space and our Singaporean colleagues from NTU/CINTRA also participated in this work.

Introduction

In the field of satellite telecommunications, the need for a high RF power transmission stage isa consequence of a more connected world, driven by an increase in the digital bit rates and number of users. The requirement increasing this transmission power is also accompanied by the requirement of more compact devices tor to reduce the size and weight of the satellites. For these components, the required electrical performances impose the need of high quality factors, in the order of several thousands, requiring the use of very large waveguide or volumetric technologies. Hence, size reduction becomes a permanent challenge for RF designers, since the constraints on quality factors and even more on power handling are a major obstacle to miniaturization.

As a result of these needs, the study of high-power phenomena, like the multipactor effect, inside the devices is crucial. The multipactor effect is manifested in the vacuum and under certain electromagnetic conditions, resulting in an electron discharge inside the RF devices. These discharges can damage the devices and the complete system, causing the satellite to be out of service. In a satellite, the most exposed components to this phenomenon are the ones of the communications stage between the satellite and the earth, in particular filters and multiplexers.

Then, the design of new RF components should include a power analysis and optimization of the potential power handling to accomplish the requirements. The inclusion of multipactor mitigation techniques in the design of these structures increases design time and adds a new degree of complexity to the structures since different approaches can be imagined. One of these approaches consists in the modification of the electrical properties of the metallic conductors, specifically the Secondary Emission Yield (SEY), impeding new electrons from being liberated and be part of the resulting electrons avalanche.

Recent studies have been initiated on the possibility of coating the metallic conductors of RF components with nanometric carbon layers as graphene or amorphous carbon. Preliminary results have shown that the use of these coatings helps to increase the maximum power that can be handled by microwave devices. The objective of this thesis is part of this study, since it involves evaluating what nanoscale carbon coatings can provide, in terms of protection against multipactor discharges and the consequences on the miniaturization of RF systems.

With the intention of presenting our results, this work is divided in 5 different chapters. In Chapter I, a state the art that includes a better description of the multipactor effect and different mitigation techniques is presented. Then, Chapter II presents the characterization of carbon coatings and an evaluation of their impact on electrical performances on a microwave filter. Chapter III presents the design, study and measurements of a microwave filter used for the determination of the impact of carbon coatings in in terms of power handling capabilities. Then, in Chapter IV a different solution is presented to increase the power handling of a microwave filter by proposing a novel $\lambda/4$ resonator topology. In addition, the potential of the carbon coatings is also studied, showing the interest of these coatings and the use of multiple strategies at the same time. Next, Chapter V presents a preliminary study in the use of dielectric fillings as an element of multipactor protection. First results are compared with the results on the previous chapters and future studies are proposed. Finally, the conclusions and perspective of this work are presented on the last section.

Chapter I : State of the art

I.1 Introduction

In this chapter, the state of the art of high-power satellite communication TX filters and multipactor effect on these components is presented. First, sections I.2 to I.3 expose the need of higher power on satellite communications and a brief description of the platform and the payload. Then, section I.4 presents the theory on multipactor effect, its main parameters and how to model it. Finally, in section I.5, multipactor mitigation techniques are presented and compared.

I.2 Satellite communications and new requirements

After Sputnik, the first satellite, launched in 1957, satellite communications and applications have evolved drastically. In modern satellite communication systems, the transmitter power is one of the variables that is increasing to improve the performance of novel and more complex coding and modulation schemes. The need of higher transmission rates is accompanied by the increase of the channel bandwidth, which is normally accomplished by using higher frequencies, as it is the case of High Throughput Satellites which have moved their operating band from Ku (12-18 GHz) to Ka (26.5-40 GHz) [1], [2], [3].

I.3 Architecture of a satellite communication system

A satellite communication system is divided in three main segments, control, ground, and space. The control segment consists of all the different ground facilities that participate in the control and monitoring of the satellite (including tracking and traffic management). The ground segments consist of all the different earth stations that can vary depending on the service or applications. Finally, the space segment is conformed by the single or multiple satellites in orbit [1].

I.3.1 Satellite architecture

The size and architecture of a satellite will depend on the mission it is conceived for, like communications, space or earth observation, global positioning systems... They can be classified in terms of weight from a few kilograms up to thousands of kilograms, they can have different sizes and shapes. A general classification of satellites by their mass is presented in Figure I.1.

Table I.1 Classification of satellites by mass [3]

Category	**Mass [kg]**
Large	>1000
Medium	500-1000
Mini	100-500
Micro	10-100
Nano	1-10
Pico	<1

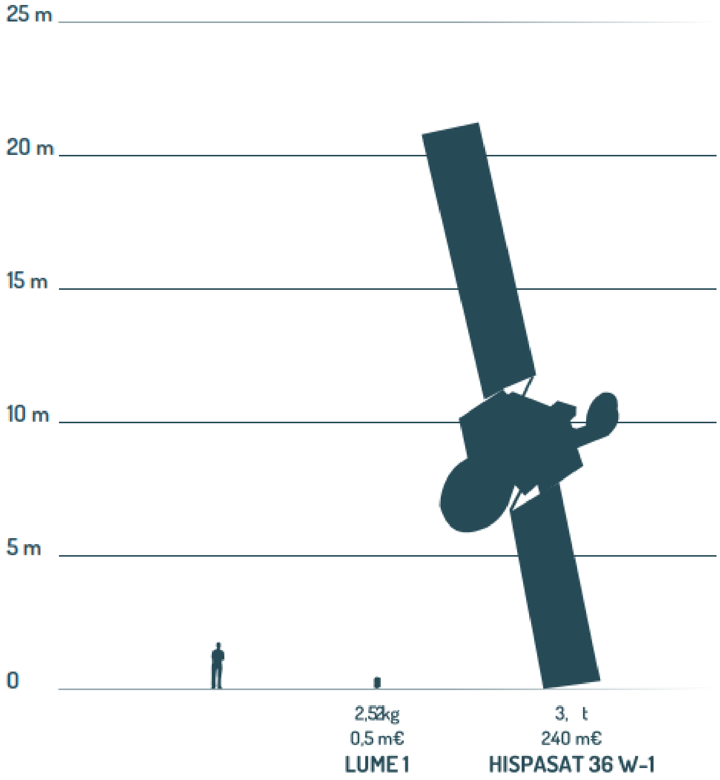

Figure I.1 satellites comparison. Taken from [4]

The actual price of sending something to space is around 10 000 euros per kg, taking this into account, depending on the specifications and mass, the cost of a conventional satellite can reach the value of 500 million euros without considering latter expense of maintaining and repairing. In the other hand, a nanosatellite can be built and placed in orbit for only 500 000 euros [3], being as reliable as other conventional satellites. Furthermore, this reduced price also implies that the risks in space missions are divided into smaller segments, and because of its size, it can be replaced easily without representing a big cost that could endanger the whole mission as it happens with big scale satellites.

I.3.1.a Platform and payload

The components of a satellite will depend on the function for which the satellite is designed, however, there are several components that are common in most satellites (platform). First, we have the antennas, used to receive and transmit signals to and from earth; a solar array to convert sunlight into energy generating the satellites power, the transponders (payload of telecommunications satellite) which provide the link between the receiving and transmitting antennas, a thermal control that protects satellite components against extreme temperature changes, the command and data handling system that control the satellites functions and operations also receiving commands from earth. Housing constructed from strong materials that can withstand the harsh space environment, and finally the guidance and stabilization system that ensure the right orbit and that is orientated forward to its correct target, this is possible due to the sensor monitor and the use of thrusters to maintain the ideal position and orientation. All these parts and its placement in a satellite are shown in Figure I.2.

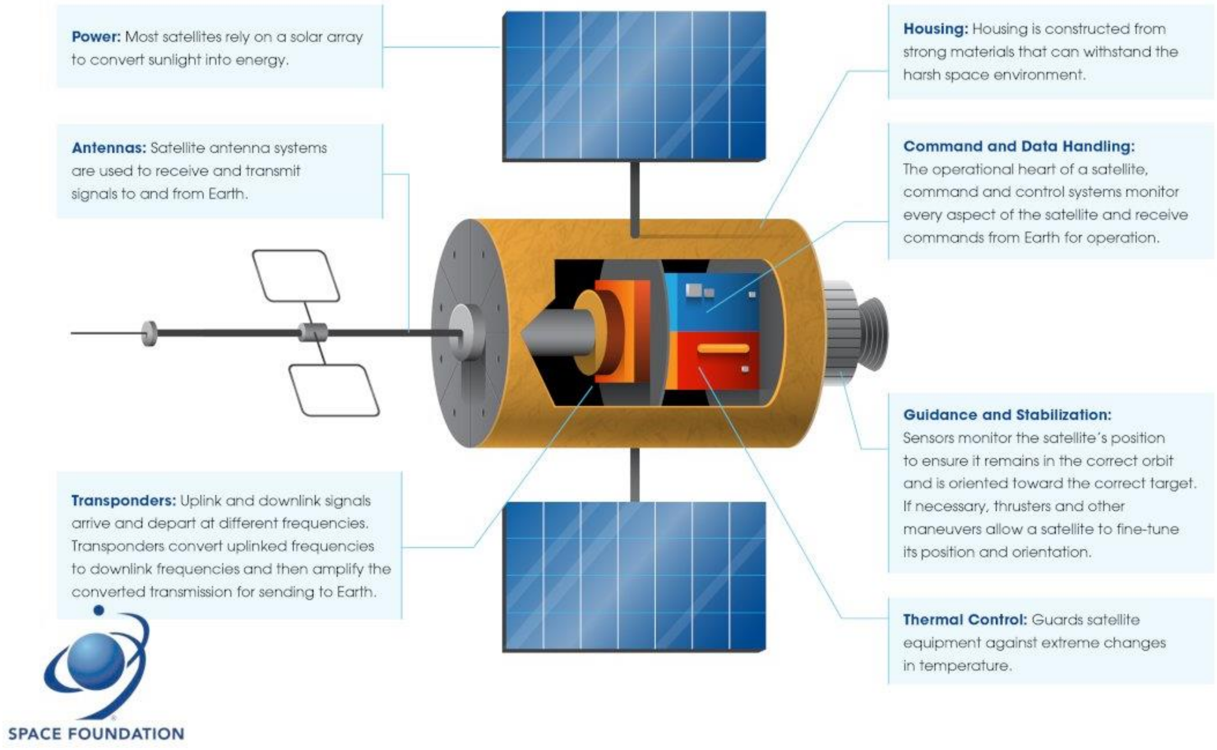

Power: Most satellites rely on a solar array to convert sunlight into energy.

Antennas: Satellite antenna systems are used to receive and transmit signals to and from Earth.

Transponders: Uplink and downlink signals arrive and depart at different frequencies. Transponders convert uplinked frequencies to downlink frequencies and then amplify the converted transmission for sending to Earth.

Housing: Housing is constructed from strong materials that can withstand the harsh space environment.

Command and Data Handling: The operational heart of a satellite, command and control systems monitor every aspect of the satellite and receive commands from Earth for operation.

Guidance and Stabilization: Sensors monitor the satellite's position to ensure it remains in the correct orbit and is oriented toward the correct target. If necessary, thrusters and other maneuvers allow a satellite to fine-tune its position and orientation.

Thermal Control: Guards satellite equipment against extreme changes in temperature.

Figure I.2 Components of a satellite. Taken from [5]

I.3.1.b Tx Filters

In the communication module, the architecture has two transmission links, the uplink and the downlink. The uplink chain (Rx) is the transmission between the earth and the satellite, consisting of highly sensitive equipment but working at low power. On the other hand, the downlink chain (Tx) is the transmission between the satellite and the earth. In this stage, a high transmission power is required to send the signals to the earth.

As an example, additional to the demanding electrical performance constraint, physical dimensions of new Radio Frequency components are an important design constraint. Figure I.3 shows two compact filters in the C and Ku bands for space applications. The need for compact structures is also related to the cost of launching satellites into space, where not also size but weight should be minimized.

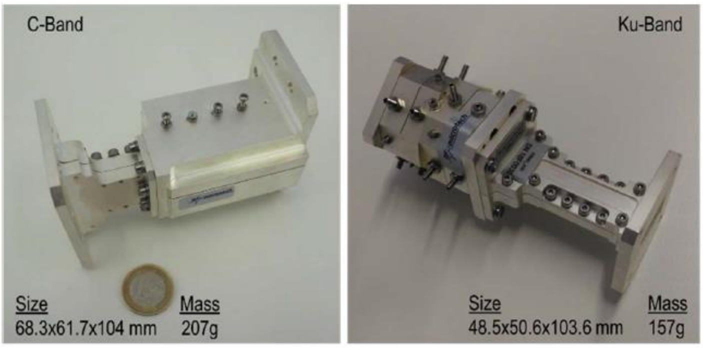

Figure I.3 C and Ku band filters in [2]

The combination of size and weight reductions, together with the increase of transmitted power, implies higher electromagnetic fields inside the structures, leading to power handling limitations. Therefore, power handling of a RF component can be a limiting factor of the system performance [2], [6]. Unfortunately, power limitations are not always considered as a primary constraint in the design of new hardware. As reported in [7], around 50% of new equipment fails to reach the specified power requirements for space applications.

I.4 Multipactor effect

The Multipactor effect is an electron discharge that occurs in vacuum. Under determined conditions of electromagnetic power and frequency, a free electron gets accelerated and synchronized with an electric field ($\bar{E}$). When this primary electron impacts against a wall with an energy enough to release more than one secondary electron from the wall, they can start a chain reaction leading to an exponential growth of the electron population (electron avalanche) [8]. The maximum working power of a microwave component will be limited by the power at which the discharge will occur.

Although this effect can occur in a single or double surface configuration, it is often described as a two-surface event [9]. Figure I.4 presents a double surface Multipactor avalanche occurring between two parallel plates separated by a distance d. Between time $t = t_0$ and $t = t_n$ a free electron could oscillate between both metallic walls in synchrony with the RF field but without enough energy to release new electrons. Then at $t = t_{n+1}$ this electron will hit one metallic wall with enough energy that it releases two secondary electrons that will start an avalanche releasing each of them two new electrons as they impact the opposite wall as it can be seen on $t = t_{n+2}$.

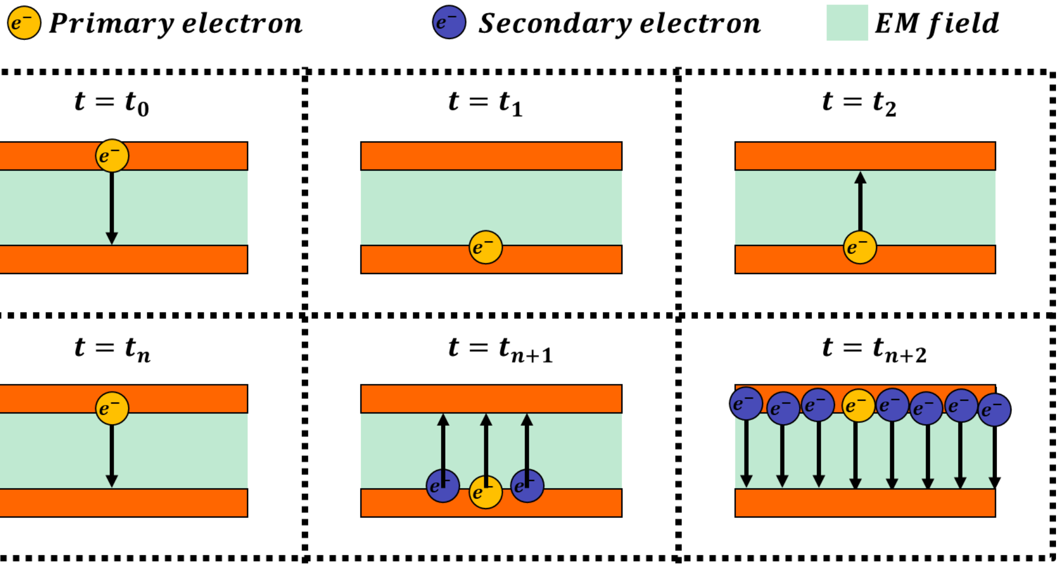

Figure I.4 Double surface Multipactor representation over time

Multipactor can occur in a wide variety of systems and applications like RF and microwave components, klystrons, magnetrons, particle accelerators, and vacuum tubes. In RF components, a multipactor discharge can be the cause of different harmful effects like:

- Heating of the device
- Quality factor degradation
- Increase of the reflected power
- Increase of noise floor
- Detuning of resonant cavities
- Physical damages (erosion as presented in Figure I.5)

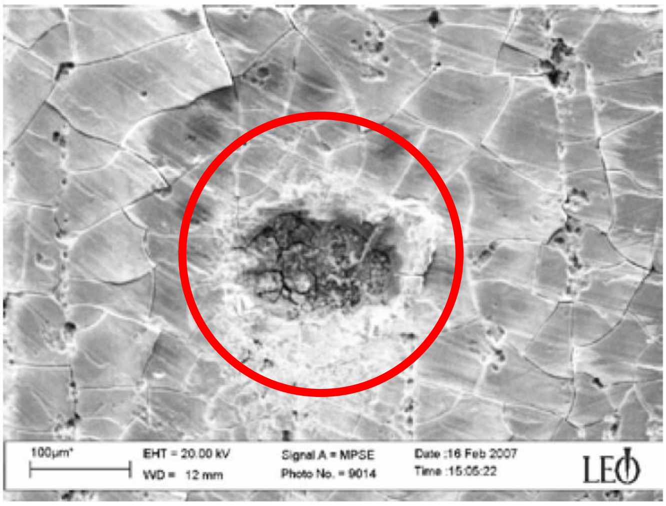

Figure I.5 Surface micro-erosion caused by a multipactor discharge [7]

Over the last years, different solutions have been proposed to prevent this effect on board of satellites. Despite the advances in this domain, the multipactor effect is still a concern. The exponential growth in the demand of high transmitted power from space to earth and the shift of applications to higher frequency bands are adding new challenges in the mitigation of this phenomenon.

I.4.1 Theory

Multipactor effect is directly coupled to the frequency of the Radio Frequency (RF) field, the geometry of the structure, and the intrinsic properties of the walls' material.

I.4.1.a Equation of motion between parallel plates

As mentioned before, the simplest case of multipactor is a discharge between two parallel plates with the same electrical properties, separated by a distance (d) and with an RF field $(V_{RF}\sin(\omega t))$ between them. With a RF peak voltage (V_{RF}) at given pulsation (ω). In this section, the equations of movement for multipactor are presented. Inside a known electromagnetic field, the movement of an electron is governed by the Lorentz force, and an equation of movement for the electron can be determined. From it, an expression for the velocity of an electron released from one of the surfaces is obtained:

$$v = \frac{e\,V_{RF}}{m\omega d}[\cos(\alpha) - \cos(\omega t)] + v_0 \qquad \text{(I-1)}$$

where:

e: electron charge

m: electron mass

α: phase of the RF field at which the electron is released

v_0: velocity at which the electron is released

d: separation distance between the plates

By the integration of (I-1), the expression of the position (s) of the electron is obtained, which leads to:

$$s = \frac{e\,V_{RF}}{m\omega^2 d}\left[(\omega t - \alpha)\cos(\alpha) - \sin(\omega t) + \sin(\alpha)\right] + \frac{v_0}{\omega}(\omega t - \alpha) \tag{I-2}$$

Considering that the electron must be synchronized with the RF field, the time for the electron to go from one surface to another is N half cycles of the field, also known as multipactor order (with N being odd). When the electron impacts the second wall, its phase will be:

$$\omega t = N\pi + \alpha \tag{I-3}$$

Using (I-3), and at the distance s=d, (I-2) is expressed as:

$$d = \frac{e\,V_{RF}}{m\omega^2 d}\left[N\pi\cos(\alpha) + 2\sin(\alpha)\right] + \frac{v_0}{\omega}(N\pi) \tag{I-4}$$

which leads to an expression of the fields' voltage:

$$V_{RF} = \frac{m\omega d\,(\omega d - N\pi v_0)}{e(N\pi\cos(\alpha) + 2\sin(\alpha))} \tag{I-5}$$

Also, when using the collision conditions in (I-1), the impact velocity of the electron (v_i) is determined by:

$$v_i = \frac{2e\,V_{RF}}{m\omega d}\cos(\alpha) + v_0 \tag{I-6}$$

Finally, using (I-5) and (I-6) the impact velocity (v_i) of a primary electron on a metallic wall can be defined as:

$$v_i = \frac{2(\omega d - N\pi v_0)\,cos(\alpha)}{N\pi\cos(\alpha) + 2\sin(\alpha)} + v_0 \tag{I-7}$$

This velocity is related to an equivalent voltage between both walls (V_i)

$$V_i = \frac{m}{2e}v_i^2 \tag{I-8}$$

For the case $v_0 = 0$, (I-8) can be expressed as:

$$V_i = \frac{2\cos^2(\alpha)\, V_{RF}}{N\pi\cos(\alpha) + 2\ \sin(\alpha)} \tag{I-9}$$

The minimum voltage V_i that will lead to a multipactor discharge happens when the denominator of (I-9) is maximum. This means that the electrons phase is equal to:

$$\alpha = \operatorname{atan}\left(\frac{2}{N\pi}\right) \tag{I-10}$$

I.4.1.b Multipactor order

As previously mentioned, the multipactor order N refers to the number of half periods that took for the electron to reach from one surface to another. Figure I.6 shows a representation for the electrons trajectory for multipactor orders 1, 3, and 5.

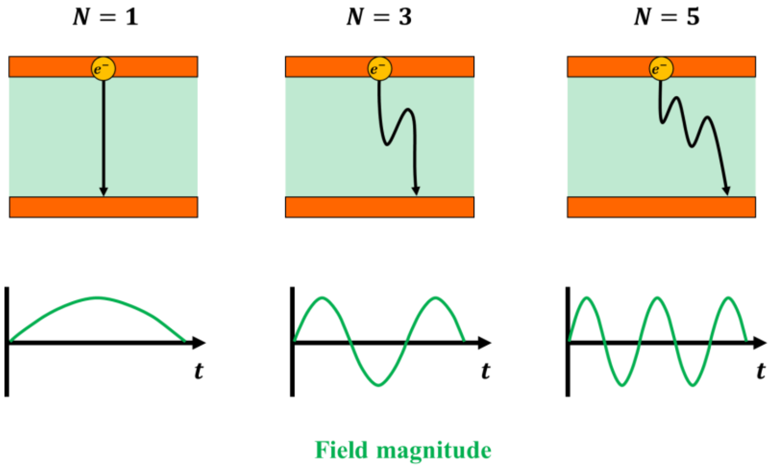

Figure I.6 Electron trajectory for different multipactor order between parallel plates.

With equations presented in I.4.1.a, we can study the regions where a multipactor break can occur in terms of the product between the frequency and the gap between the plates ($f \times d$) for different multipactor orders as presented in Figure I.7. The different regions presented for each multipactor order N show the voltages that will lead to a break at their corresponding $f \times d$. As multipactor order increases, the different regions can overlap, meaning that at a given $f \times d$, a multipactor break can occur in N or N+2, as it can be seen for the regions corresponding to N=7 and N=9 Figure I.7.

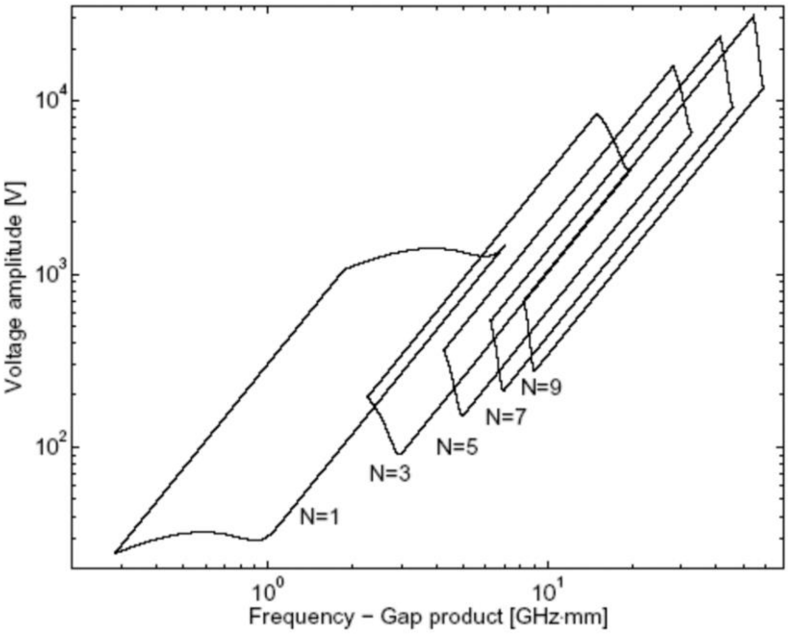

Figure I.7 Multipactor susceptibility chart [10].

I.4.1.c Secondary Emission Yield

The secondary Emission Yield (SEY) is a characteristic property for every material and refers to the number of secondary electrons that will be released, on average, by an incident (primary) electron at a determined level of energy.

$$\delta = \frac{average\ number\ of\ secondaty\ electrons}{1\ incident\ electron} \tag{I-11}$$

Figure I.8 shows a representation of the SEY of a generic material, showing three important points: First crossover $(E_1, 1)$, maximum point (E_{max}, δ_{max}) and the second crossover $(E_2, 1)$, which corresponds to the region where the multipactor can occur. For examples an incident electron arriving with an energy $E_i < E_1$ will not produce an avalanche since the SEY at this point is lower than unity, meaning that on average, less than 1 new electron will be released.

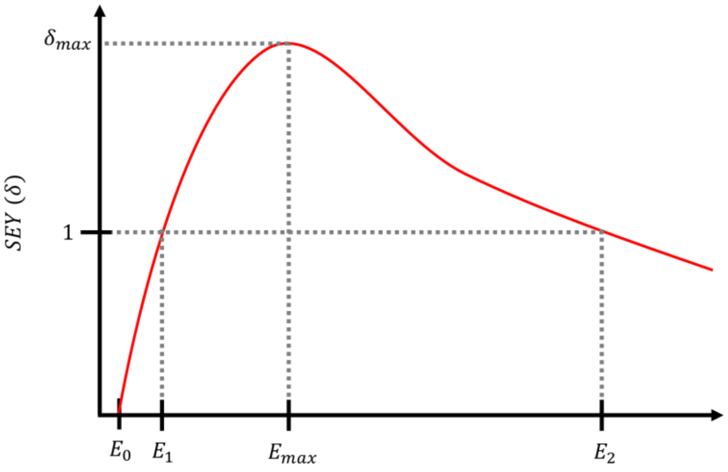

Figure I.8 General SEY characteristic curve.

Vaughan model

The modeling of the SEY curves is based on models that best fit the SEY measurements of different samples. One of the most popular models used today is the one presented by Vaughan in 1989 [8]. This model divides the SEY in two regions, a low and a high energy region and considers the incident angle of the primary electron respect to the surface normal since a correction must be done for different impact angles (θ). The $\delta_{max}(\theta)$ and $E_{max}(\theta)$ will then be defined by (I-12) and (I-13) respectively.

$$\delta_{max}(\theta) = \delta_{max}\left(1 + \frac{k_E \theta^2}{2\pi}\right) \tag{I-12}$$

$$E_{max}(\theta) = E_{max}\left(1 + \frac{k_\theta \theta^2}{2\pi}\right) \tag{I-13}$$

The parameters k_E and k_θ are related to the surface roughness and are generally considered as 1, although values for different materials can be found on the literature. Once this correction being done, we can calculate the δ curve.

First, for all incident electrons with an impact energy (E_i) below E_0 it is assumed that all the incident electrons are backscattered. Then, for impact energies over E_0, two different regions are defined, low energy and high energy regions respectively. The criterion for dividing these regions is done using the parameter v as presented by equation (I-14). If $v \leq 3.6$ it is a low energy region and if $v > 3.6$ it corresponds to the high energy region.

$$v = \frac{Ei - E_0}{E_{max}(\theta) - E_0} \qquad \text{(I-14)}$$

For the low energy region ($v \leq 3.6$) we have:

$$\delta = \delta_{max}(\theta)\left(v - e^{1-k}\right)^k \qquad \text{(I-15)}$$

Although the original Vaughan model proposes $E_0 = 12.5\ eV$ on an arbitrary way, a modified version of this model proposes E_0 to be a new fitting parameter in order to have a better fit of the first crossover energy E_1 between the experimental data and the model [11] , [12]. There is a special interest in fitting correctly the first crossover since it is a parameter that affect considerably the multipactor breakdown, this will also define the value of the parameter k as presented:

$$k = \begin{cases} 0.56 & for\ v < 1 \\ 0.25 & for\ 1 < v \leq 3.6 \end{cases} \qquad \text{(I-16)}$$

For the high energy region ($v > 3.6$) we have

$$\delta = \delta_{max}(\theta)\frac{1.125}{v^{0.35}} \qquad \text{(I-17)}$$

Figure I.9 shows the SEY modeling of three different materials, at an incident angle normal to the surface and $E_0 = 12.5\ eV$.

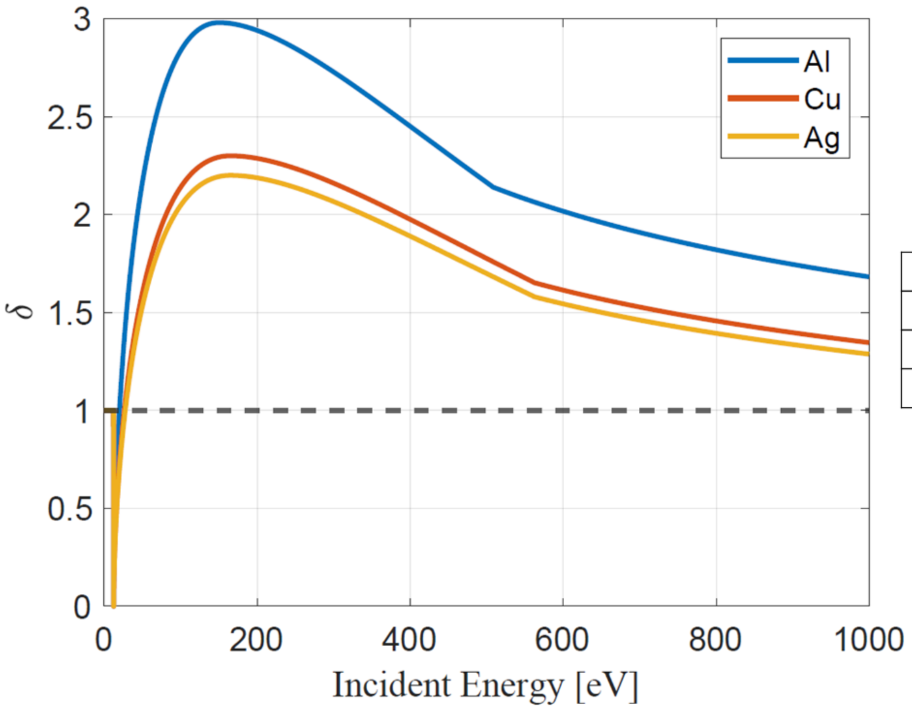

	δ_{max}	E_{max}
Al	2.98	150
Cu	2.3	165
Ag	2.2	165

Figure I.9 Compared SEY for different materials.

Additionally, Figure I.10 shows the SEY curve for silver at different incident angles respect to the normal of the surface. As the angle increases, the emission of secondary electrons will increase for the same incident energy E_i.

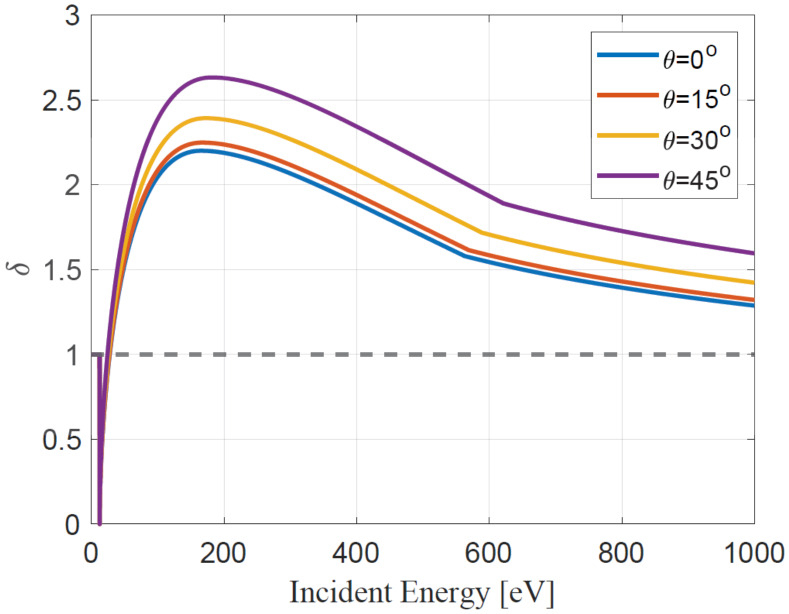

Figure I.10 SEY of silver at different incident angles.

Furman-Pivi model

The Furman-Pivi model presents a more sophisticated SEY representation, when compared to Vaughn’s, providing energy and angular distributions for the emitted electrons. This model separates the secondary emissions into three different components. When a current of electrons arrives to a surface a portion of them will be backscattered, giving the first component (δ_e) of the model. From the portion that penetrates the material we can find electrons that are reflected as a result of their interaction with one or more atoms inside the material, also known as rediffused electrons (δ_r). Finally, the true secondary electrons (δ_{ts}) result of a more complex interaction of the incident electron current. A representation of each of these three components is presented in Figure I.11 and equation (I-18) shows the link between them to obtain δ [13].

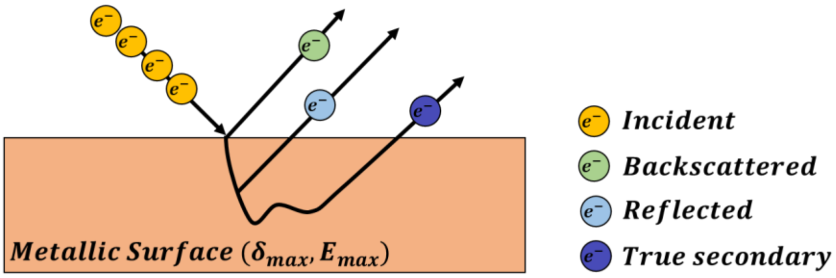

Figure I.11 Representation of the three components of the SEY on Furman's model

$$\delta = \delta_e + \delta_r + \delta_{ts} \tag{I-18}$$

In this model, a correction of the incident angle is also done for each of the different components of the SEY by a multiplicative factor of the form $1 + a_1(1 - \cos^{a_2}(\theta))$, where a_1 and a_2 are parameters that must be calculated separately for each of the three components. Finally, Figure I.12 presents the fit of this model to experimental data of a copper sample at normal incident angle, showing a good agreement between the data and the model. All three components are plotted separately, and it can be observed that the highest contribution to the SEY corresponds to true secondary electrons.

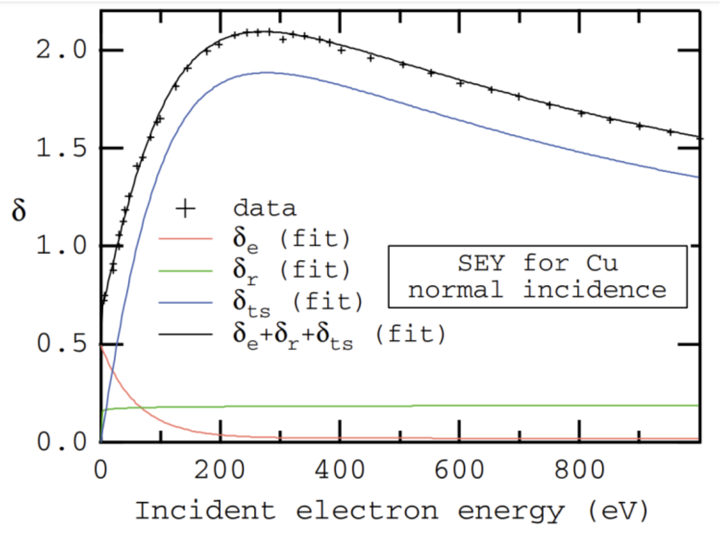

Figure I.12 SEY comparison between the Furman-Pivi model and experimental data for a copper sample.

A comparison between Vaughan's and Furman's models is presented in Figure I.13 showing curves for copper for normal and an incidence angle of 60°. Differences between both models can be observed at the low and high energy regions. However, the most important difference is on the low-energy region since the Furman-Pivi model makes a more accurate estimation of the SEY [14].

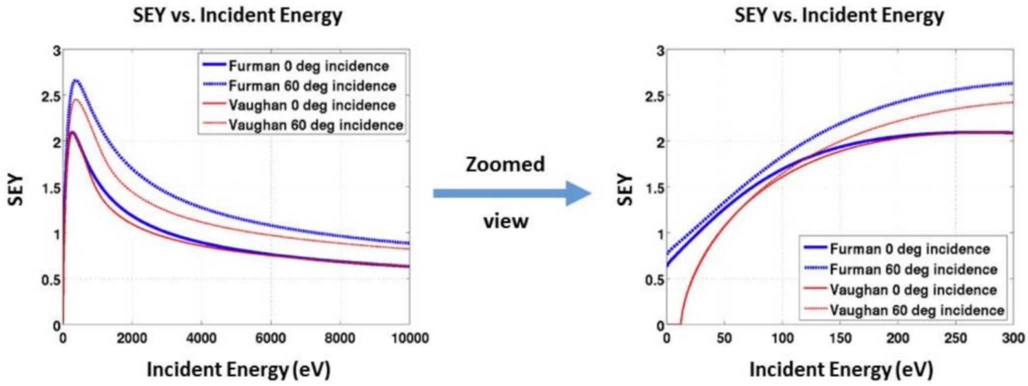

Figure I.13 SEY vs Incident energy curves for Vaughan and Furman-Pivi models at normal and 60°inicdence angles for copper taken from [14].

I.4.2 Modeling and Simulation

Multipactor discharges have been modeled and studied using different tools and Models like Analytical calculations, Monte Carlo and Particle-In-Cell simulations, statistical theory, and on the recent years with map-based and chaos theories.

I.4.2.a Analytical models

As multipactor is a voltage driven effect, the peak voltage in the critical section of the component can be used to determine the power at which multipactor will occur. First thing to do is to determine the voltage of the gap to be studied when the device has an input power of 1W (V_{1W}). Then, the voltage required for the discharge must be calculated. In the case of simple structures, it can be obtained using (I-5). Finally, an estimation of the multipactor power can be predicted as follows:

$$P = 1W\left(\frac{V_{RF}}{V_{1W}}\right)^2 \qquad \text{(I-19)}$$

The main inconvenience with this method is the reduction of accuracy of the final value, and the need of an electromagnetic simulator to obtain the voltage at 1W input power of the device [15].

A more complex calculation of the multipactor power can also be done using the time average stored energy (TASE) in the structure. In this case, the energy stores in the structure at 1W input power is needed. The calculation is done using (I-20).

$$P = 1W\left(\frac{V_{RF}}{V_{1W}}\right)^2\left(\frac{1J}{TASE_{1w}}\right) \tag{I-20}$$

I.4.2.b Particle simulations

To simulate complex structures like RF filters or antennas, particle simulators are a good solution. For a multipactor simulation, the electromagnetic fields of the structure are needed, as an excitation signal and the materials´ SEY of the surfaces. Simulations are done by placing electrons inside the structure (this electron distribution can be defined or aleatory), that will interact with the imported electromagnetic fields. The simulator will calculate the acceleration, trajectories, and interaction of an electron when it collides with a surface. Based on the material SEY, it will evaluate how many secondary electrons will be released for every collision.

As a result, the simulator will obtain the electron population evolution over time inside the structure. This information is thereafter used to infer the presence of a multipactor break. Figure I.14 shows a representation for the total number of electrons over time for two different powers. For power P_1, the total number of electrons decreases over time, therefore no multipaction is present. Alternatively, the number of electrons increases for the power P_2, consequently it can be concluded that a multipactor discharge occurred.

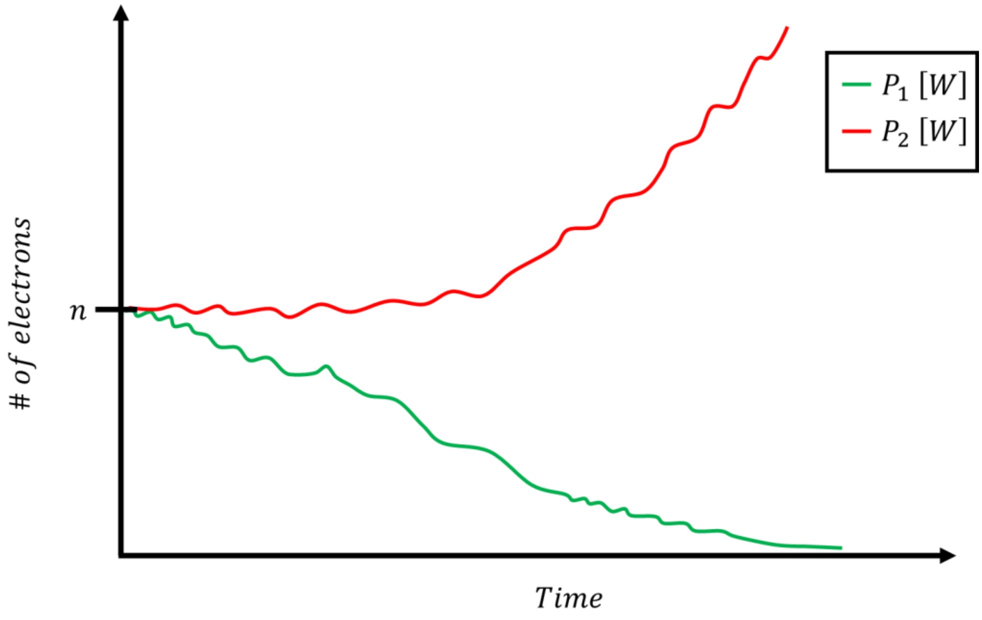

Figure I.14 Particle simulator results representation

The use of simulators allows to characterize of high complexity structures. Nevertheless, this increases calculation times drastically as a consequence of the need of accurate fields simulation, linked to the electron's trajectories, electron seeding, and secondary electrons emission at every collision [15].

In this work, two multipactor simulators were used, SPARK 3D and CST Particle Studio, although other simulation tools can be found, such as ANSYS HFSS for example. Table I.2 shows the main differences between these simulators. In a global view, Spark 3D is simpler to use and has lower simulation time than CST-PS. But CST allows a deeper management of simulation parameters and allows us to have multiple materials at the same time. For the latest version of SPARK3D, multiple materials can be used, but this is bounded to a previous electromagnetic simulation using CST or ANSYS HFSS and is still bounded to the mesh quality of this simulation.

Table I.2 Features comparison for SPARK 3D and CST-PS

Feature	**SPARK 3D**	**CST-PS**
Fields computation	Imported from external software	Computed by CST-MW
Simulation region	User bounded	Whole structure
SEY curves	Imported and Vaughan modified model	Imported, Vaughan and Furman-Pivi models
Material definition	Only one material (for version before 2022)	Multiple materials
Macroparticles	Automatic	User specified number of electrons per macroparticle.

I.5 Multipactor mitigation techniques

To limit multipactor breakdown, different techniques can be used. These techniques can be divided into 2 different classifications: active and passive, which will modify either RF fields of materials' properties.

I.5.1 Fields modification

Modification of the electric or magnetic fields in the structure is a highly studied and used technique for multipactor mitigation [16] [17]. For example, in [18] external magnets are used to modify the magnitude of the magnetic field of a coaxial line. As multipactor threshold is influenced by the magnitude of the RF field, the use of external permanent magnets is proved to be effective to mitigate or attenuate a breakdown. When measuring multipactor discharge, a break was not detected when magnets where used.

Although the use of permanent magnets for multipactor suppression showed to be a good approach, these magnets surrounding all the component will require additional bulk and could interfere with other RF elements of the system.

I.5.2 SEY modification

Parallel to the electromagnetic field modification, another approach to mitigate the apparition of multipactor is the change of material properties particularly the SEY. This can be done by surface treatments or by surface coatings and both approached present advantages and disadvantages, for example for some surface treatments, the SEY reduction effect can be lost after the surface is exposed to air [19].

I.5.3 Surface treatments

The use of artificially roughened or porous surfaces with lower SEY for multipactor mitigation is also studied. In this case, the modification of the material’s SEY is achieved by increasing the roughness of the metallic surface. The extra roughness will serve as traps for the primary electrons that arrive or depart from the surface decreasing the probability of a secondary electron release. Figure I.15 shows a conceptual design on how the treatments change the roughness of the surfaces.

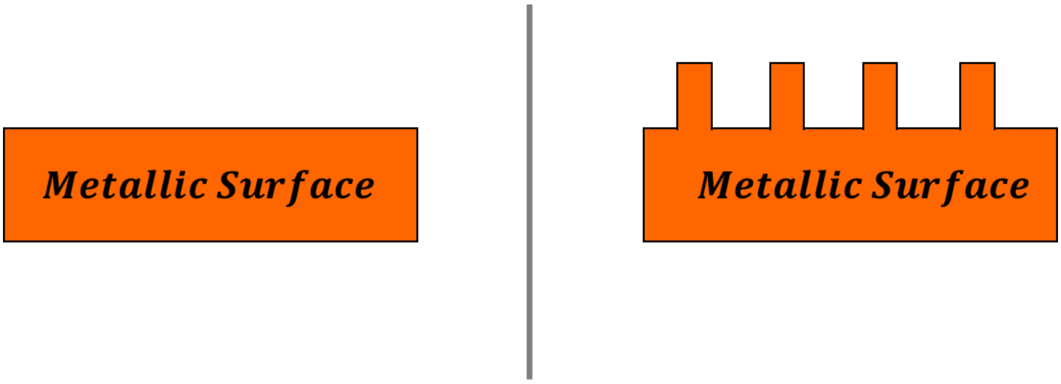

Figure I.15 Completely flat surface (left) surface with increased roughness (right)

The work in [20] presents the utilization of silver nanopillars like the ones presented in Figure I.16 for the reduction of SEY. Fabricated by glancing angle deposition with DC magnetron sputtering, the length of the nanopillars is controlled by the deposition time.

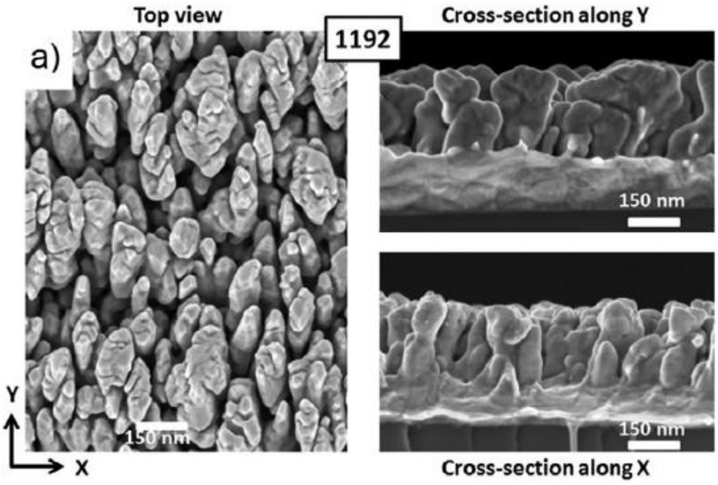

Figure I.16 Fabricated nanopillars in [20]. Top view (left) and cross sections (right)

These elements' added roughness reduces the SEY by trapping the free electrons and impeding an avalanche. In this work, the SEY was measured and compared with a flat non-treated surface, showing a reduction on the secondary electron's emission particularly at lower energy levels as it can be seen in Figure I.17 for different times of sputtering for generating the nanopilars.

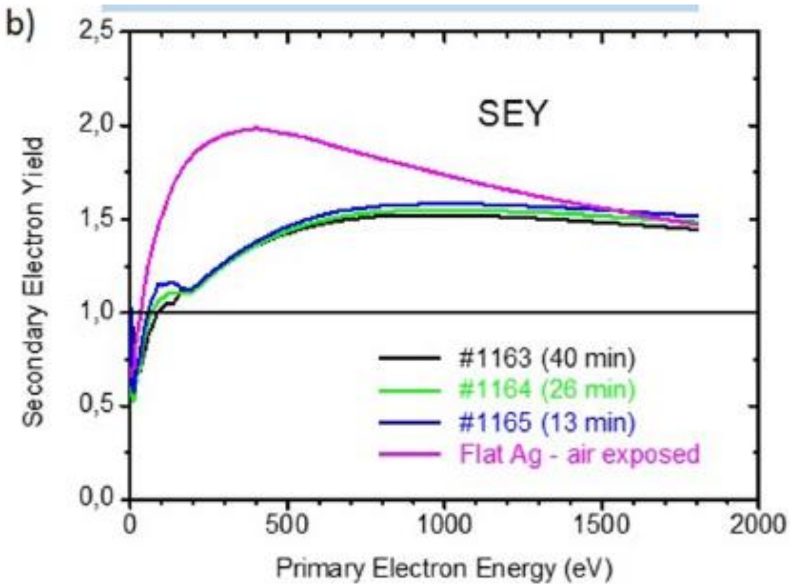

Figure I.17 SEY measurements for different samples [20]

Although, increased roughness leads to a higher surface resistance due to the skin effect, which results in higher losses, the surface resistance of the fabricated samples was estimated and was found that these surface treatments can be compatible with requirements in the space industry [20].

I.5.4 Surface Coatings

As an alternative to a surface modification, surface coatings are also used to modify the surfaces SEY. When a primary electron reaches a coated surface, the SEY of the coating material will interact in the discharge event. The use of materials with lower SEY, compared to raw metallic surfaces, is desired for realizing coatings as for example, dielectric composites [21], TiO2 [22] carbon based coatings [21].

For example, [21] presents the impact of dielectric concentration in composite materials used for coatings. Even at a 5% dielectric presence, the SEY reduction is significant when compared to an all-metallic surface. For higher dielectric concentrations, the electrons absorption is increased and the SEY of this coating is always lower than 1 as it can be seen in Figure I.18. meaning that no secondary electrons will be released therefore no multipactor break will occur. Nonetheless, the use of this type of dielectric bases composites increases the losses of the structure and lowering the overall quality factor of the structure.

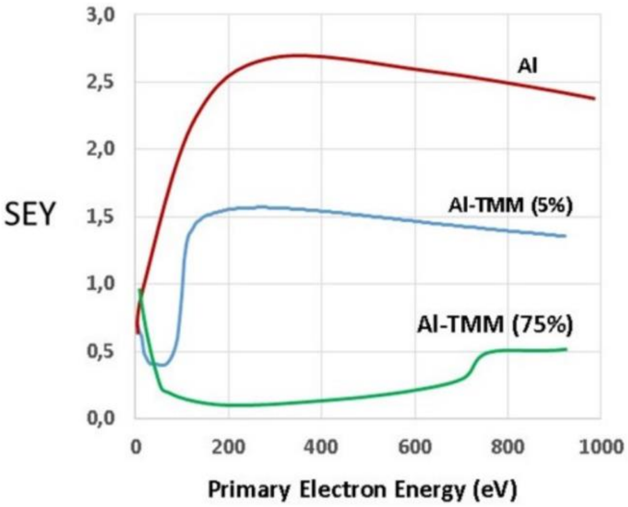

Figure I.18 SEY measurements for metal-dielectric composites coatings [21]

In the same work, graphite coatings are also studied. A comparison between graphite, and nanostructured graphite (obtained by the splitting of natural graphite) is presented in Figure I.19 and shows the positive impact of carbon coatings in the reduction of SEY. However, the exposition to air of the graphite has a negative impact on the SEY performance of the coating since it contaminates the surfaces and generally oxidates the samples. Additionally, graphite coatings are much complicated to implement and have a higher cost.

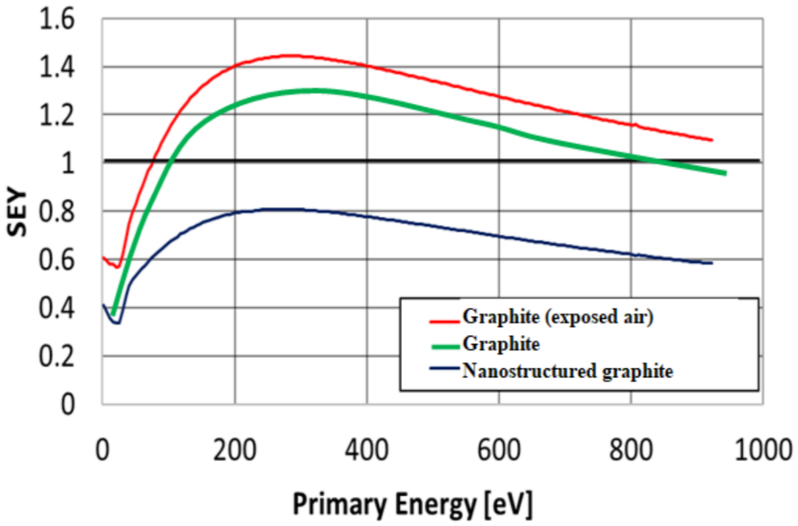

Figure I.19 SEY measurement of two different graphite coatings [21]

I.6 Chapter I conclusion

As higher constraints are applied in the design of microwave components for space applications, the multipactor effect is more relevant and novel solutions to impeach its apparition must be proposed. Within the actual proposals for multipactor protection, the surface treatments, and coatings are solutions that modify the materials SEY without interfering with the RF fields or adding additional parts to the components.

However, air exposure of some of these solutions degrades the SEY response and reduces the efficiency of the treatment, as in the case of titanium nitrides. In addition, although these methods seem to be able to produce surfaces with very low secondary electron yields (lower than 1) they are difficult to apply on a large scale as in a complete microwave structure as filters or antennas.

Chapter II : Carbon coatings

II.1 Introduction

In this chapter, the study of the selected carbon coating is presented. In the first section, a brief introduction on how the selected coating is done is given. Then the coating characterization is described in 3 main axes. First, the potential impact of this coating in terms of electrical conductivity and the consequences this could have in the performance of a filter. Second, the fabricated samples are presented followed by their SEY characterization. Finally, the design, fabrication and measurement of an electrical conductivity characterization structure is presented with the measurements and results.

II.2 Selected Carbon coating

Based on the equipment available at Nanyang Technological University at Singapore (NTU), an amorphous carbon coating is done using High-Power Impulse Magnetron Sputtering (HiPIMS) technology, a plasma-based technology extensively used to deposit thin films. Sputtering creates smooth coatings with reduced friction and sticking. The high-power density on the cathode generates ionized atoms, for hard, high-density coatings with good wear resistance (like carbon).

In HiPIMS, high voltage, short duration burst of energy are focused on a coating material to generate a high-density plasma that results in a high degree of ionization of the coating material in the plasma. Pulsing the target coating material with bursts of high voltage energy allows for a large fraction of the sputtered target material to be ionized in the plasma cloud without overheating the target and other components of the system.

The main advantage of HiPIMS over conventional sputtering is the control of a pulsed powerful high voltage that ionizes an extremely high percentage of the target material without overheating, creating a dense plasma cloud with virtually no droplets. This produces high performance dense coatings with good adhesion that are extremely smooth. Figure II.1 shows a diagram for the setup of this technology [23].

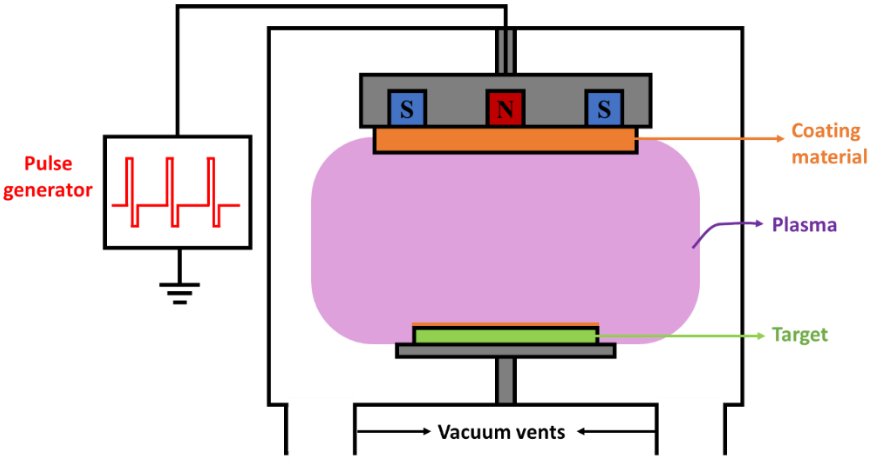

Figure II.1 HiPIMS setup diagram

II.3 Coatings' characterization

As the carbon coatings are going to be used in microwave components, it is important to determine the impact of these coatings on the electrical response of the structures. As it has already been mentioned in Chapter 1 (Section I.5.4), surface treatments and coating can have a significant impact on the electric conductivity of the treated surfaces.

In the framework of this work, components in the transmission stage (Tx) of a satellite are of our interest. Hence, a Tx filter will be designed and tested with and without carbon coating.

II.3.1 Conductivity sensibility analysis

The determination of the critical areas of a two-section coaxial Stepped Impedance Resonator (SIR) [24] , [25] was done. This was done to determine the critical areas of the resonator, and the impact of these coatings on the resonator's quality factor. For doing this, a two-section coaxial SIR was selected and designed with a 1.5 GHz central frequency. Then, 5 different coating areas were defined and numbered from 1 to 5.

Figure II.2 shows the 5 different defined areas. Area number 1 is presented with a green color and corresponds to the inner walls for the outter section. Area number 2, represented with a dark-blue color, corresponds to the outter wall of the medium conductor. The third area, is the inner wall of the medium conductor. Area number 4 corresponds to the central conductor of all the structure and finally, the fith area corresponds to the top and bottom covers.

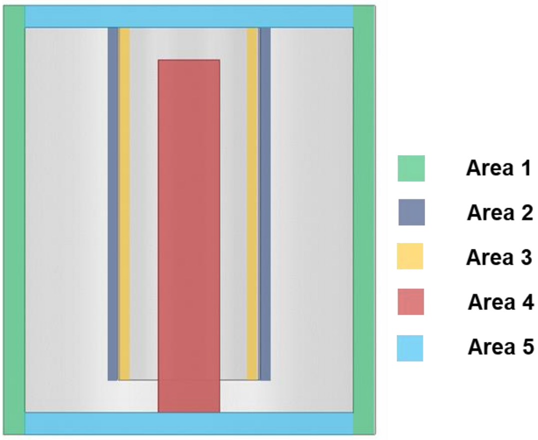

Figure II.2 Two-section coaxial stepped impedance resonator coating areas definition

After the definition of the areas to be studied, limit values for the conductivity of the experiment were selected. First, a worst-case scenario of a conductivity degradation up to 1 MS/m was picked as the lower level of the variable. Then, a best-case scenario of 62 MS/m conductivity, for the carbon coating was used.

A total of 32 cases were simulated referring to the different possible combinations of conductivity values. Some examples are presented in Table II.1

Table II.1 Examples for combinations of conductivity values

Case	Area 1	Area 2	Area 3	Area 4	Area 5
1	**1 MS/m**	62 MS/m	62 MS/m	62 MS/m	62 MS/m
2	62 MS/m	**1 MS/m**	62 MS/m	62 MS/m	62 MS/m
3	62 MS/m	62 MS/m	**1 MS/m**	62 MS/m	62 MS/m
4	62 MS/m	62 MS/m	62 MS/m	**1 MS/m**	62 MS/m
5	62 MS/m	62 MS/m	62 MS/m	62 MS/m	**1 MS/m**

In order to evaluate the impact on the Quality factor of the resonator, a script on Matlab that controlled the setup of every simulation and made an analysis of the results was implemented. This script changes the conductivity of every area and generates a Phyton code that will start the ANSYS HFSS simulation with the desired configurations (Eigenmode). When simulation is done, results are saved in a test file and are imported again by Matlab for their prior analysis. The implemented sequence allows an effective and reliable simulation. Figure II.3 presents the workflow of the implemented code. This allows simulation of more complex scenarios in a simplest and faster way, with no need of launching every simulation by hand, which opens the door to possible human mistakes.

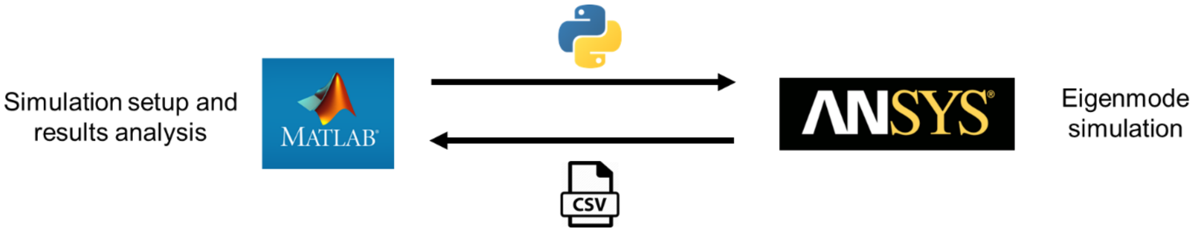

Figure II.3 Simulation workflow

A first analysis of the results obtained for the cases presented on Table II.1 showed that all the sections have a different impact on the structure quality factor as presented in Table II.2. It was observed that for case number 2, the decrease of the quality factor was greater than for the others. However, these results only correspond to 5 of all the simulations, and no critical areas can be defined with this information.

Table II.2 Quality factor results for previously described cases in Table II.1

Case	Q-factor
1	770
2	479
3	1196
4	665
5	1280

To compare all the simulations, the results for these simulations are presented from Figure II.4 to Figure II.8 in a Q-factor V.s frequency plot. For each figure dedicated to one area, the data colored in red represents the values where the dedicated area has a conductivity value of 1 MS/m. As explained in [26], the quality factor can be expressed in terms of the complex resonant frequency for eigenmode analysis of electromagnetic cavities. In the presented results, the frequency value is the real part of the complex frequency, resulting in different frequency values for different quality factors. However, these variations are under 0.23% for a 1.5 GHz resonant frequency.

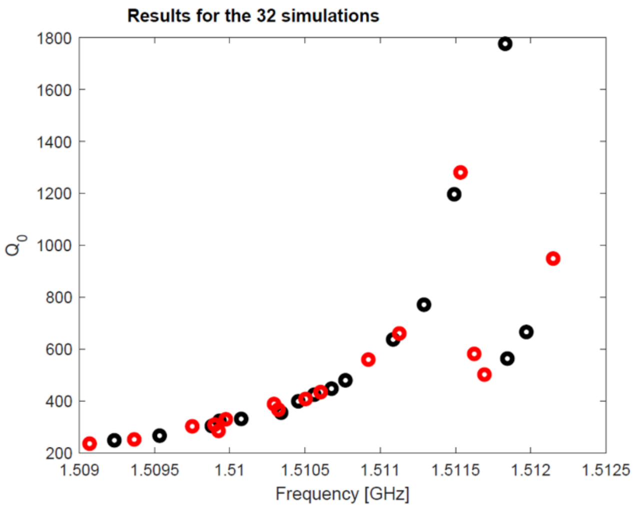

Figure II.4 Results Area 1

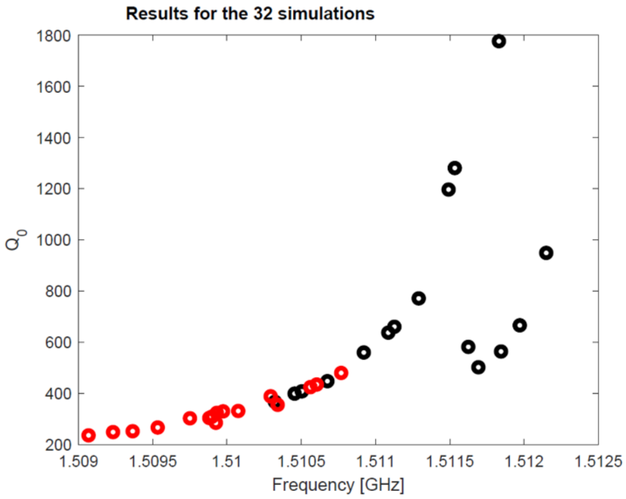

Figure II.5 Results Area 2

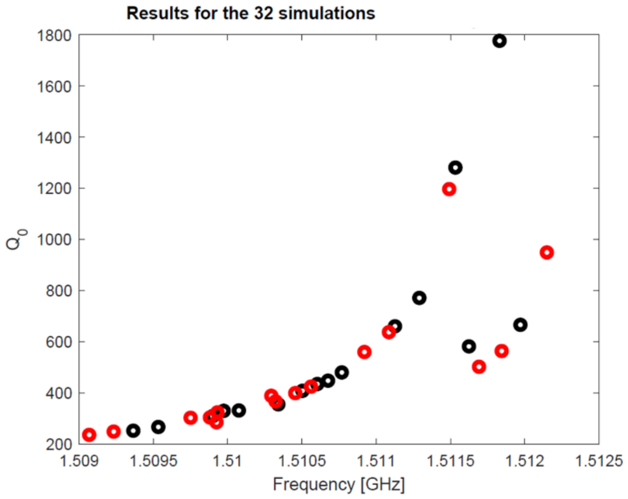

Figure II.6 Results Area 3

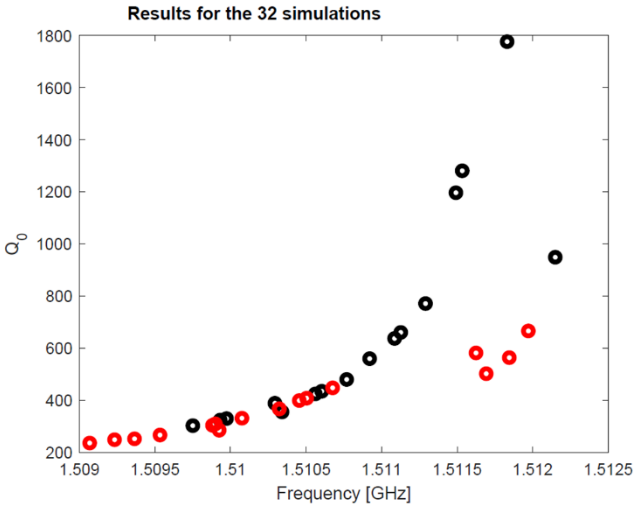

Figure II.7 Results Area 4

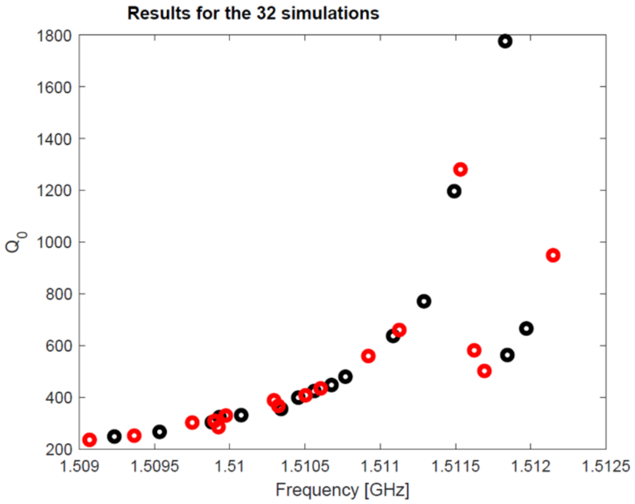

Figure II.8 Results Area 5

When observing the results of each area, it was identified that area number 2 (Figure II.5) was the one with lower quality factors (under 500) when it had a conductivity of 1 MS/m. While other areas had configurations with quality factors above 600. This means that the most critical area of the resonator is area number 2, a low conductivity here will have a greater impact on the overall quality factor. In this order of ideas, the areas are classified as follows from more critical to less critical: 2-4-1-3-5.

With these results, if a partial coating of the structure is done, a selection of preferred coating areas can be done. For example, if a multipactor break occurs between areas 1 and 2, it is preferable, in terms of quality factor maximization, to coat area number 1.

II.3.2 Fabricated carbon samples

After the impact sensibility analysis was completed, a characterization of carbon coating was done. For this, squared samples of 5 cm x 5 cm were defined based on the biggest possible dimensions for carbon coating at NTU. Using silver samples provided by GoodFellow, the carbon coatings were done aiming for the maximum possible thickness (around 20 nanometers). Figure II.9 shows a picture of the resultant samples after being coated. During the whole time, both samples were stored separately in different containers and identified as “Sample 1” and “Sample 2”.

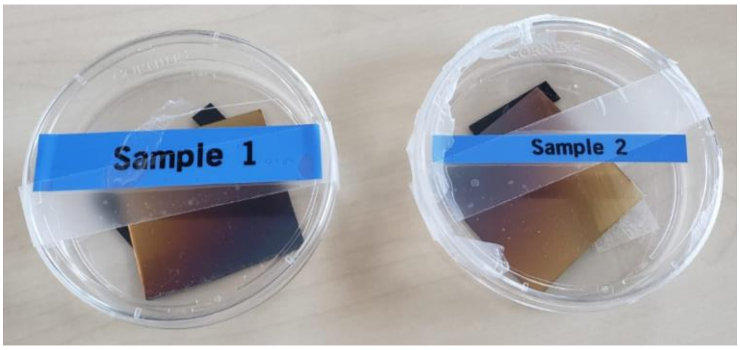

Figure II.9 picture of the received samples of carbon coated silver

On a first visual inspection, it was observed that coloring of the samples was not uniform through the surface. Nevertheless, a complete carbon coating was assured by NTU and later verified with the measurement performed in this chapter.

II.3.3 TEEY Characterization

The Total Electron Emission Yield (TEEY) characterization of the samples was done by Onera Laboratory in Toulouse. To do so, samples are placed under an electron gun that will send a current of electrons with different energies to the sample, then the reflected electrons energy will be measured around the sample. A picture of the measurement setup is presented in Figure II.10. Two samples of silver and two other samples of carbon coated silver were measured. In order to have good information about the TEEY of the samples, two types of measurements were done.

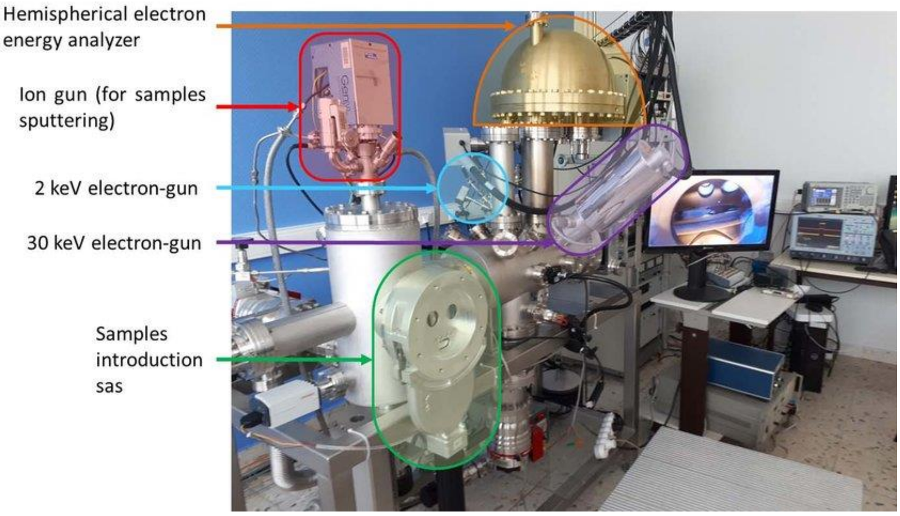

Figure II.10 SEY measurement setup at ONERA

The first SEY measurement was carried out at 0° incident angle. Figure II.11 presents the results for these measurements comparing the measurement of the two samples, under the name of “New samples 2021”, with a precedent measurement of a carbon coating done in 2018 (HPIMS 2018). Also, the TEEY curve of one of the silver samples is presented as “Reference native Ag” in order to compare the results of the carbon coatings.

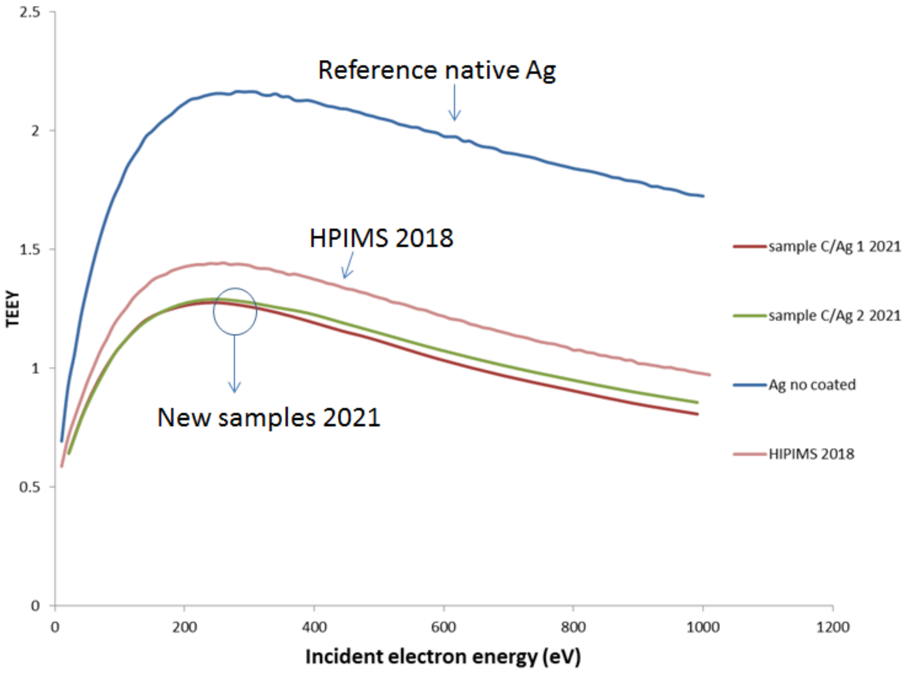

Figure II.11 SEY measurements comparisons at 0° incident angle

When observing results of the measurements, we can observe that the carbon coating presents a lower TEEY than the silver, either for the 2018 sample or the latest ones. Also, the first crossover energy for the carbon coated samples is higher, meaning that a higher incident energy will be needed to start an avalanche. Additionally, the good agreement between both carbon coated samples, especially at lower energies, suggests that the selected coating method will give trustable and repeatable results for further implementations.

Then, the samples are heated up to 100°C and the second type of TEEY measurement is done. In this second run, measurements are also done for different incident angles from 0 to 60° in steps of 20°. Results of these measurements are presented in Figure II.12

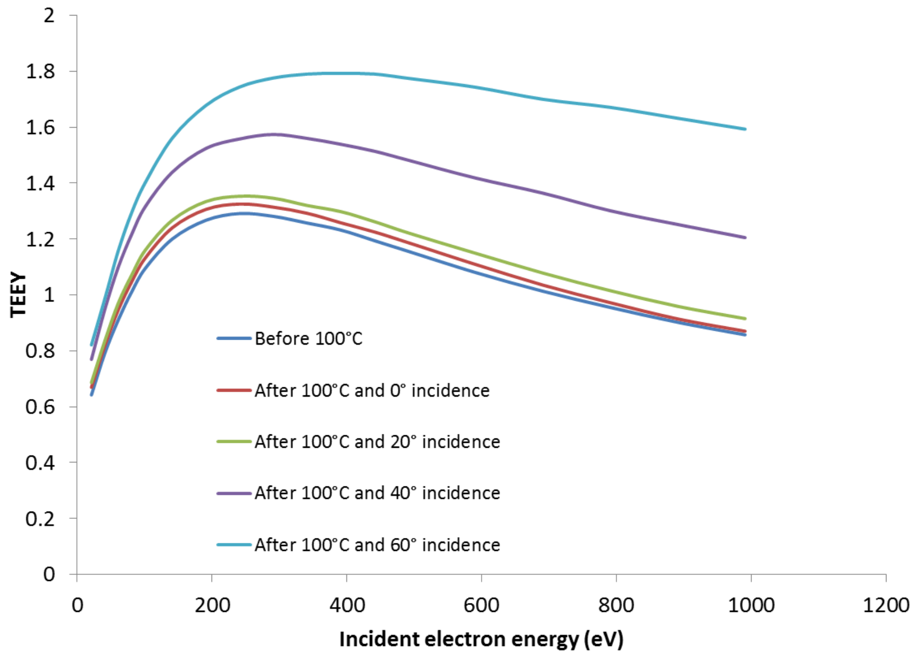

Figure II.12 SEY measurements after samples heating

On these measurements it can be seen that the δ_{max} of the carbon coated samples is lower than one of the reference silver samples, even after the samples had been heated and with an incidence angle of 60° from the normal. These results show that the use of the selected carbon coating is a good way to reduce the SEY of the silver samples with coatings of only 20 nm.

II.3.4 Conductivity Characterization

A cylindrical resonator was chosen as the characterization structure. A high Quality-factor, in the order of tens of thousands (10 000), can be obtained, which leads to a high sensitivity of the measurement. The cavity is designed to operate in the TE_{011} mode as this mode has a high-quality factor. As presented on Figure II.13, the first step is to measure the homogeneous quality factor Q of the cavity, since it is all the same metal, and estimate the conductivity of the cavity metallization σ_{ref}. Then, one extremity (cover) of the cavity is replaced by the sample under test and therefore the conductivity of the sample σ_{sample} can be extracted from the measurement of the mixed Quality factor Q_{mix}.

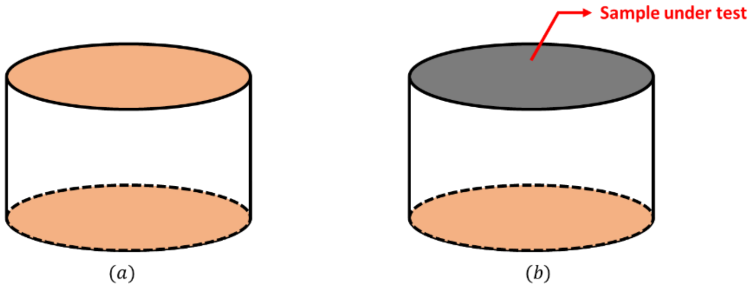

Figure II.13 (a) Homogeneous cavity configuration for reference conductivity σ_{ref} measurement. (b) Cavity configuration for sample conductivity σ_{sample} measurement

II.3.4.a Structure Design

For the design of the characterization structure, the main restriction was the size of the samples to be measured, as the available samples were of 5 cm x 5 cm this was the maximum diameter that could be used for the cavity. The dimensions of the samples is an important factor for setting the working frequency of the cavity. With a security distance of 2 mm on every side of the sample to place the sample and assure a full placement, a cylindrical cavity with 46 mm diameter was designed.

In [27], it is shown the ratio $\mathrm{Diameter/Height}$ has an impact on the error of the estimation on the losses of the cavity due to the walls of the cavity. The bigger the height of the cavity, higher the losses due to the cylindrical wall's material and the measurement of the sample decreases its accuracy. Therefore, a ratio $\mathrm{Diameter/Height} = 3.5$ was selected as it leads to an error in the estimation of the sample conductivity in 10% with lower losses in the cylindrical cavity walls. This leads to a cavity that will be operating at 13.819 GHz, for a cavity at 1.5 GHz a bigger sample would be needed.

Equations (II-1) to (II-5) show the homogeneous quality factor Q of the TE_{011} mode and σ_{ref} in terms of the cavity dimensions and the measured quality factor Q.

$$Q = \frac{\pi f_0 \mu_0 H_c R_c}{\frac{2Rs}{k^2}\left(k_g^2 R_c + \frac{H_c}{2} k_c^2\right)} \tag{II-1}$$

$$R_s = \frac{1}{\sigma\sqrt{\frac{2}{\mu_0\mu_r\omega\sigma}}} \tag{II-2}$$

$$R_s = \frac{\pi f_0 \mu_0 H_c R_c}{\frac{2Q}{k^2}\left(k_g^2 R_c + \frac{H_c}{2} k_c^2\right)} \tag{II-3}$$

$$\frac{1}{\sigma\sqrt{\frac{2}{\mu_0\mu_r\omega\sigma}}} = \frac{\pi f_0 \mu_0 H_c R_c}{\frac{2Q}{k^2}\left(k_g^2 R_c + \frac{H_c}{2} k_c^2\right)} \tag{II-4}$$

With a relative permeability of the material $\mu_r = 1$, the conductivity σ_{ref} is:

$$\sigma_{ref} = Q^2 \frac{\left(\frac{k_g^2}{k^2} 2R_c + \frac{k_c^2}{k^2} H_c\right)^2}{\pi f_0 \mu_0 H_c^2 R_c^2} \tag{II-5}$$

Following the estimation of the cavity material conductivity, the same must be done to find the expression of the sample conductivity (σ_{sample}) in terms of the cavity dimensions, the cavity conductivity σ_{ref} and the new measured Quality factor (Q_{mix}) as it is presented in detail in [1] and shown in equations (II-6) and (II-7).

$$Q_{mix} = \frac{\pi f_0 \mu_0 H_c R_c}{Rs_{sample}\frac{k_g^2}{k^2} R_c + R_s\left(\frac{k_g^2}{k^2} R_c + \frac{k_c^2}{k^2} H_c\right)} \tag{II-6}$$

$$\sigma_{sample} = \frac{1}{\left(\frac{H_c\sqrt{\pi f_0 \mu_0}}{Q_{mix}\left(\frac{k_g^2}{k^2}\right)} - \left(1 + \frac{k_c^2}{k_g^2}\frac{H_c}{R_c}\right)\frac{1}{\sqrt{\sigma_{ref}}}\right)^2} \tag{II-7}$$

When operating at the TE_{011} mode, the TM_{111} mode is also present at the same frequency. This is observed when comparing the formulas for the resonance frequency of the TE_{mnl} (II-8) and for the TM_{mnl} (II-9) [28], where P_{nm} and P'_{nm} are de m^{th} roots of $J_n(x)$ and $J'_n(x)$. Here, $P'_{01} = P_{11} = 3.8317$.

$$f_{mnl} = \frac{c}{2\pi\sqrt{\mu\varepsilon}}\sqrt{\left(\frac{P'_{nm}}{R_c}\right)^2 + \left(\frac{l\pi}{H_C}\right)^2} \tag{II-8}$$

$$f_{mnl} = \frac{c}{2\pi\sqrt{\mu\varepsilon}}\sqrt{\left(\frac{P_{nm}}{R_c}\right)^2 + \left(\frac{l\pi}{H_c}\right)^2} \tag{II-9}$$

Therefore, a strategy for separating both modes must be implemented. In [27] a solution is proposed using a “trap” like structure. As a multiple frequency characterization is desired, an adjustable moving cover is conceived. This diving cover will keep the TE_{011} mode in the lower part of the cavity (resonant zone) and will prevent the establishment of the TM_{111}. The air gap between the diver and the wall of the cavity stops the current flow impeaching the TM_{111} to be established. Consequently, all the energy at the defined frequency will be stoked in the TE_{011} mode. Figure II.14 presents a front view comparison of a normal cavity and a cavity with the proposed diver.

Both solutions were simulated in ANSYS HFSS and their performances were compared. Although both solutions have a good mode suppression effect, the diver solution has more freedom degrees that leads to a more optimal and versatile design of the cavity and allows the cavity to be tuned to a specific frequency. Therefore, a diver solution was implemented.

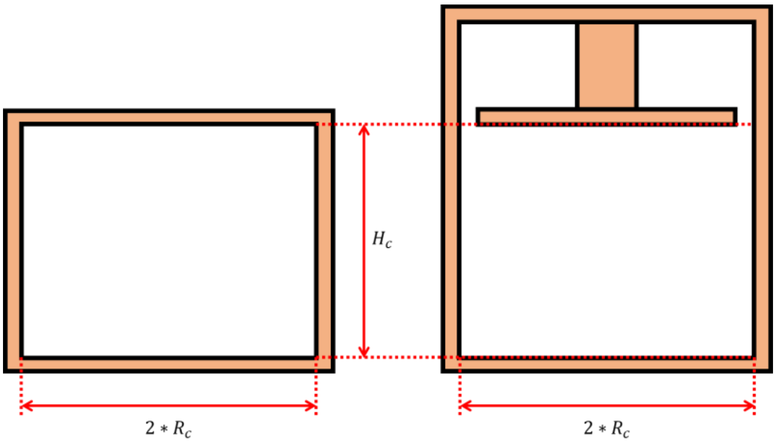

Figure II.14. Concept design of the characterization structure without and with diver

A full wave electromagnetic simulation is performed using ANSYS HFSS. The excitation of the cavity is made through a waveguide access at both sides of the resonator. The bottom part of the structure has a cover that can be replaced by a sample of maximum 5 cm x 5 cm and 2 mm thickness. The diver structure is at the top of the structure. Figure II.15 shows the top and front views of the simulated structure. From the top view, the sample placement area can be observed. Also, the electric field distribution at the resonant frequency is plotted, which corresponds to the electric field distribution of the TE_{011} mode.

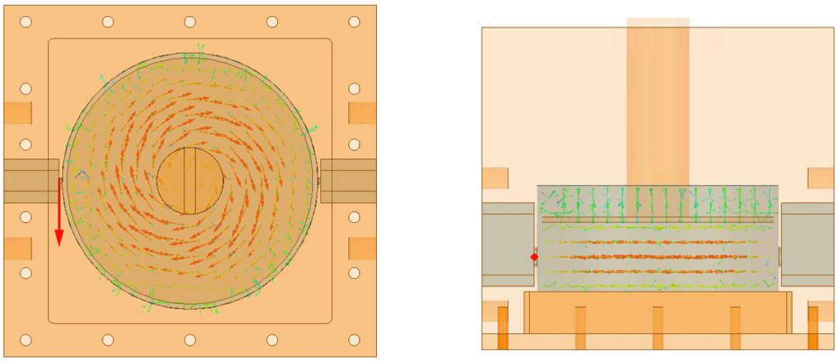

Figure II.15. ANSYS HFSS model of the characterizations structure. Top (left) and front view (right)

II.3.4.b Fabricated structure

All the pieces of the structure were fabricated in copper By Breizh Usinage [29] using copper Cu-a1 (CU-ETP) and Cuc1. Pictures of the fabricated structure are presented from Figure II.16 to Figure II.18

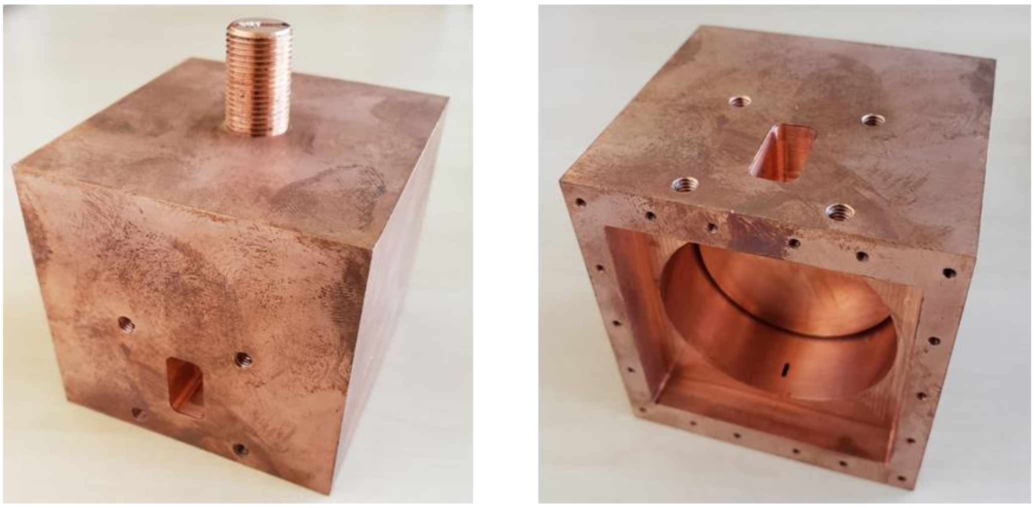

Figure II.16 Fabricated conductivity characterization structure

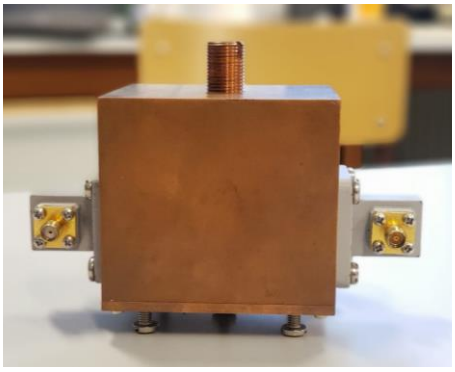

Figure II.17 Structure with TGC connectors for measurement

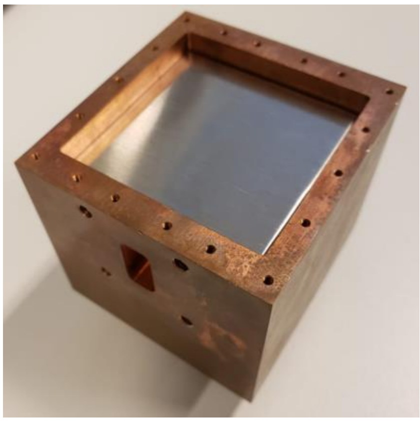

Figure II.18 Fabricated structure with aluminum sample.

Figure II.19 shows a silver sample and a carbon coated silver sample. These samples were placed over the copper cover, which is also used as mechanical support. As the carbon coated samples do not have a uniform color, the hypothesis that the coating thickness is not uniform was proposed. In order to determine if this could have an impact on the electrical conductivity of the sample, a measurement procedure was defined rotating the samples by 90° for each measurement. Figure II.20 and Figure II.21 present the measurement setup of each type of sample.

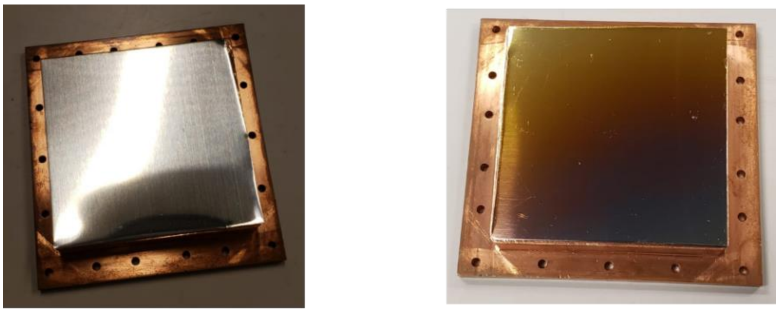

Silver

Carbon coated silver

Figure II.19 Measured samples on the support cover. Silver (left) and carbon coated silver (rigth)

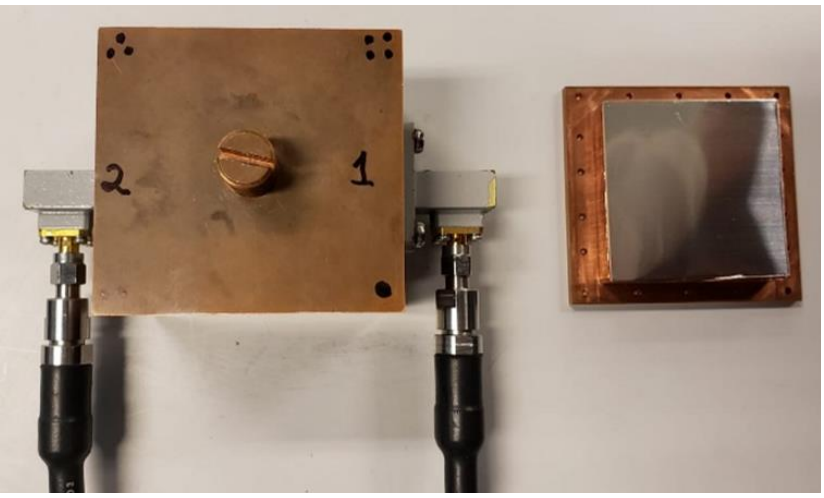

Figure II.20 Measurement setup for silver samples

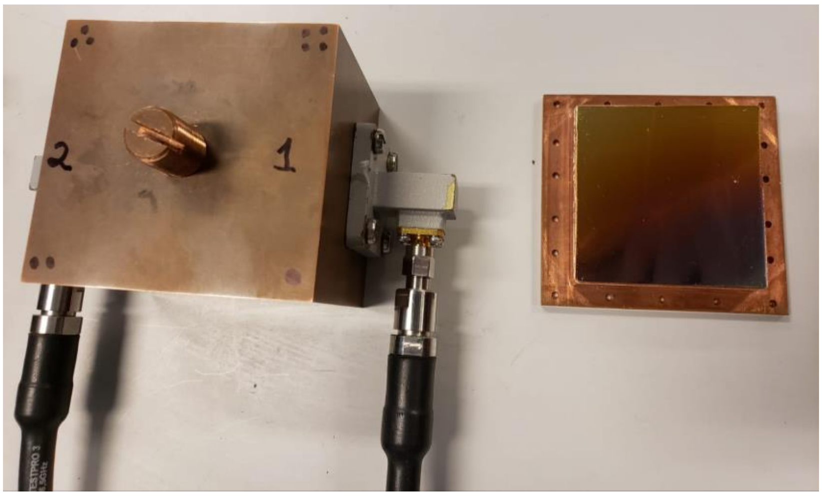

Figure II.21. Measurement setup for silver coated samples

II.3.4.c Measurements

First, a Broadband (13 GHz – 15 GHz) measurement of the characterization structure was done. A comparison between measurements and simulations showed a general good agreement between the simulated and the measured response, as presented in Figure II.22. Nevertheless, an unexpected resonance appeared around 13.6 GHz. After different measurements of the structure performed to find the source of this resonance, it was found that it corresponds to a resonant mode that established in the upper section of the structure above the diver [3]. To validate this finding, a measurement without the bottom cover was performed (Figure II.23).

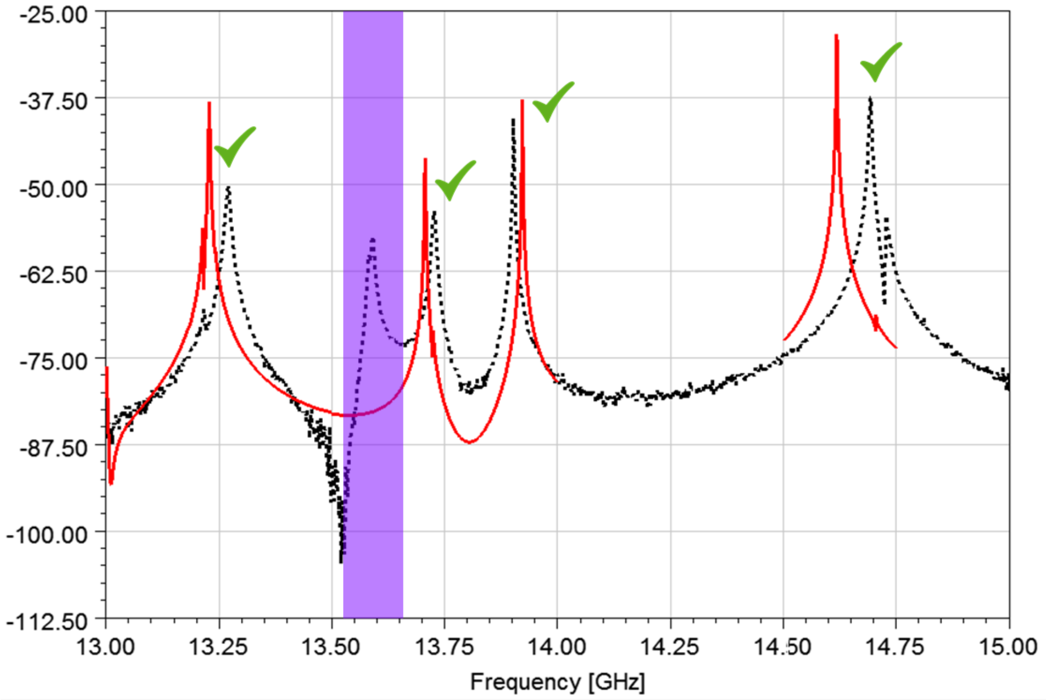

Figure II.22 Simulated (continuous red line) v.s measured (dashed black line) results

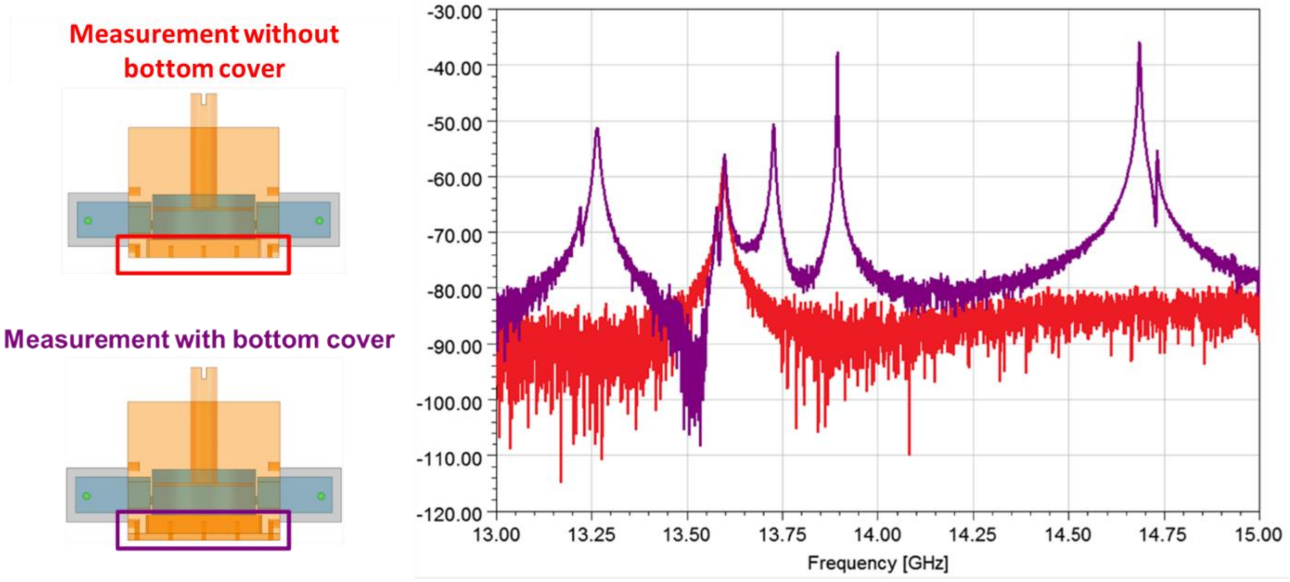

Figure II.23 Validation measurements comparison for parasite mode

As it can be observed in Figure II.24, a resonance at 13.9 GHz is present. This corresponds to the resonance of the TE_{011} mode. It is observed that no additional resonances, that could interfere with the desired resonant mode, are present from 13.75 GHz up to 14.7 GHz.

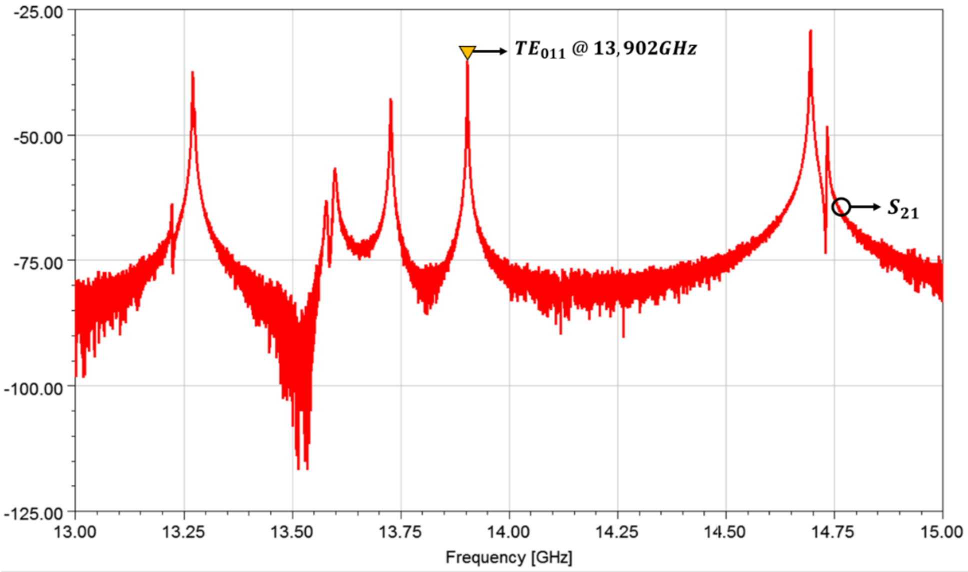

Figure II.24 Broadband measurement of the characterization structure

Figure II.25 presents the frequency response of the cavity for different narrow-band measurements with the copper cover. Based on these results, the copper conductivity estimation was done, and results are presented in Table II.3. Seven different measurements were done with slight variations of the diver height to evaluate the impact of the diver position. Due the high-Quality factor of the structure, the resonance is highly sensitive to the position of the diver and the resonance frequency is slightly shifted as observed in Figure II.25. However, all the conductivity estimations were done using the nominal height as the maximum variation of the diver position was of only 0.5 mm.

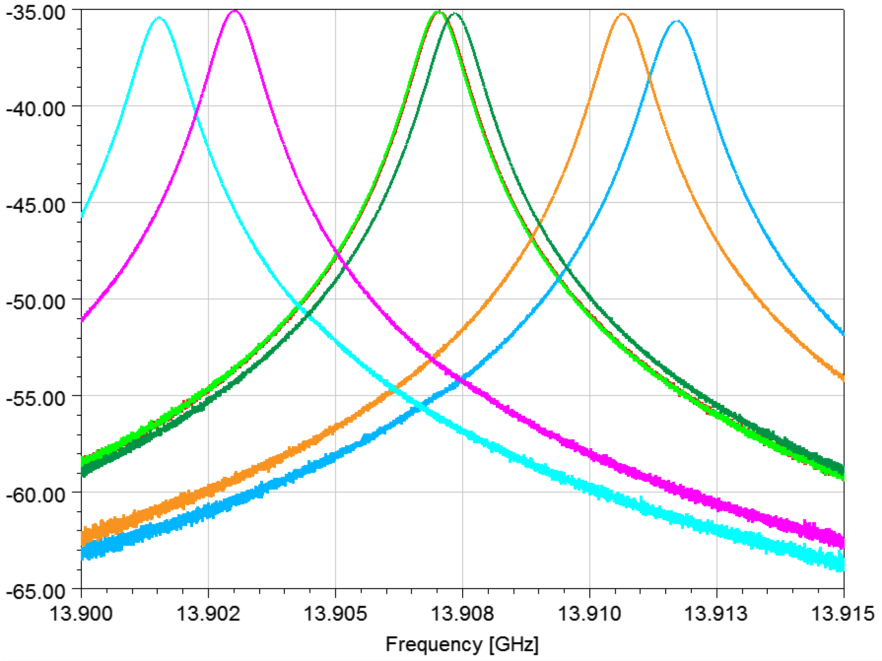

Figure II.25. Different measurements for copper cover

Table II.3. Conductivity estimation results for the copper cover

Case	$Q-factor$	BW_{-3dB} $[MHz]$	σ_{DC} $[MS/m]$	$\sigma_{14\ GHz}$ $[MS/m]$	Variation
Copper_Meas_1	14 540	0.973	58	51.13	11.85%
Copper_ Meas_2	14 437	0.973	58	51.18	11.76%
Copper_ Meas_3	13 434	1.050	58	43.82	24.45%
Copper_ Meas_4	14 518	0.975	58	50.97	12.12%
Copper_ Meas_5	14 371	0.984	58	50.04	13.72%
Copper_ Meas_6	14 449	0.979	58	50.48	12.97%
Copper_ Meas_7	14 628	0.967	58	51.23	11.67%

After the estimation of the copper conductivity, which corresponds to the reference value σ_{ref}, measurement of samples of silver and silver coated with carbon were done. A picture of the characterization structure with a silver sample is presented in Figure II.20. Two silver samples and two silver with carbon coating samples where available.

For each sample, a total of 12 measurements were performed. Each sample was marked with a reference trace in the bottom and placed in 4 different orientations. For each orientation, the reference marker would correspond to one of the corners of the cavity, also identified with different position markers as presented in Figure II.26. At the end, each sample was placed in the 4 positions and 3 measurements were made for each position (orientation).

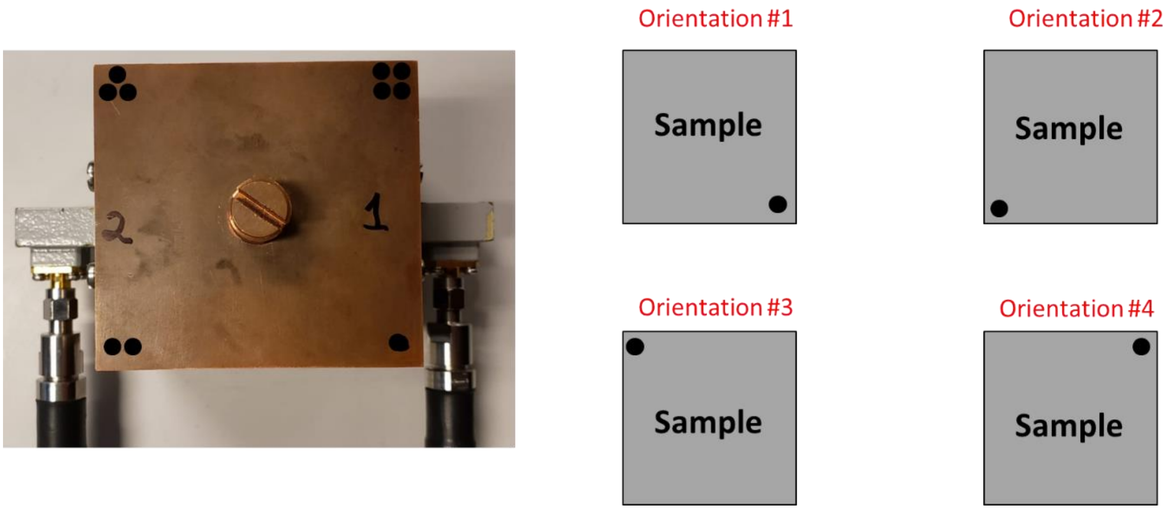

Figure II.26 Orientation definition for sample measurement

A complete table of all the measurements is presented in Table 0.1 of the annex section. Table II.4 presents the average values for measured quality factor and estimated conductivity for the four samples under test. Results of the estimated conductivity at 13.9 GHz are presented as the average of the 12 measurements per sample ± the standard deviation of the same 12 measurements.

For all the measurements, it was observed that the measurements had a low variation (5.3 % maximum), and for the carbon coated samples, the results where more consistent between them. In term of conductivity impact, the carbon coating did not significantly decrease the conductivity of the sample. If we compare silver sample 1 and carbon coating sample 2, we can even see that the coated samples has a higher conductivity, this can be explained because some of the samples were not completely flat and some bending was present in the samples, leading to a non-uniform sample and not having a completely closed structure with additional losses.

On the other hand, when comparing silver samples 2 and the carbon coated sample 2, a difference of 4 MS/m between conductivity values can be taken as low as this represents a degradation of 7.7%.

Table II.4 Silver and carbon characterization results summary

Sample	$\boldsymbol{Q-factor}$	$\boldsymbol{\sigma_{DC}\ [MS/m]}$	$\boldsymbol{\sigma_{estimated}\ [MS/m]}$ **@13.91 GHz**
Reference Copper	14 630	58.00	51.67 $\pm$ 2.30%
Silver_1	14 233	61.00	45.68 $\pm$ 5.30%
Silver_2	14 681	61.00	52.59 $\pm$ 4.75%
Carbon_coating_1	14 383	-	47.98 $\pm$ 3.15%
Carbon_coating_2	14 428	-	48.54 $\pm$ 3.52%

II.4 Chapter II conclusion

From the results presented in this chapter, it can be said that the amorphous carbon coatings can be considered as a multipactor mitigation technique as they have a SEY and electrical performances that will allow a good incorporation in microwave structures allowing higher power handlings.

As presented in the first section of the chapter, the effective electrical conductivity of the silver samples with carbon coatings is a critical factor when designing a filter. A lower conductivity values could have redhibitory effects on the quality factor of the structure and on the filter response, based on the area to be treated. Fortunately, the designed characterization structures allowed the measurements of the electrical conductivity of the samples with a high precision and repeatability, with a maximum dispersion of 5.3 %.

The measurements showed that the impact of these coating does not represent a significant decrease of the samples’ conductivity. This, since the thickness of the coatings is of 20 nm, on its thickest area, a value that is relatively thin when compared with the skin depth at 14 GHz (536 nm). So, the superficial losses would not be modified.

On the other hand, the 20 nm thickness was enough to modify the silver SEY and reduce the number of secondary electrons of the coated samples, since this electrons’ interaction occurs on the first 5 to 10 nm of the surface. In addition, the amorphous carbon coating presented not only a lower δ_{max}, but a higher first crossover energy, meaning that more energy will be needed to start an electrons avalanche, increasing the power handling of a RF structure.

Finally, the coatings presented good mechanical handling based the low damage while being handled for the electrical conductivity measurements, although additional test should be done to validate that they can be space qualified.

Chapter III : Structure design for multipactor test

III.1 Introduction

In this chapter, the specification, design, modeling, and fabrication of a multipactor test structure is presented. The objective of this structure is to allow power measurements that will validate carbon coatings as a solution for multipactor protection in RF equipment. To do so, an integration of the characterization results presented in section II.3.4.c were considered in the simulations.

Different studies were done to design a robust structure that would allow reliable power measurements. First, the electrical specifications and the selected topology are presented in sections III.1 and III.2. Then, the impact of the different design variables of the structure was determined by different studies in section III.3. Third, structure specifications and the final design of the structure, are presented and explained in sections III.4 and III.5.

Then, section III.6 shows the multipactor analysis of different structures and the impact of integrating carbon coatings on the overall power handling of these structures. Finally, sections III.7 and III.8 will present the final designed structure and measurements respectively.

III.2 Multipactor simulations

The multipactor simulations performed in this section allowed the determination of critical areas of the structure. These simulations were performed using SPARK 3D for most of the cases and CST particle solver for specific cases.

III.2.1 SPARK 3D setup

The software SPARK 3D uses the electric and magnetic fields of the structure, or area, to be studied. These fields must be previously obtained by and electromagnetic simulation, in our case these simulations were used using ANSYS HFSS. Once the fields are imported from

ANSYS HFSS they cannot be modified, so the quality of the SPARK 3D simulation results will depend directly on the electromagnetic simulation. The available version of SPARK3D only allowed the use of a single material. Later versions of this simulation tool allow the use of different materials at the same time.

The multipactor simulation parameters were set up in order to do an ascending search of the power break starting at 0.1 W, with a maximum power of 1000 W and, a resolution of 0.1 W. Additionally, the initial electrons distribution could be modified choosing from a homogeneous electrons distribution or a no homogeneous. In the no homogeneous distribution, the software places the electrons in the areas with higher electric field. On the other hand, in the homogeneous distribution, electrons are placed all over the structure in such a way that they are equally distributed all over the simulation volume.

Results between these two distributions should not vary a lot between them. Figure III.1 shows the result of a simulated structure using both electron distributions, and Figure III.2 shows the electron distribution with both configurations at the beginning and after 70 ns, resulting in the identification of the same multipactor threshold and area of avalanche.

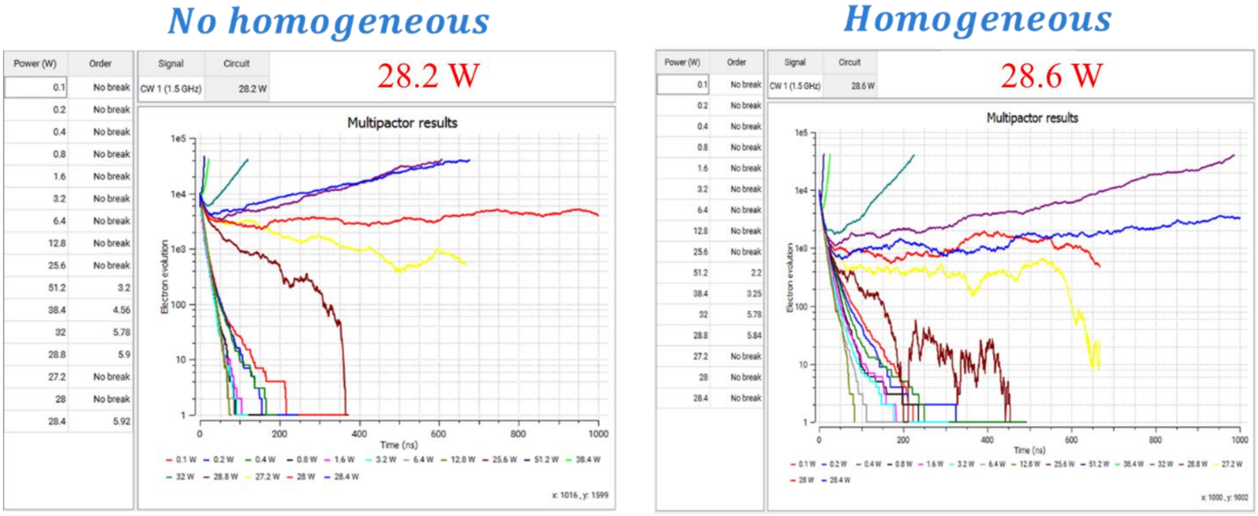

No homogeneous

Power (W)	Order
0.1	No break
0.2	No break
0.4	No break
0.8	No break
1.6	No break
3.2	No break
6.4	No break
12.8	No break
25.6	No break
51.2	3.2
38.4	4.56
32	5.78
28.8	5.9
27.2	No break
28	No break
28.4	5.92

Signal	Circuit
CW 1 (1.5 GHz)	28.2 W

Homogeneous

Power (W)	Order
0.1	No break
0.2	No break
0.4	No break
0.8	No break
1.6	No break
3.2	No break
6.4	No break
12.8	No break
25.6	No break
51.2	2.2
38.4	3.25
32	5.78
28.8	5.84
27.2	No break
28	No break
28.4	No break

Signal	Circuit
CW 1 (1.5 GHz)	28.6 W

Figure III.1 Multipactor simulation with no homogeneous and homogeneous distributions

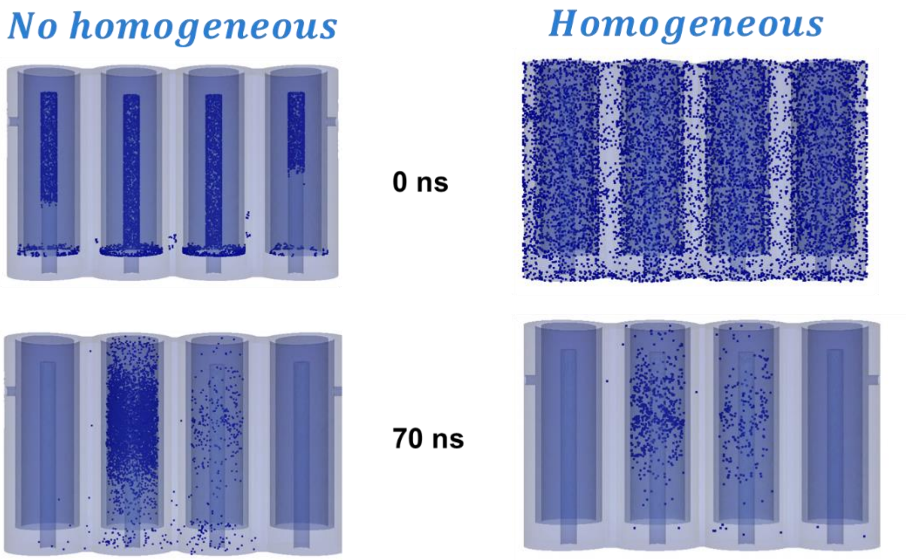

Figure III.2 Electrons position with no homogeneous and homogeneous distributions

III.2.2 CST setup

As mentioned previously CST is a more powerful simulation tool compared to SPARK3D. To use the CST Particle Solver tool for multipactor simulations, an electromagnetic simulation in CST frequency solver is needed. The structure can be modeled directly on CST or a STEP file can be imported from another simulation tool like ANSYS HFSS, this final option was the one used for this work.

Once the electromagnetic simulation is done, the electric and magnetic fields of the structure must be saved at the frequency to be studied, contrary to a SPARK3D simulation where fields are exported at the meshing frequency. Now, the problem type is changed to “Particle” and Particle In Cell (PIC) is selected. Once this is done, the fields can be imported and a Maxwellian particles source model is created, in this configuration multiple parameters as macroparticles, boundary settings and more can be modified. In here, materials secondary emission characteristics can be modified individually for every material allowing to choose between a Vaughan, Furman, or a user’s imported model.

III.3 Study of a coaxial transmission line

In this section, a preliminary study to determine the impact of carbon coatings in simple RF structures was done. Different transmission coaxial lines with different characteristic impedances, a length of 10 mm and a distance between conductors of 0.65 mm were simulated.

For each line, 4 multipactor simulations were done using CST-PIC, the first simulation assumed an all-silver line. The second simulation assumed the inner conductor was coated with carbon. In the third one, the coating is placed in the external conductor, and finally the fourth simulation assumes a carbon coating of both conductors.

The results are presented in Figure III.3 and the coated area is represented in red for each case. It is observed that the used of carbon coating increases the power handling of these structures in all configurations. It is also seen that for higher characteristic impedances, the maximum power gets reduced. For the partial coatings, the maximum power handling does not increase significantly compared to the complete coatings of the transmission lines.

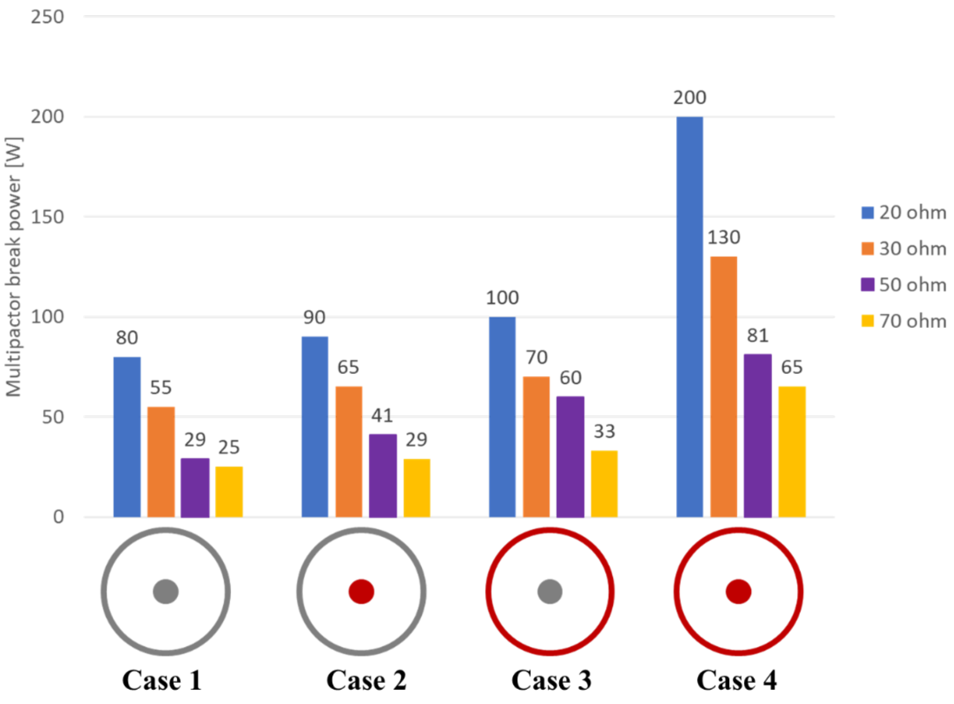

Figure III.3 Power handling results for coaxial transmission lines at different impedances and for a distance between conductors of 0.65 mm

III.4 Resonant structure specifications

First, it was important to define the electrical and physical characteristic of the test structure, so that a robust and trusted prototype could be fabricated and measured correctly. The main constraint was the measurement setup for the multipactor breaks test. Since the available setup at Thales Alenia Space, Toulouse, works at a central frequency of 1.5 GHz, and has a maximum detection power of 400 W, power breaks above this value cannot be measured. Also, it was important to consider the size and geometry of the structures to be coated, since they should fit the HiPIMS carbon coating setup at NTU, Singapore.

III.5 Structure design

III.5.1 Two-section Coaxial Stepped Impedance Resonator

Coaxial Stepped Impedance Resonators (SIR) are formed from multiple coaxial structures fitted inside one another in a head-to-tail arrangement, where the ground conductor of the internal structure becomes the central core of the next one. These structures are arranged alternately presenting an open circuit at one end and a short circuit at the other, forming a quarter-wave resonator. This type of resonators can be formed by n sections each with its characteristic impedance Z_i and the same physical length l.

The simplest case of a coaxial SIR is the two-section case, made up of two coaxial sections with characteristic impedances Z_1 and Z_2, with their respective electrical lengths θ_1 and θ_2. The ideal electrical representation model of this case is presented in Figure III.4. Each section is represented with its characteristic impedance Z_i and electrical length θ_i.

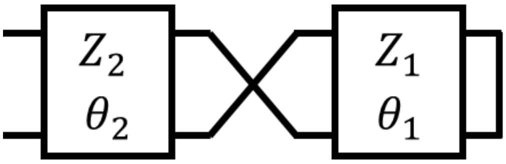

Figure III.4 Two-sections coaxial Stepped Impedance Resonator model

An example of the physical implementation of the two-sections coaxial SIR, is presented in Figure III.5. Here, three main conductors form the resonator, a first open-end coaxial structure is formed between the red and the blue conductors, and a short-end outer section is formed between the blue and gray conductors. In this case, there is air between the metallic conductors so $\varepsilon_r = 1$ and the electrical lengths θ_1 and θ_2 are the same ($\theta_1 = \theta_2$).

On a first design approach, the width of the second conductor (blue) is neglected for simplicity.

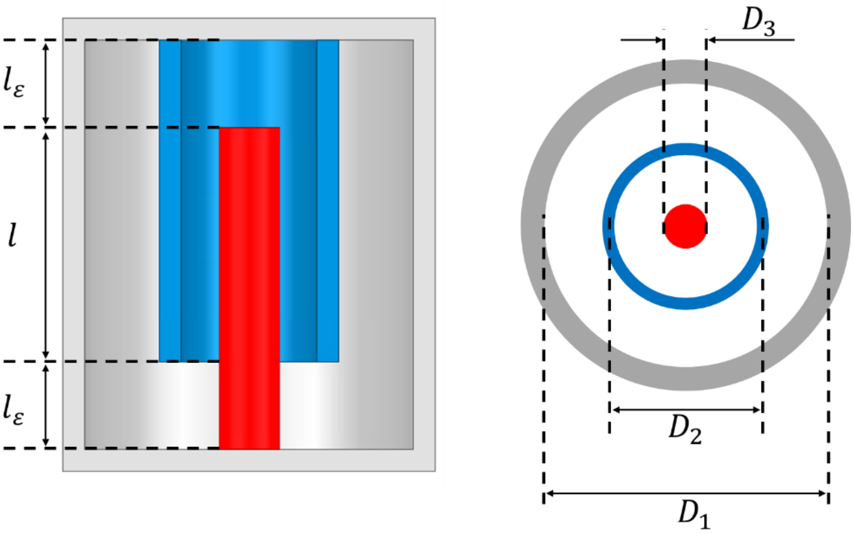

Figure III.5 Two-section Stepped Impedance Resonator geometry

Figure III.5 also presents the design variables of the two-section coaxial SIR resonator:

l_ε → coupling length between sections.

l → length of the coaxial section of the resonator

D_1 → diameter of the outer conductor (C_1) of the outer coaxial section

D_2 → diameter of the shared conductor (C_2) between the inner and outer coaxial sections

D_3 → diameter of the central (C_3) conductor of the inner coaxial section

In addition, two additional variables are presented for the study of the structure. These variables, noted A_1 and A_2, are the distances between conductors and are defined as follows:

$$A_1 = D_1 - D_2 \tag{III-1}$$

$$A_2 = D_2 - D_3 \tag{III-2}$$

Using these variables, the characteristic impedance of the coaxial sections and the electrical length can be obtained by using (III-3) and (III-4).

$$Z_i = \frac{\eta_o}{2\pi\sqrt{\varepsilon_{ri}}} \ln\left(\frac{D_i}{D_{i+1}}\right) \tag{III-3}$$

$$\theta_i = \beta_i l \tag{III-4}$$

where the phase constant is

$$\beta_i = \frac{2\pi\sqrt{\varepsilon_{ri}}}{\lambda_0} \tag{III-5}$$

Being η_0 the free space impedance (η_0=377Ω), λ_0 the wavelength in the vacuum and ε_{ri} the relative permittivity of the dielectric filling the spaces between the conductors.

The characteristic impedance ratio M (III-6) between both sections of the coaxial SIR has an impact on the physical length of the resonators (III-7) and in the apparition of the first harmonic f_1.

$$M = \frac{Z_1}{Z_2} \tag{III-6}$$

In (III-6) Z_1 is the characteristic impedance of the outer section and Z_2 the characteristic impedance of the inner section.

$$l = \frac{c}{2\pi f_0}\operatorname{atan}\left(\frac{1}{\sqrt{M}}\right) \tag{III-7}$$

$$f_1 = \left(\frac{\pi}{\operatorname{atan}\left(\frac{1}{\sqrt{M}}\right)} - 1\right) f_o \tag{III-8}$$

III.5.2 Two-section Coaxial SIR Filter design

A two-section coaxial SIR filter was defined to fulfill the electrical specifications presented in Figure III.6 with a central frequency of 1.5 GHz and a fractional bandwidth of 1.73 %. To fulfill these requirements a 4th order filter was designed using a Chebyshev synthesis. By performing multipactor analysis with a 4th order filter, we are considering all the possible environments where a multipactor break could occur influenced by the different interactions that can be present like the input/output couplings and inter-resonators couplings.

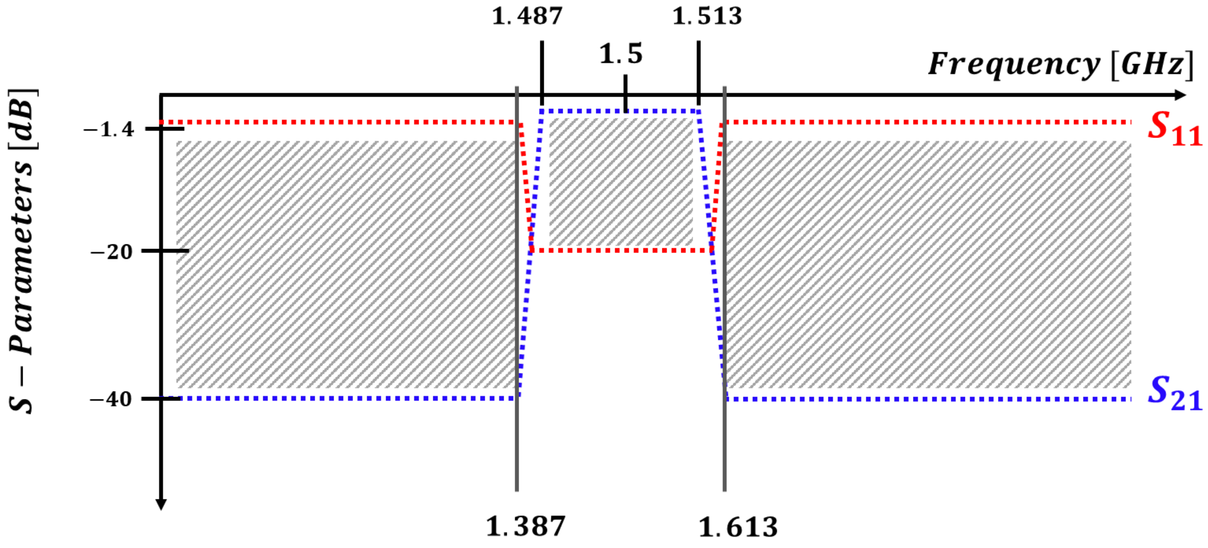

Figure III.6 L-Band electrical specifications for multipactor study

A top view layout of the designed filter is presented in Figure III.7. The position of the input-output connectors is highlighted, and the four resonators are named from R_1 to R_4.

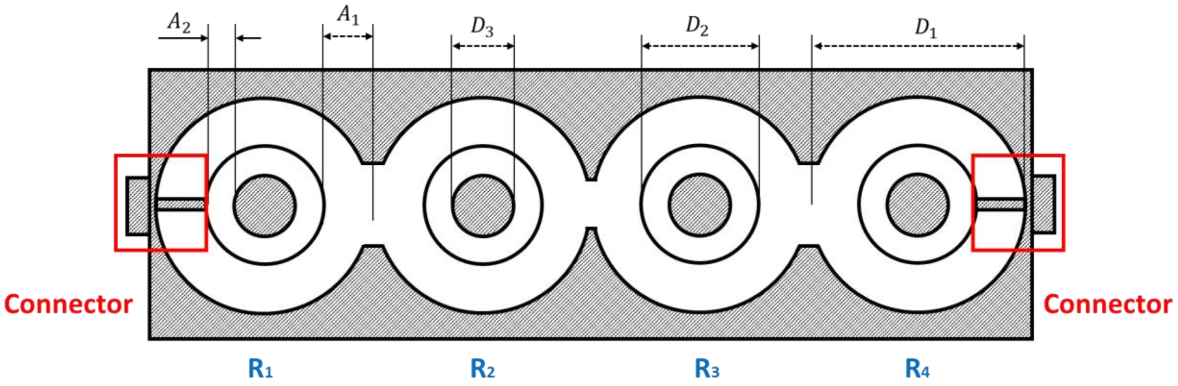

Figure III.7 4th order filter layout

A diameter D_1=50 mm and D_3=2.8 mm were selected. The variable D_2 will vary based on the desired impedance ratio, or distance between conductors. On a first approach, an impedance ratio M=1 was defined with impedances $Z_1 = Z_2 = 50\ \Omega$. The isometric view of 3D model of this configuration is presented in Figure III.8 and a top view of the same model in Figure III.9.

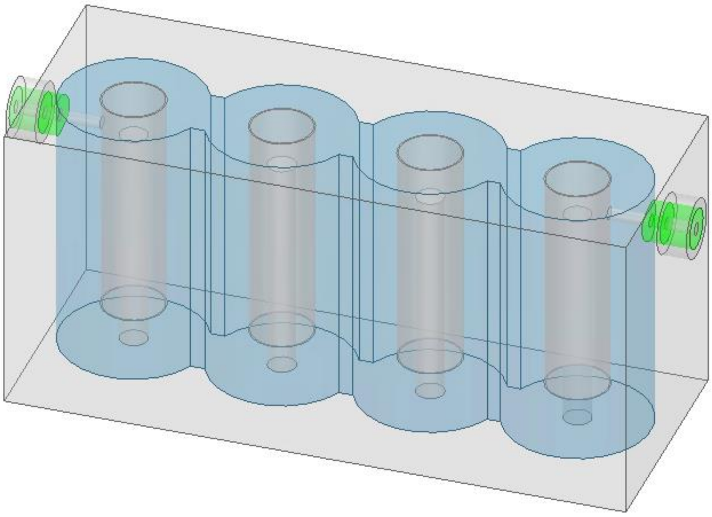

Figure III.8 Isometric view of the simulated 3D model

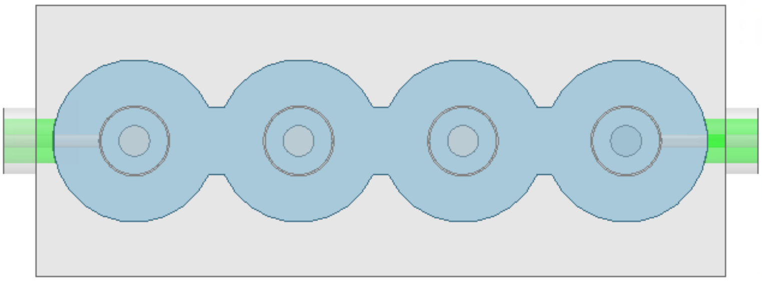

Figure III.9 Top view of the 3D model

III.6 Multipactor analysis

III.6.1 Coupling area $l\varepsilon$ study

The first area to be studied was the coupling area defined by the variable l_ε. On a first sight, this area seems to be critical as a capacitance is formed between the open-ended sections of the resonator and the covers of the resonator [III-1]. If the capacitive effect in this area is significant, the conditions for a multipactor break can be fulfilled and a break can occur.

III.6.1.a Study at 1.5 GHz

Different configurations of the filter were designed with different coupling lengths l_ε varying from 1 to 7 mm. For each of these configurations, the multipactor simulations were done using SPARK3D. Table III.1 presents the specifications of the filter and the different power handlings for each value of l_ε. As the inter-section coupling changes as l_ε does, modifying the electrical length of the resonator, a correction of the physical length l of the resonator must be done to keep the same resonant frequency.

Table III.1 Filter configurations

Order	sections	D_3 [mm]	A1 [mm]	A2 [mm]	l_ε [mm]	l [mm]	Break [W]
4	2	2.8	1.63	3.47	1.0	32.52	1.5
					1.5	32.52	6.8
					2.0	32.25	23.4
					3.0	31.45	23.8
					4.0	30.45	24.0
					5.0	29.52	23.0
					6.0	28.45	25.0
					7.0	27.45	25.0

Using SPARK, it is possible to track the position of the electrons over the time and determine the critical environments of the filter. Figure III.10 presents the position of electrons at different times when the coupling distance l_ε is 1.5 mm and with an input power of 7 W. As it can be observed, the multipactor break occurs in the open circuit area of the first resonator.

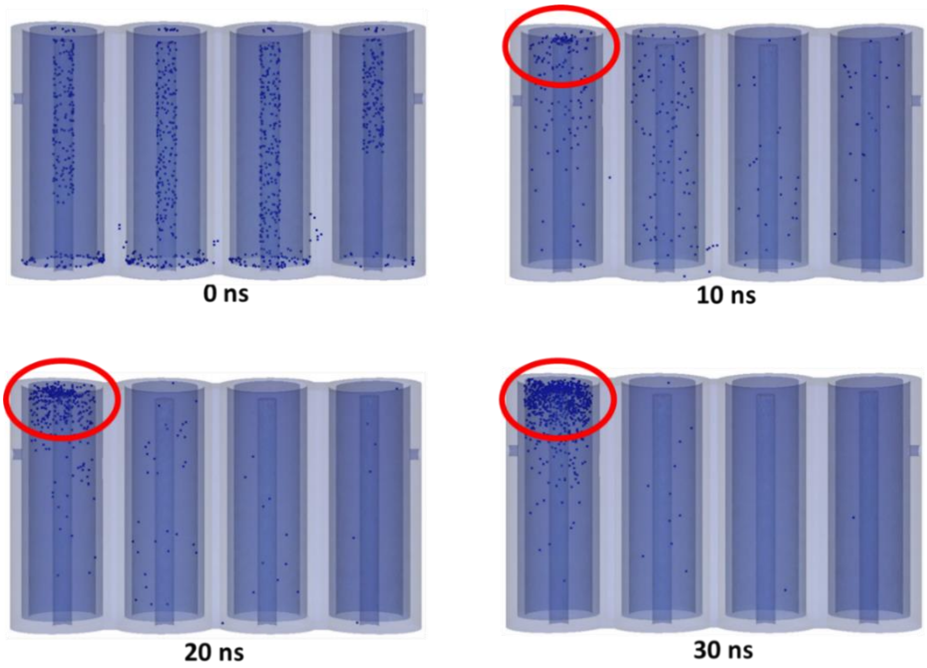

Figure III.10 Electrons position and break with l_ε= *1.5 mm*

A more detailed view on a top view of the structures is presented in Figure III.11. Here it is observed that an important concentration of electrons is present on the center of the resonator, corresponding to the open-end area of the inner section of the resonator.

Figure III.11 Top view of the break with l_ε= *1.5 mm*

A plot of the coupling distance l_ε vs multipactor break power is presented in Figure III.12. As it can be observed, the maximum power handling of the filter is arround 24 W. The maximum power does not increases significantly after $l_\varepsilon = 2\,mm$, meaning that the multipactor break does not occur in this region and for values greater than 2 mm the open circuit region is not critical.

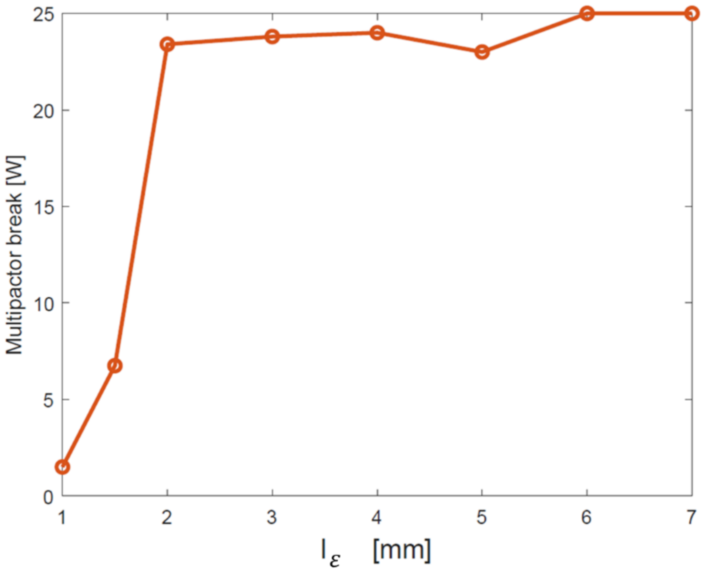

Figure III.12 l_ε Vs multipactor break power for a filter at 1.5 GHz

Based on these results, and to maintain a security factor in the design of the final structure, a coupling distance $l_\varepsilon = 4\,mm$ was fixed for the following studied. By choosing this distance, it was assured that a multipactor break would not occur in this region.

III.6.1.b Study at 2.35 GHz

As a potential application at 2.35 GHz was also contemplated, a validation of the results at 2.35 GHz was done. In this case, 3 lengths were studied: 0.5 mm, 1.5 mm, and 3 mm. As it can be seen, after 1.5 mm the maximum power converges to 12 W. In both cases a $l_\varepsilon = 4\,mm$ could be used.

Table III.2 determination of critical l_ε at 2.35 GHz

Order	sections	D_3 [mm]	A1 [mm]	A2 [mm]	l_ε [mm]	Break [W]
4	2	2.8	1.63	3.47	0.5	0.4
					1.5	13
					3.0	12

III.6.2 Distance between conductors

In this section, different configurations for the distances between conductors A_1 and A_2 were studied. Five different cases were proposed in terms of the distances A_1 and A_2 and in terms of the cross-section areas Σ_1 (blue) and Σ_2 (orange), as presented in Figure III.13

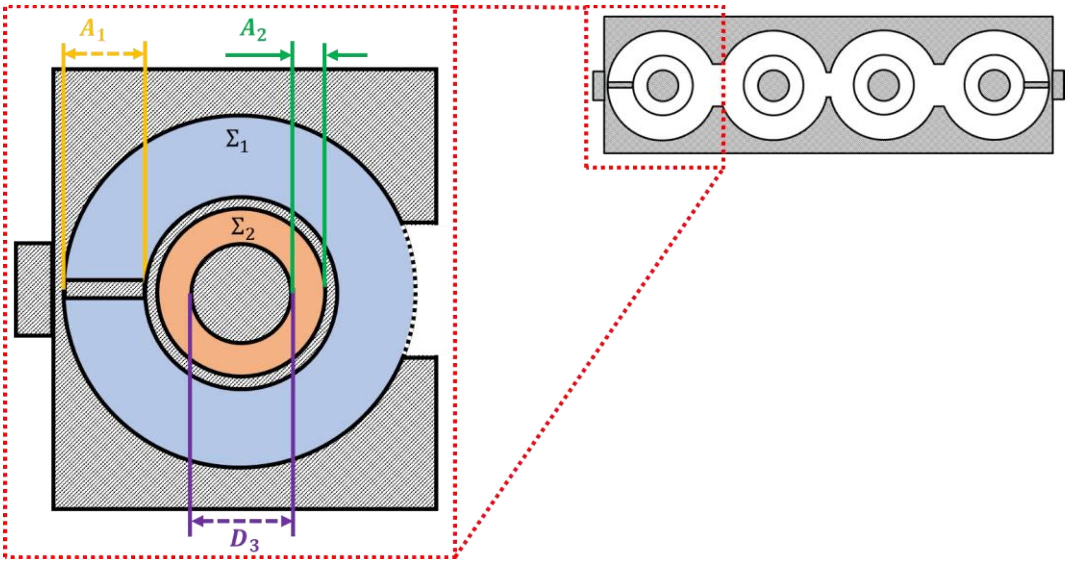

Figure III.13 Detalied view of a coaxial SIR

The five proposed variations were defined as follows:

1) The distance for the inner section A_2 is significantly greater than the distance for the outer section A_1.

2) The cross-section areas of the inner and outer sections are equal
3) The distance between conductors is equal
4) The impedance ratio M is equal to 1
5) The distances of the inner A_2 is significantly smaller than the distance for the outer section A_1.

In all the studied cases, the dimensions D_1=50 mm and D_3=2.8 mm where kept the same. The diameter D_2 was modified to set the different variations.

III.6.2.a Study at 1.5 GHz

The first study was done at 1.5 GHz, the description, and results of the different variations with the informations of impedance ratio, distances, surface area and, multipactor break power is presented for each case in Table III.3

Table III.3 Multipactor break results at 1.5 GHz for different configurations

Variation	$\boldsymbol{M}$	$\boldsymbol{A_2}$ $[\boldsymbol{mm}]$	$\boldsymbol{A_1}$ $[\boldsymbol{mm}]$	$\boldsymbol{\Sigma_2}[\boldsymbol{mm^2}]$	$\boldsymbol{\Sigma_1}$ $[\boldsymbol{mm^2}]$	$\boldsymbol{Break}$ $[\boldsymbol{W}]$
$A_2 = 5A_1$	0.1	5.00	1.00	122.52	48.035	7
$\Sigma_1 = \Sigma_2$	0.24	4.00	2.10	85.45	85.45	34
$A_1 = A_2$	0.45	3.05	3.05	56.05	114.50	12
$M = 1$	1	1.70	4.25	24.03	146.52	2
$A_2 = \frac{A_1}{5}$	2.1	1.00	5.00	11.93	158.62	0.44

From the results of Table III.3 we can see that the best configuration in terms of power handling is the case where the cross-section areas $\Sigma_1 = \Sigma_2$ with a break at approximately 34 W. However, in terms of impedance ratio M, this configuration is not optimal, since this solution corresponds to a M=0.24. As mentioned before, one of the interests in using coaxial SIR resonators is related to size reduction of the structure when M>1.

III.6.2.b Study at 2.35 GHz

As for the 1.5 GHz, the same cases were evaluated at 2.35 GHz and their results are presented in Table III.4. From this complimentary study, it is observed that the behavior of the multipactor break is similar at different frequencies. The maximum power handled by the structures occurs at the equal-areas configuration with 34 W at 1.5 GHz and 46 W at 2.35 GHz.

Table III.4 Multipactor break results at 2.35 GHz for different configurations

Variation	M	$A_2[mm]$	$A_1[mm]$	$\Sigma_2[mm^2]$	$\Sigma_1[mm^2]$	$Break\ [W]$	$Order$
$A_2 = 5A_1$	0.1	5.00	1.00	122.52	48.035	39	10
$\Sigma_1 = \Sigma_2$	0.24	4,00	2.10	85.45	85.45	46	6
$A_1 = A_2$	0.45	3.05	3.05	56.05	114.50	37	8
$M = 1$	1	1.70	4.25	24.03	146.52	10	5
$A_2 = \frac{A_1}{5}$	2.1	1.00	5.00	11.93	158.62	2	4

III.6.2.c Metallization thickness

In the previous section, it was determined that the ideal configuration, in terms of power handling, was the case with equal surface areas. However, the metallization thickness of the middle conductor C_2 was not taken into account. In this section, the metallization thickness, noted as met_{th} in Figure III.14 is considered in the simulations. A metallization thickness of 1 mm is used as it corresponds to the minimum thickness that can be achieved by the available fabrication process.

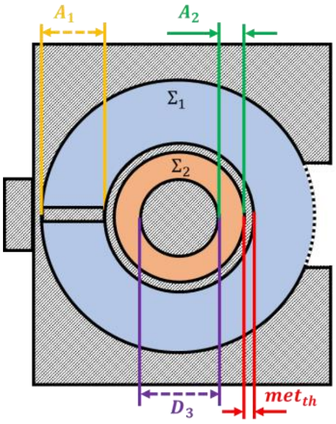

Figure III.14 Detalied view of a coaxial SIR including metallization thikness

Table III.5 presents the studied cases, and their results, considering this new variable. As in the previous section it was already determined that the best case was $\Sigma_1 = \Sigma_2$, we studied different configurations around it. The studied configurations were defined by changing the distance A_1 and A_2 between conductors by steps of 0.25 mm. For example, when A_1 was reduced by 0.25 mm, A_2 was increased and in consequence $\Sigma_1 < \Sigma_2$. When the step is of 0.5 mm the studied case corresponds to $\Sigma_1 \ll \Sigma_2$.

Table III.5 Multipactor break results at 1.5 GHz for different configurations considering metal thickness

Variation	$A_2\ [mm]$	$A_1\ [mm]$	$\Sigma_2 [mm^2]$	$\Sigma_1\ [mm^2]$	$Break\ [W]$
$\Sigma_2 \ll \Sigma_1$	2.97	2.13	53.83	86.12	20
$\Sigma_2 < \Sigma_1$	3.22	1.88	60.89	77.48	28
$\Sigma_2 = \Sigma_1$	3.47	1.63	68.35	68.46	24
$\Sigma_2 > \Sigma_1$	3.72	1.38	76.19	59.05	17
$\Sigma_2 \gg \Sigma_1$	3.97	1.13	84.43	49.23	9

When observing the previously presented results, the first thing that was observed is the difference between the maximum power with the configuration $\Sigma_1 = \Sigma_2$. In the first case, with no metallization thickness, the multipaction level was reached at 34 W, while with a more realistic model this maximum power drops by 10 W. However, this result is in coherence with the reduction of the distances between conductors. In addition, it was also observed that the maximum power handled was not anymore at the equal-areas case, but when the area of the outer section was slightly greater than the inner section of the coaxial SIR resonator.

In order to gain a better understanding of the relation between the surface area and the power handling of the structure, the results were plotted Figure III.15 in using the surface ratio Σ_2/Σ_1 on the x-axis. Although the maximal power handling of the structure does not occur exactly at the $\Sigma_2/\Sigma_1 = 1$ case, it is a good starting point when maximizing power handling of a filter is crucial.

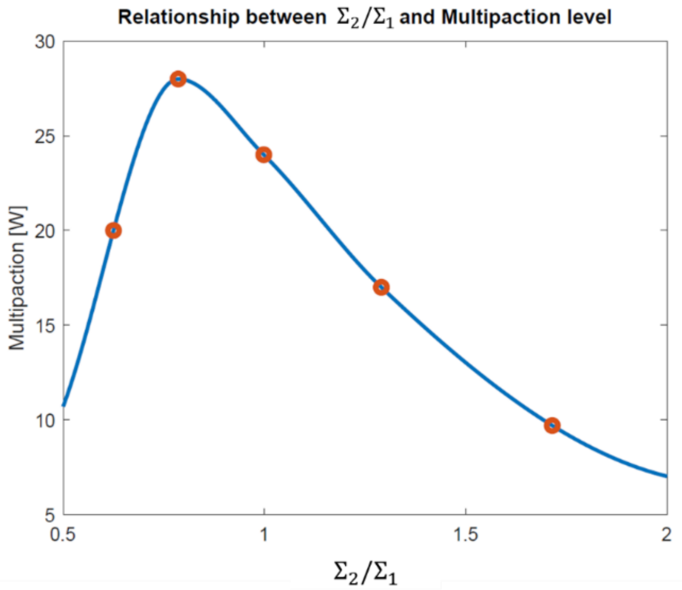

Figure III.15 Relation between the normalized surface area and the power handling

In addition to the break level analysis of the structure, the behavior of the electrons at the break was analyzed for the equal areas and maximum power configurations. Figure III.16 shows a front view of the structure with particles positions at different times for the case $\Sigma_1 = \Sigma_2$. Here, it is observed that multipactor break occurs in two different regions of the same resonator.

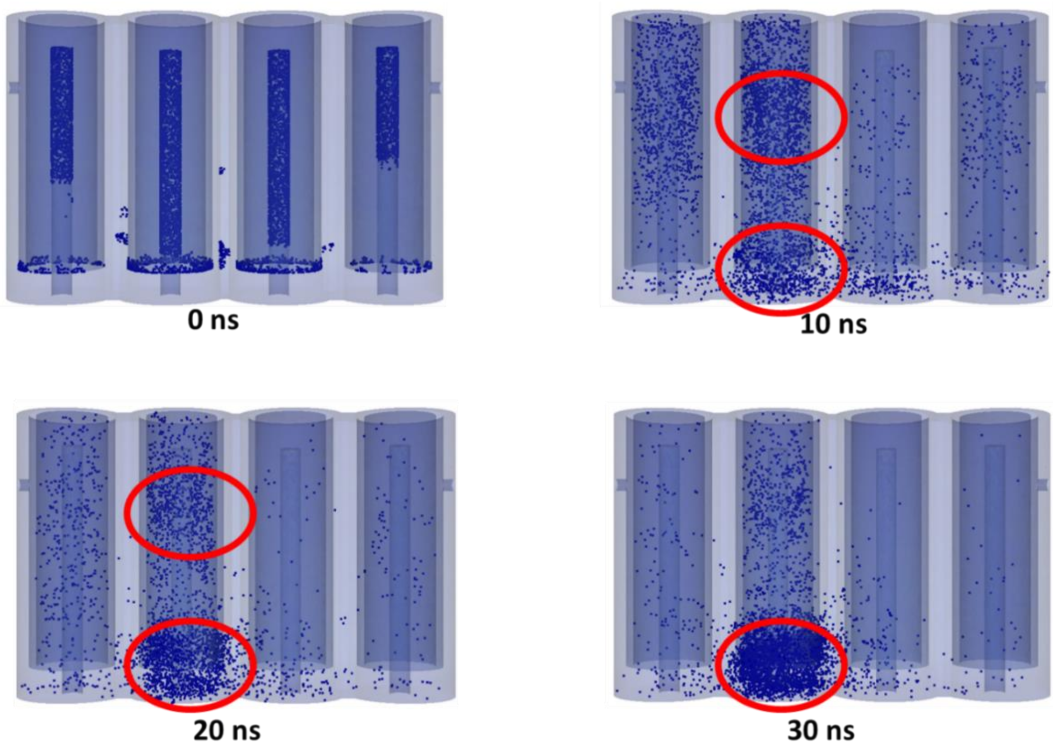

Figure III.16 Positions of the electron avalanche at different times for the case $\Sigma_1 = \Sigma_2$

The first identified area is the region corresponding to the inner section of the resonator, area denoted by Σ_2 as seen in Figure III.17. The break in this region occurs between the conductors C_2 and C_3 but not at the level of the open circuit of the C_3 conductor. The second region occurs in the Σ_1 area, at the lower part of the resonator between conductors C_1 and C_2. This can be constated when observing the electrons concentration in Figure III.17, since the clouds of electrons are present between the conductors and not at the level of the sections coupling.

In both cases, the breaks occur between cylindrical conductors and not in the open-ended parts of the conductors as it was intended when setting $l_\varepsilon = 4\,mm$. This can be validated by observing in detail Figure III.17, since there is no cloud of electrons in the coupling regions as in Figure III.11.

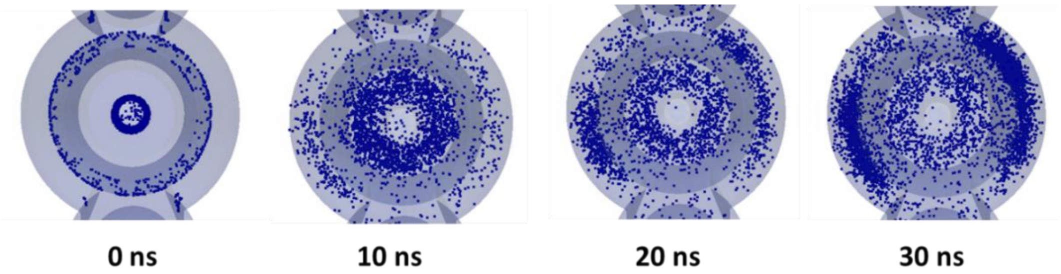

Figure III.17 Top view of electrons position of resonator 2 at different times for the case $\Sigma_1 = \Sigma_2$

The electrons positions were also studied for the configuration with maximum power handling $\Sigma_2 < \Sigma_1$. With a break at 28 W, the tracking of the electrons showed that the discharge occurred only in one region of the coaxial SIR. As it can be seen in Figure III.18, the avalanche of electrons is between conductors C_2 and C_3. The top view of resonator number 2 from Figure III.19 shows a better view of the particle's distribution. As in the previous case, at $l_\varepsilon = 4\ mm$ the coupling area is not critical.

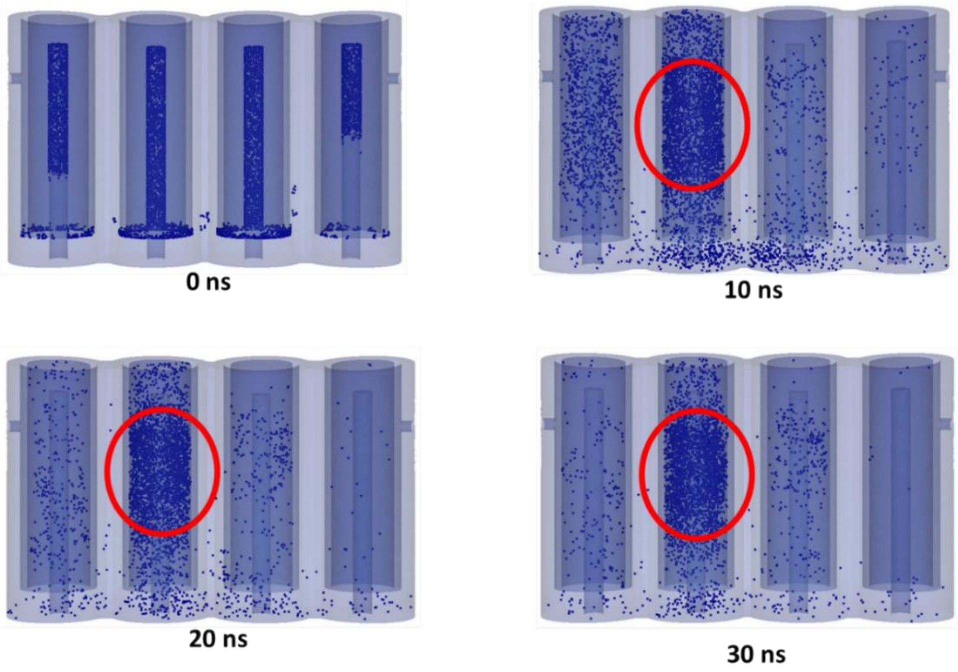

Figure III.18 Positions of the electron avalanche at different times for the case $\Sigma_2 < \Sigma_1$

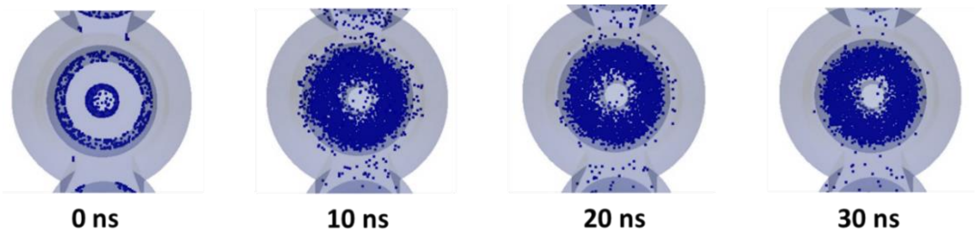

Figure III.19 Top view of electrons position of resonator 2 at different times for the case $\Sigma_2 < \Sigma_1$

In the design of a multipactor test structure it is convenient to have a well-defined break area as it is the case $\Sigma_2 < \Sigma_1$. This will simplify the analysis and study of the use of carbon coatings in the structure since any changes in the power handling could be attributed to the coating and not to other sources.

III.6.3 Inter-Resonator coupling

We also wanted to determine the impact of inter-resonators coupling on multipactor break, as we saw on the previous results a break can occur in the external section of a resonator but not where the coupling iris are present. To study this, a 4th order filter with the same electrical specifications was designed, but the inter resonators coupling was done with metallic bars in contact with the C_2 conductors of the resonators as presented in Figure III.20 and Figure III.21.

In this approach, the couplings were modified by changing the diameter of each bar. These coupling bars were all placed at the same height near the short-circuit of conductor C_2 so they would not perturbate the coupling between each resonator section.

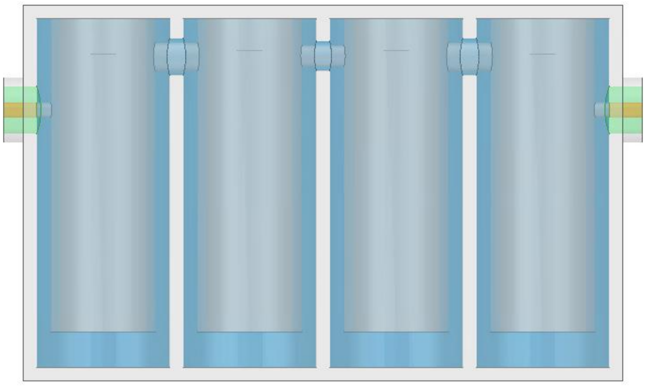

Figure III.20 Front view of the 4th order filter with bar couplings

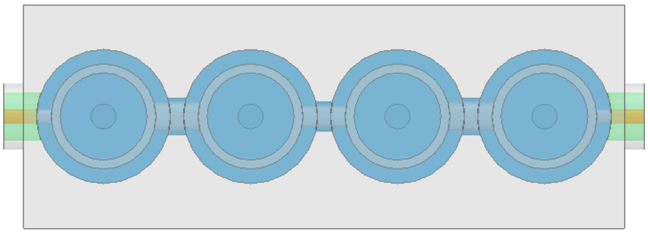

Figure III.21 Top view of the 4th order filter with bar couplings

The results of these simulations and their comparison with their equivalent filter using an iris coupling are presented in Table III.6 . Although the maximum power for each configuration is higher than their iris-coupled equivalent, this does not represent a significant improvement to consider the implementation of this coupling method.

Table III.6 Power handling comparison between iris and bar coupled filters

Variation	***Iris coupling Break*** $[W]$	***Bar coupling Break*** $[W]$
$\Sigma_2 \ll \Sigma_1$	20	24
$\Sigma_2 < \Sigma_1$	28	30
$\Sigma_2 = \Sigma_1$	24	32
$\Sigma_2 > \Sigma_1$	17	23
$\Sigma_2 \gg \Sigma_1$	9	13

Additionally, when observing the electrons distribution in the structure for the equal areas case in Figure III.22, the break areas are the same as the ones identified previously. Having a completely closed cavity does not significantly modify the global performance of the structure. It can be said that the inter-resonator coupling does not have a significant impact on the power handling capabilities of the structure.

Additionally, the physical implementation of this coupling structure is more complicated to fabricate since the coupling bars between resonators must be isolated from the resonator walls. Implementing this strategy will elevate the fabrication cost without including a benefit in the performance of the structure.

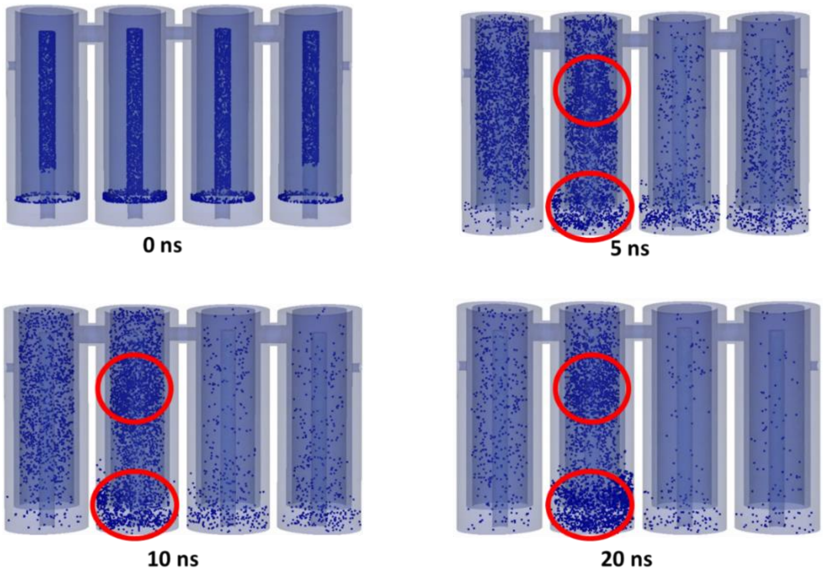

Figure III.22 Positions of the electron avalanche at different times for the bar coupled filter

III.6.4 Alternating resonators

The disposition of the resonators inside the filter is also studied. Since the open-circuit section of all the resonators were at the same level, we wanted to determine if this could impact the power handling of the structure. To assess this, two variations were studied, the first one alternates the position of resonators 2 and 3 as presented in Figure III.23 (a). In the second configuration all the resonators are alternated in a way that the open end of each resonator is between the short-circuit end of the previous and next resonator as presented in Figure III.23 (b).

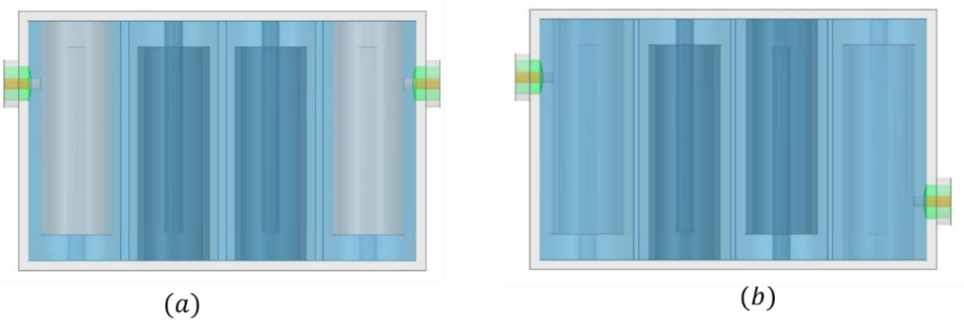

Figure III.23 Front view of the two configurations of the alternating resonators filters

These filters correspond to the best multipactor break configuration $\Sigma_2 < \Sigma_1$ with a reference value of 28 W. The SPARK3D results showed that by alternating the position of the resonators the multipactor thresholds were of 32.2 W for the case (a) and 31.4 for the case (b). In both configurations, the break is also present inside the inner section of the coaxial SIR as it can be seen in Figure III.24 for case (a), and in Figure III.25 for the case (b).

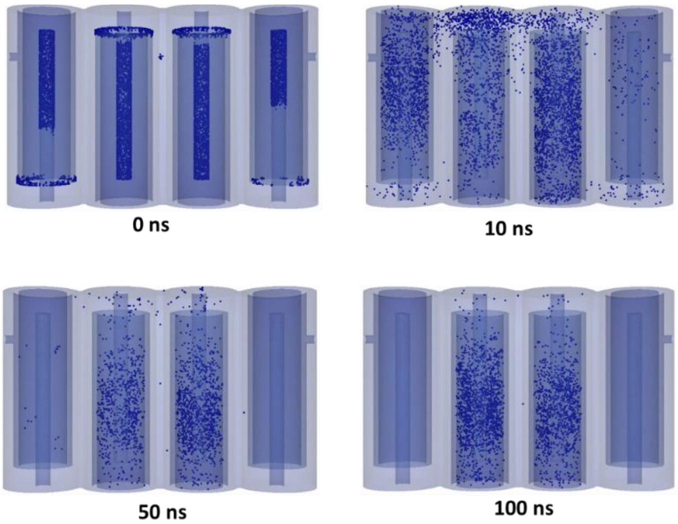

Figure III.24 Electrons position over time in the first alternating resonators filter

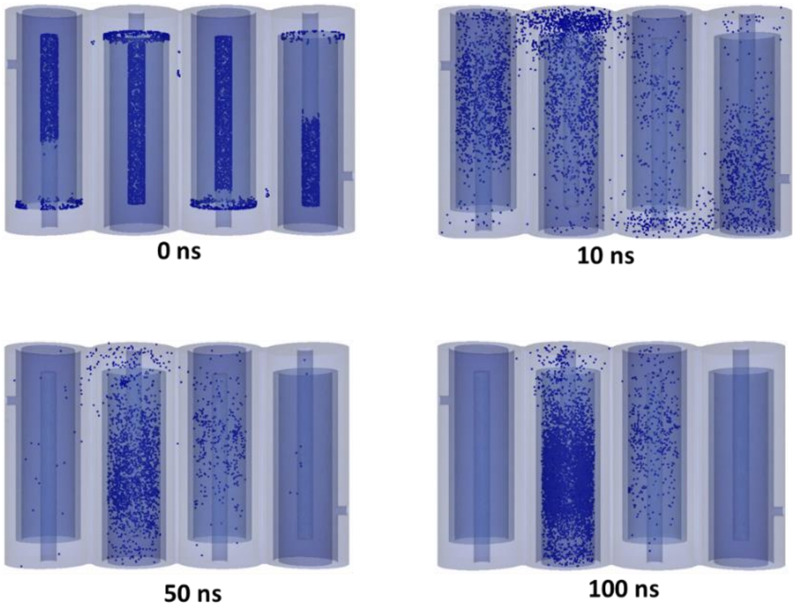

Figure III.25 Electrons position over time in the second alternating resonators filter

The implementation of both configurations of the alternating resonators showed that the versatility of the coaxial SIR resonators giving and additional freedom degree when designing filters. Additionally, the versatility of this resonator topology is also maintained in the power handling capabilities of the structures. As the resonators are kept the same and only the coupling between resonators was modified, the selected dimensions are a good choice for designing a robust and trustable multipactor test structure.

III.6.5 Squared coaxial section

In the coaxial cylindrical resonator, the distance between any point of the central conductor to the external conductor is the same. In the squared coaxial configuration this is not the case and we wanted to determine the impact of changing the external conductor of the outer section to a squared coaxial. Here, the distance between any point of the central conductor to the external metallization will not be the same.

In this version, based on the configuration $\Sigma_2 < \Sigma_1$ and keeping a width of 1 mm for conductor C_2 , the length of the side of the coaxial squared section is equal to the diameter of its equivalent circular configuration as presented in Figure III.26, and the isometric and top views of the 3D model are presented in Figure III.26.

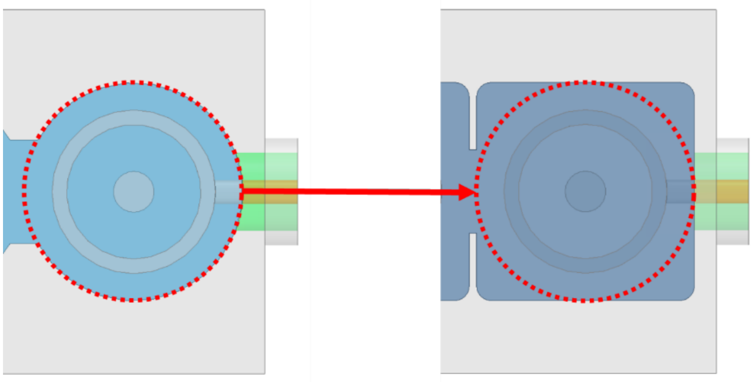

Figure III.26 Equivalence between the circular and squared coaxial sections

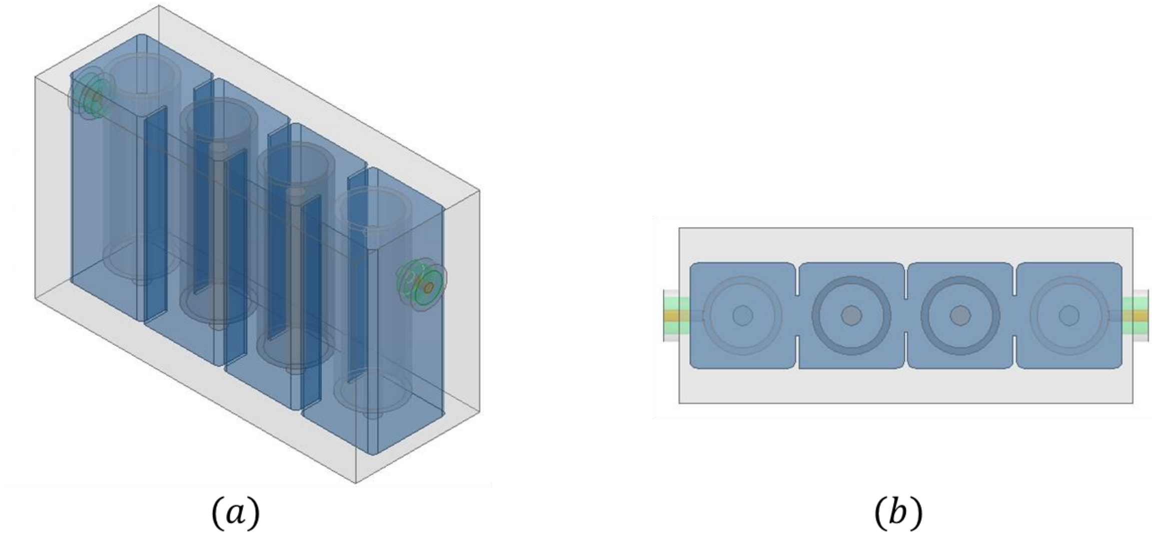

(a) (b)

Figure III.27 (a) Isometric and (b) top view of the squared coaxial section filter

With a maximum power of 33 W, the squared coaxial section did not improve the power handling significantly, as the multipactor break occurs inside the inner section of the resonator (Figure III.28).

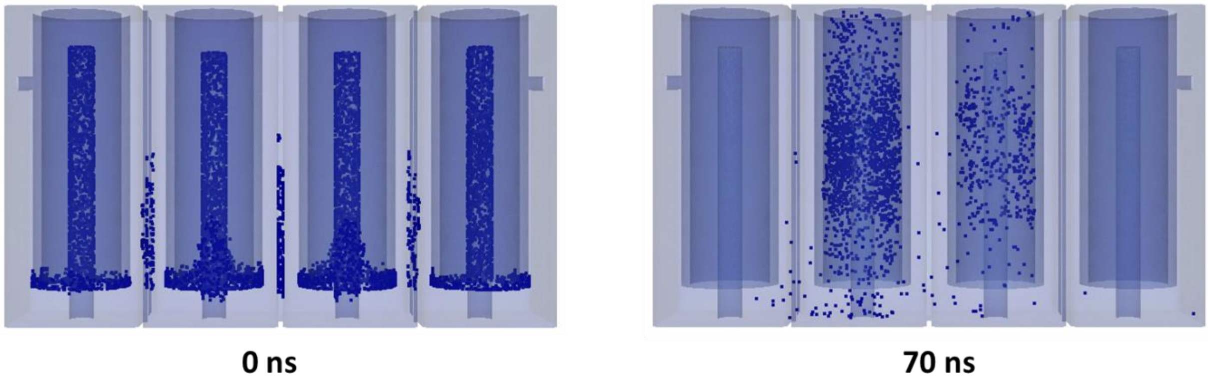

Figure III.28 Electrons position over time in the squared section filter

III.6.6 Carbon coatings impact

Once the performance of the structure was studied, and the critical variables of the filter were identified, the study of the impact of coating the structure with carbon was done. To do so, the two-section stepped impedance resonator was divided in 5 different areas of interest. The first area corresponds to the central conductor of the inner section, noted C_3. The second one is the external conductor of the inner section, corresponding to the inner part of the conductor C_2. Third, is the external area of the conductor C_2, which represents the central conductor of the outer section. The outer conductor C_1 of the outer section was defined as the fourth area, and finally, both top and bottom ends of the resonator were defined as the fifth area of interest.

Seven different configurations were studied as presented in Figure III.29. Starting with configuration number 1, corresponding to the filter with no coating, and going up to configuration number 7, which corresponds to the entire structure coated. Areas highlighted with red represent the coated area of each configuration. In configurations 3 and 4, a coating is included in the inside of the highlighted conductor C_2, and in configuration 5 the coating is done at the outer part of this conductor. Configuration 6 considers only a coating in the external conductor C_1 of the external section, and finally, in configuration 7, a coating is simulated in all the metallizations.

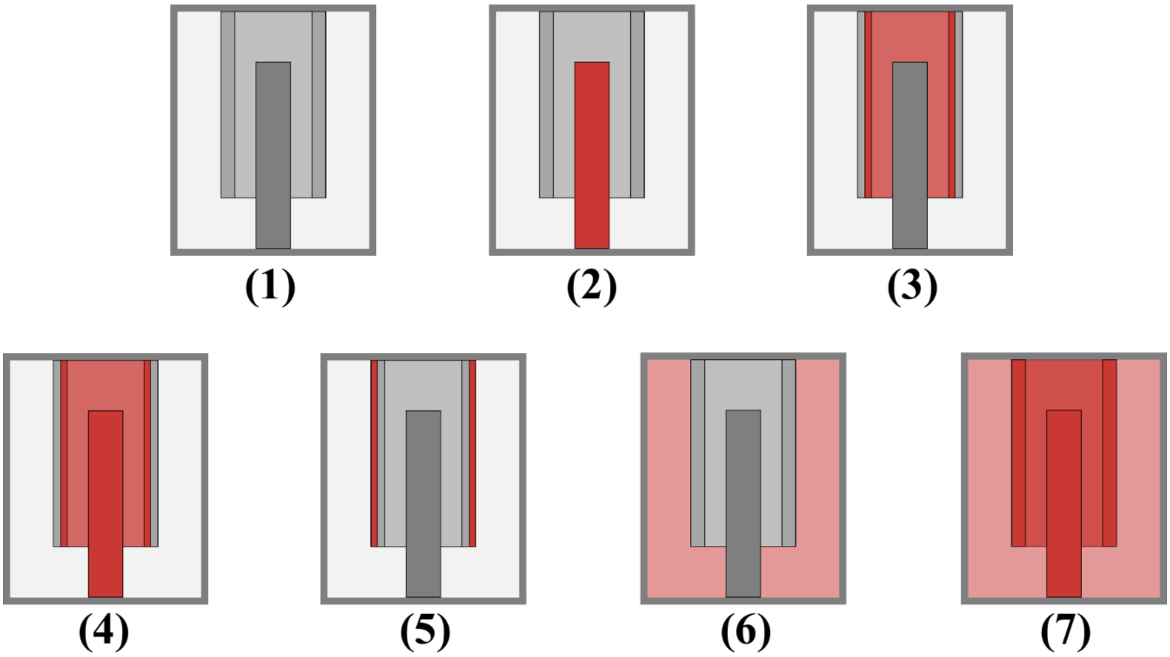

Figure III.29 coating areas definitions

III.6.6.a Whole structure coating

First, a power handling comparison between no coating (case 1) and a complete structure coating (case 7) was performed. It was important to determine if the carbon coating would have a relevant impact on the apparition of multipactor in the structure. Simulations performed with SPARK 3D were done using the measured SEY of the carbon coating presented in Chapter II. In some cases, the results obtained with SPARK3D were compared to a simulation done with CST-PIC. The comparisons are made for specific cases from previous sections.

The first analyzed cases correspond to the equal areas ($\Sigma_1 = \Sigma_2$) and the maximum break ($\Sigma_2 < \Sigma_1$) configurations. Results are presented and compared on Table III.7

Table III.7 Filter multipactor results with SPARK 3D comparison between no coating and a complete carbon coating for the equal-areas and maximum-break configurations

CASE	$\boldsymbol{A_2}\ [\boldsymbol{mm}]$	$\boldsymbol{A_1}\ [\boldsymbol{mm}]$	$\boldsymbol{Silver}\ [\boldsymbol{W}]$	$\boldsymbol{Carbon\ coating}\ [\boldsymbol{W}]$	$\boldsymbol{Gain}\ [\boldsymbol{dB}]$
$\Sigma_2 < \Sigma_1$	3.22	1.88	28	58	3.16
$\Sigma_2 = \Sigma_1$	3.47	1.63	24	40	2.21

As it can be observed, the use of a carbon coating all over the structure increases the power handling of the structure in both cases. As PIC simulations require more computational time, this will only be used for final validation of the structures.

Later, the filters of different sizes (A_1 and A_2) were compared to determine if the gain in the maximum power handling was the same or it changed in function of the size of the structure by always keeping the same resonance frequency, so only the diameters would be increased and keeping the same resonators length. As it is observed in the results presented in Table III.8, the maximum power handled by the structure increases as the size of the structure does. While the benefit of using a carbon coating is of 3 dB on the base case, for a structure of double the size, this benefit is an increase of almost 13 dB.

Table III.8 Filter multipactor results with SPARK 3D comparison between no coating and a complete carbon coating for the maximum-break configurations at different sizes

CASE	$\boldsymbol{A_2}\ [\boldsymbol{mm}]$	$\boldsymbol{A_1}\ [\boldsymbol{mm}]$	$\boldsymbol{Silver\ Break}\ [\boldsymbol{W}]$	$\boldsymbol{Coating\ Break}\ [\boldsymbol{W}]$	$\boldsymbol{Gain}\ [\boldsymbol{dB}]$
$\Sigma_2 < \Sigma_1$	3.22	1.88	28	58	3.16
1.065 x	3.429	2.067	44	99	3.52

CASE	$A_2\ [mm]$	$A_1\ [mm]$	$Silver\ Break\ [W]$	$Coating\ Break\ [W]$	$Gain\ [dB]$
1.15 X	3.703	2.312	47	162	5.36
1.25 X	4.025	2.6	48	168	5.44
1.50 X	4.83	2.82	54	248	6.62
2.00 X	6.44	4.76	165	3251	12.95

From the results in Table III.8, we also observed that a small increase in the size of the structure had a significant impact on the power handling of the filter and keeping the 3 dB power gain from the base case.

Additionally, for the squared coaxial section and the alternating resonators, the multipactor threshold was improved by 3 dB for a complete structure coating and $\Sigma_2 < \Sigma_1$. These results are in coherence with its equivalent filter in an all circular coaxial since the electrons avalanche occurs in the inside sections of the resonators.

III.6.6.b Partial carbon coatings

Once we had validated that a complete carbon coating of the structure increased the maximum power handling of different configurations of a 4th order filter, we studied the impact of coating the structure with carbon using CST-PIC. For this study, the filters were designed with a $\Sigma_2 < \Sigma_1$ configuration and the size increase by a factor of 1.065.

First, we studied the impact of the order of the filter by simulating 3 different filters of orders 2, 4 and 6 with electrical responses that satisfied the specifications as presented in Figure III.30. From this comparison it was observed that a second order filter could satisfy the electrical specifications with the lowest insertion losses of the 3 studied filters.

For each filter, the study cases (1), (2), (3), (4) and (7) were evaluated (Figure III.31). It was found that the order of the filter had an impact on the overall power handling of the structure in all the different configurations. The second order filter had a better power handling compared to the fourth and sixth order cases. Also, the gain of the use of carbon coating was maximized for the second order structures as it can be seen in Figure III.31.

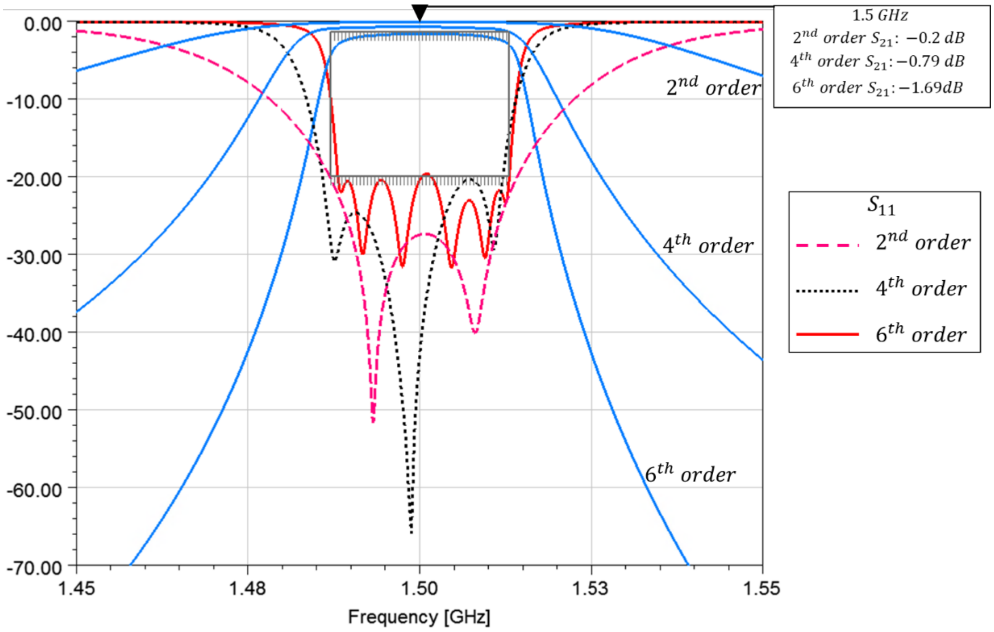

Figure III.30 Frequency response comparison for 2^{nd}, 4^{th} and 6^{th} order filters

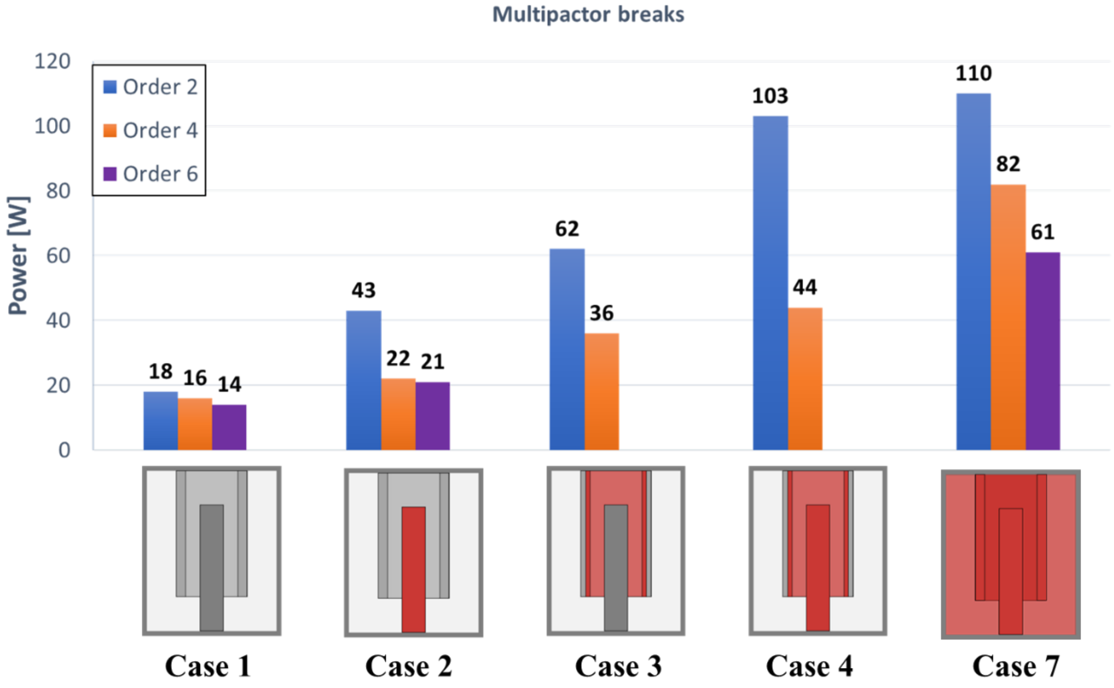

Figure III.31 Power results for filters of different order and different coating areas.

For the partial coatings inside the metallizations of the inner sections (cases (2) and (3)), an important difference is observed depending on where the coating was added, contrary to the first simulations on a simple coaxial transmission line (Figure III.3). This difference can be explained by the occurrence of single sided multipactor on the conductor C_2 and since the probability of reaching the central conductor is lower than reaching the external conductor of the coaxial section.

However, for the second order filter, the benefit of coating the inner conductor results in a power gain over 3 dB, which agrees to the desired gain for this study. It is important to remember that, for the fabricated structure, a complete carbon coating cannot be done, so the choice of a particular coating area must be done. Based on these results, and on the impact that the coating could have on the quality factor of the filter, the coating of the central conductor (case 2) seems a good choice.

As the 2nd order filter presented the largest difference between no coating and a coating on the inner section (case 2), this was the chosen order to continue the study. In terms of fabrications and carbon coating, the 2nd order filter is easier to fabricate and to coat considering that there is also a physical limitation in the size of the samples to be coated.

Finally, based on the tendency observed on the 4th order filters, the size of the 2nd order filter was modified to determine the impact of size in the overall power handling. Figure III.32 shows the behavior of the power handling of four 2nd order filters with different size footprints. For each size filter, 5 coating cases previously presented were also studied, starting from a no coated structure and ending with a complete coating case.

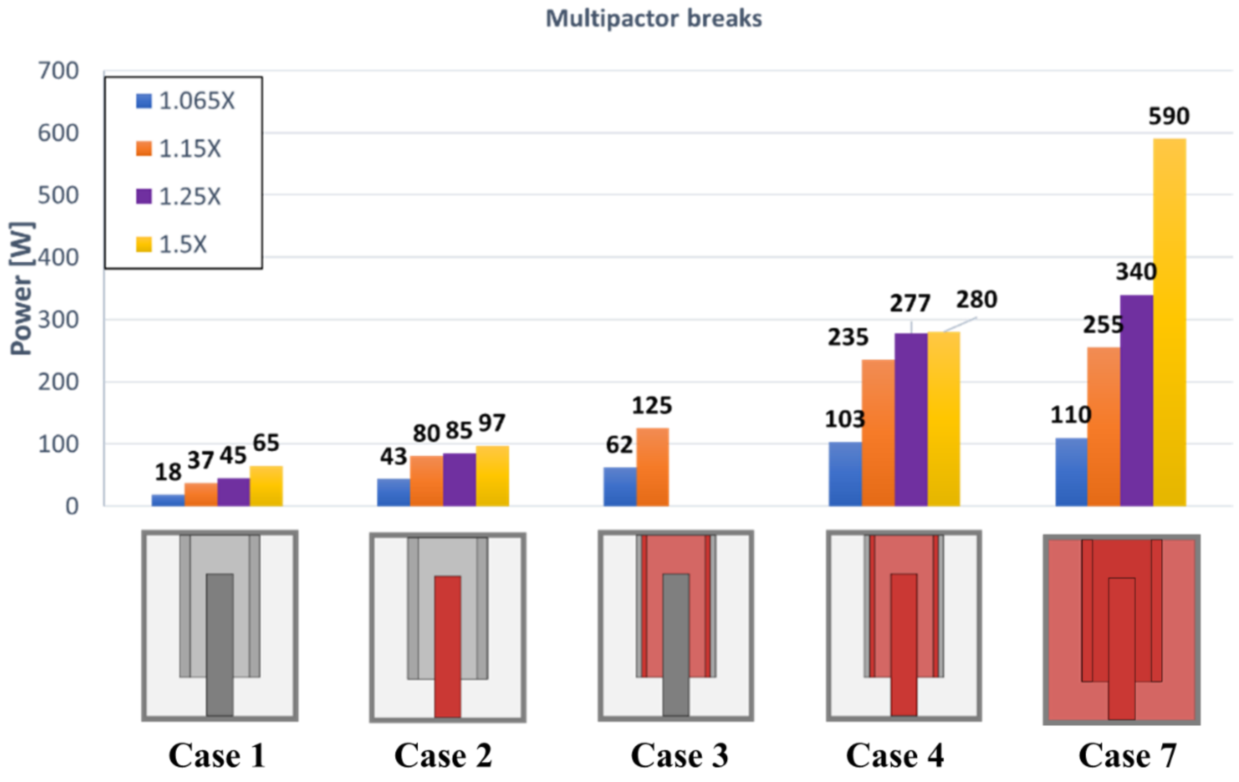

Figure III.32 Power handling of multiple 2nd order filters of different sizes

III.7 Defined structure

Considering that a complete coating of the structure was not possible due to the high complexity of the structures, the selection of the area to be coated was based on the simplicity of the geometry and the potential impact on the multipactor break. The central conductor of the inner section was selected as the carbon coating could be possible. In order to choose the best configuration, Table III.9 compares the maximum power handling for the 2nd order filters of different sizes for all silver and the only central conductor coated cases.

Table III.9 power handling comparison for 2nd order filters of different sizes

	All silver $[\boldsymbol{W}]$	**Case 1** $[\boldsymbol{W}]$	$\boldsymbol{\Delta\ Power}\ [\boldsymbol{W}]$	$\boldsymbol{Gain}\ [\boldsymbol{dB}]$
1.065 ×	18	43	25	3.78
1.15 ×	37	80	43	3.35
1.25 ×	45	85	40	2.76
1.5 ×	65	97	32	1.73

The selected configuration should present the highest difference between the power handlings ($\Delta\ Power$) in order to clearly differentiate both breaks. Also, the maximum power to be measured should not be greater than 100 W, as the test bench at Thales Alenia Space has a measuring range from 0 to 400 W and a security margin of 6 dB must be respected. With this information, and the results on Table III.9, the 1.15 × configuration was chosen as it fulfilled all the requirements. Additionally, a power gain of 3.35 dB between both cases is a significant result that proves the advantage of using nanoscale carbon coatings. As the objective of this structure was to validate the complete set of simulations previously presented, a robust structure, with the minimum perturbator effects was preferred.

III.7.1 Designed structure

The electromagnetic model of the selected configuration is presented in Figure III.33 and its corresponding electrical response in Figure III.34.

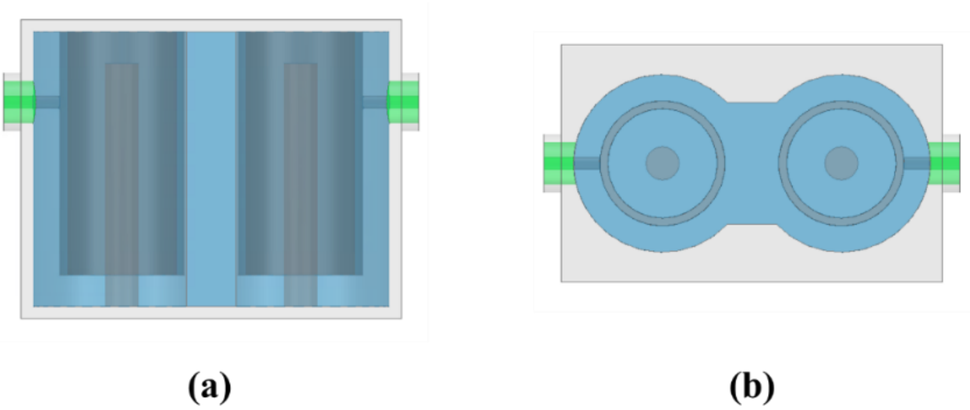

Figure III.33 Electromagnetic model of the designed test structure

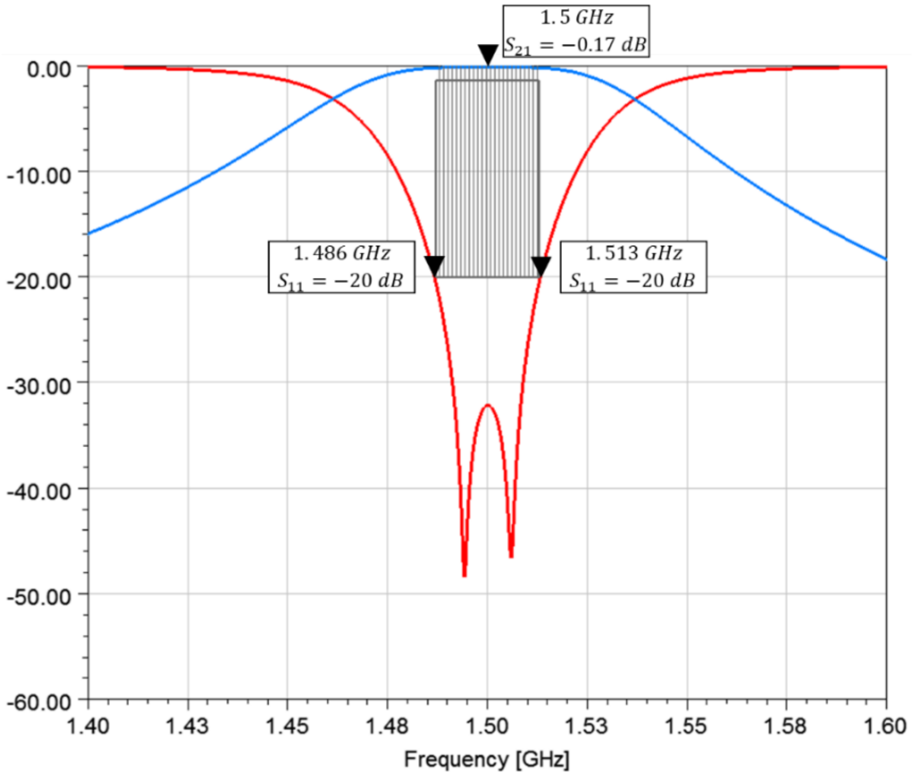

Figure III.34 Electrical response of the designed test structure

The final design of the structure consisted in a 3 parts 2nd-order filter as presented in Figure III.35. This two-section coaxial SIR filter is made up from a cover, body, and bottom parts. The bottom part corresponds to a cover and the C_3 conductors, the top part makes up a cover and the C_2 conductors and finally, the body part is the C_1 conductors of the structure. The structure is designed to have the multipactor break in the inner section of the filter, defined by the distance A_2.

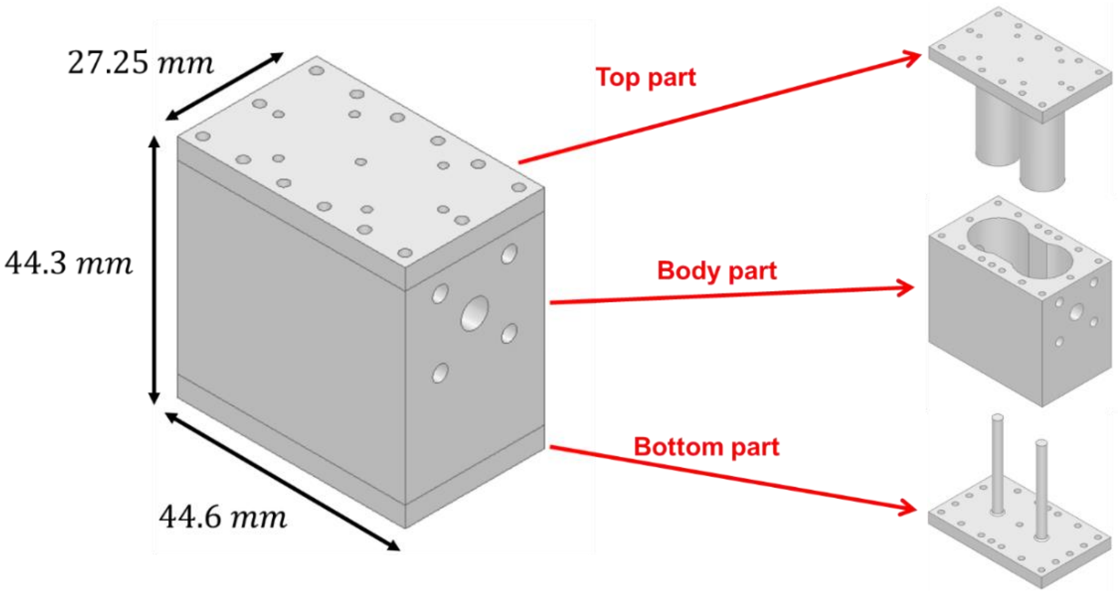

Figure III.35 Main component of the designed structure

As this structure is going to be used to measure the advantages of carbon coatings in multipactor protection. This modular design will allow us to test the structure with and without carbon coatings on the C_3 conductor by only changing the bottom part.

III.7.1.a Tuning screws

Tuning screws were added to the final design of the filter to compensate any fabrication defect under the fabrication tolerance of $\pm 50\mu m$. Two screws for tuning the frequency of each resonator, one at the coupling iris, and one for every connector were added at the short circuit area of the resonators (top cover), where they would have a lower impact on the electrical field, and therefore, a lower perturbation of the overall structure specially the multipactor threshold.

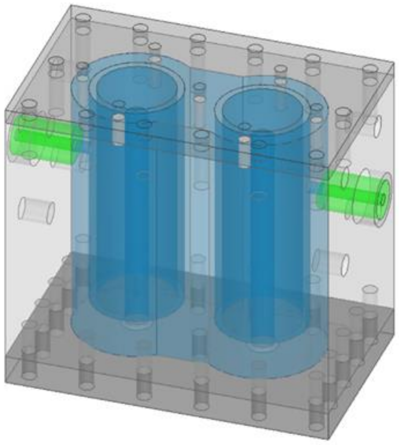

Figure III.36 Complete electromagnetic model, with tuning screws, of the test structure

Additionally, multipactor simulations were done using SPARK3D to validate that the use of the tuning screws would not modify the power handling capabilities of the structure. Silver ECSS was used for these simulations as their objective was to compare difference between power handling results rather than to obtain a specific value. As for previous simulations, the SEY curve used was based on the carbon characterization presented in chapter II, results might vary as the first crossover energy E_1 and δ_{max} are different.

Table III.10 and Table III.11 presents the results of the filter without tuning screws and the results with tuning screws respectively.

Table III.10 Multipactor break and order for the test structure without tuning screws

CASE	$\boldsymbol{Multipactor\ Break}$	$\boldsymbol{Multipactor\ Order}$
All silver	122	7.64
All Carbon	291	3.15

Table III.11 Multipactor break and order for the test structure with tuning screws

CASE	$\boldsymbol{Multipactor\ Break}$	$\boldsymbol{Multipactor\ Order}$
All silver	110	7.36
All Carbon	288	3.09

When comparing both tables, it can be seen that power handling performances of both models are very similar. In both cases, multipactor orders and power breaks are comparable, despite a 10 W drop for the silver filter with screws.

III.7.2 SEY sensitivity analysis

Finally, as carbon coating SEY could vary for different deposition runs, a sensibility analysis was done considering the measured SEY curve presented in chapter 2. This was done to make sure that the power handling of the test structure will not change drastically if the SEY of the coatings is not identical to the one of the measured samples. The four different curves had variations on their values of E_1, E_{max}, δ_{max} and E_2 based on the curve used for the reference studies.

From these variations two are of main interest. The first one refers to the “coated_1” SEY with the highest first crossing energy level E_1 and the lower δ_{max}, assuming an optimistic scenario (blue curve). On the other hand, the “coated_4” models a worst-case scenario with the lowest E_1 and the highest δ_{max} (yellow curve). These SEY curves are presented in Figure III.37.

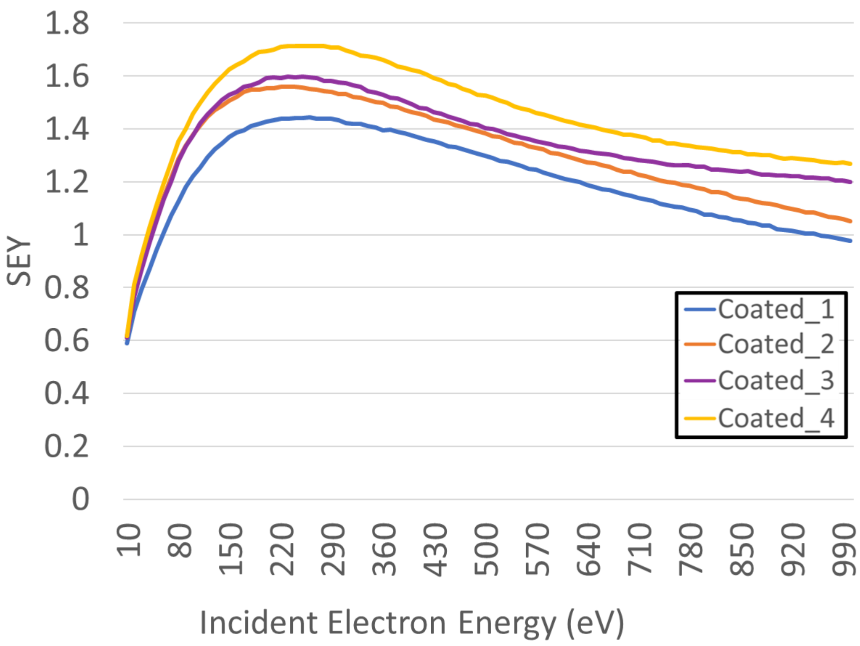

Figure III.37 SEY curves for the sensitivity analysis

Table III.12 presents multipactor thresholds with the different SEY curves. Coatings on C_3 and all the structure were analyzed for both cases of main interest as there are both extreme cases. For the other two cases in between only the C_3 coating was simulated. From these results we observe that for the optimistic scenario the multipactor threshold is of 106 W, being at the limit of the 100 W determined for the experiment. On the other hand, in the worst-case scenario, the multipactor threshold decreases only by 6 W when compared to the 80 W of the reference design (Table III.9), maintaining a 3 dB gain between the 2 coating cases.

Table III.12 Power handling results for the sensitivity analysis

		Power [W]	
Filter	SEY	C_3 coated	All carbon
Filter 1.15 X	—Coated_1	106	380
	—Coated_2	82	
	—Coated_3	81	
	—Coated_4	74	215

III.8 Fabrication and measurements

III.8.1 Fabrication

The structures were fabricated in 2 parts (body and cover) of aluminum and then silver coated by Thales Alenia Space at Toulouse, France. Once the fabrication was done, a witness sample made of the same aluminum and silver coated at the same time as the body and cover structures and one of the bottom parts were sent to be coated with carbon at Singapore. Due to a fabrication defect on one of the bodies (Figure III.38), it was redone in a new fabrication batch. When drilling the aluminum, the drill started to change its trajectory as shown in the figure. This was caused by the length of the cylinders which was significatively large for the drill needed for the piece, resulting in the combing of the drill.

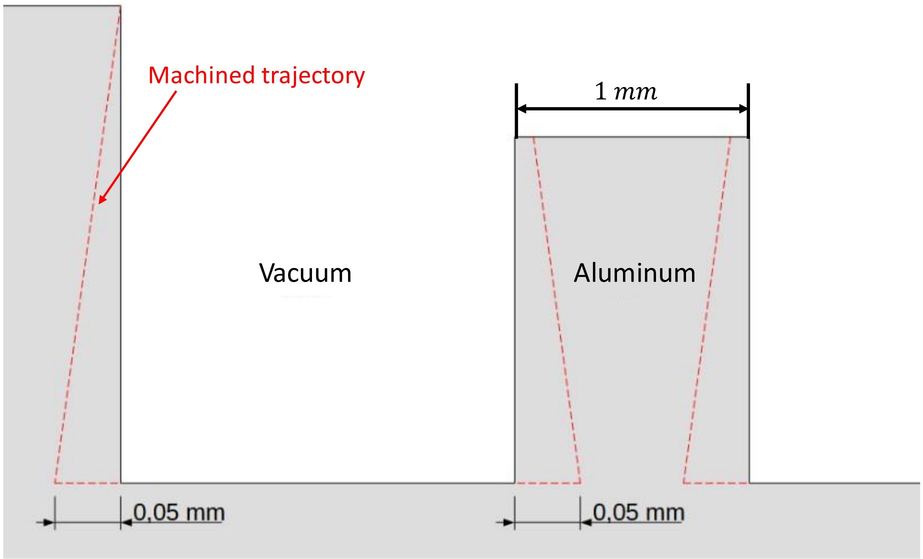

Figure III.38 Description of fabrication defect due to drill combing

Figure III.39 shows all the parts of the two filters and details which was the body part that was fabricated later. Also, the carbon coated bottom part can be observed with a different color than the rest of the pieces.

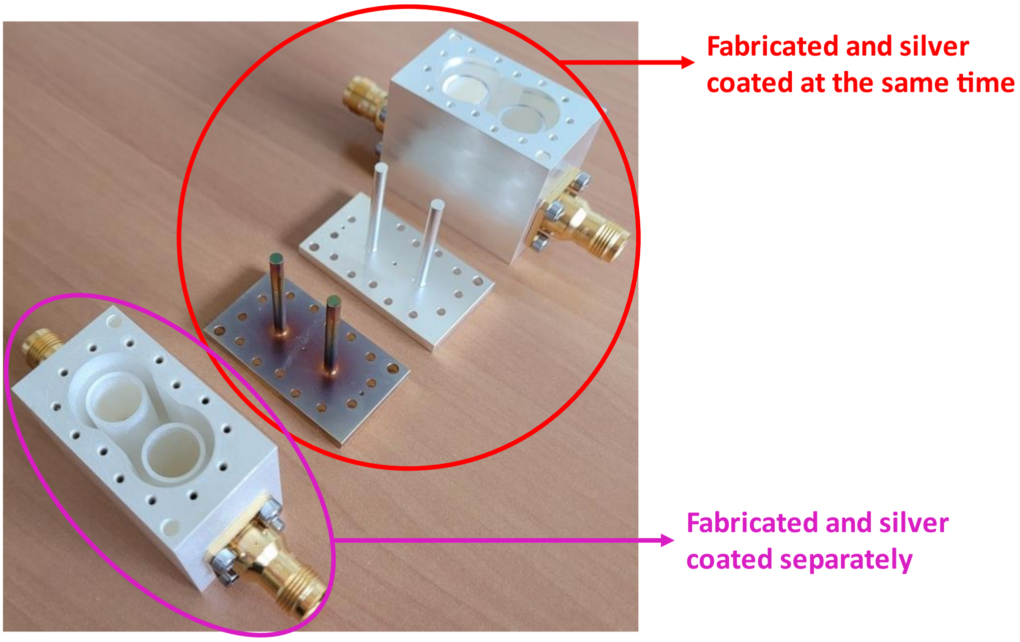

Figure III.39 Description of the fabricated parts of the two filters

A difference between the first and second batch of fabrication is observed. For the first set of fabricated parts (one body and two bottom parts), the silver seemed brilliant. While for the second body, the silver had a matte aspect as presented in Figure III.40. Surface roughness measurements were done on both bodies. For the brilliant body, a roughness average (Ra) equal to 0.4 was measured, while for the matte body, the measured roughness average was of 2.4 which explains the different aspect of this body. In addition, both covers roughness average was of 0.5 in agreement with the brilliant body results since they were all fabricated on the same batch.

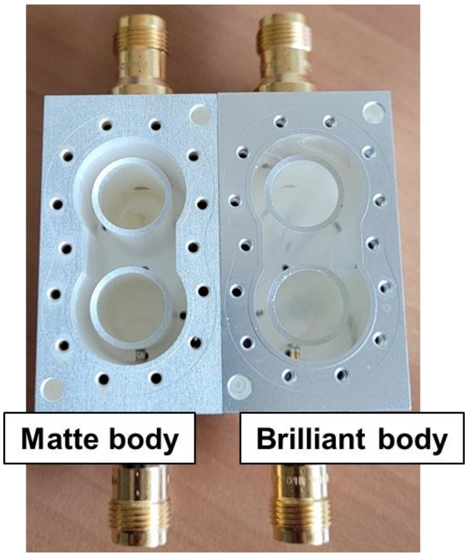

Figure III.40 Comparison of the two bodies aspect

7 tunning screws shown in **Error! Reference source not found.** were added to compensate for fabrication defects. Four of them for tunning the frequency, two on each resonator, one for the iris coupling and two for the input/output couplings, one for each connector. The depth of each screw has an impact of each parameter, and a nominal depth of 4 mm was set. These screws were placed near the short circuit end of the C_2 conductor reducing the impact on the electric field and without disturbing the multipactor response of the structure.

Figure III.41 Detailed view of the tunning screws

III.8.2 Measurements

III.8.2.a RF measurements

Both filters were assembled as shown in Figure III.42 and measured. In both cases, the filters had to be tunned using the tunning screws to obtain a response presented in Figure III.43. A comparison between measurement and simulation showed that the electrical response presented a 1% frequency shift relative to the design, which was determined to be acceptable. This difference came from the same fabrication defect presented in Figure III.38 but in a less significant way.

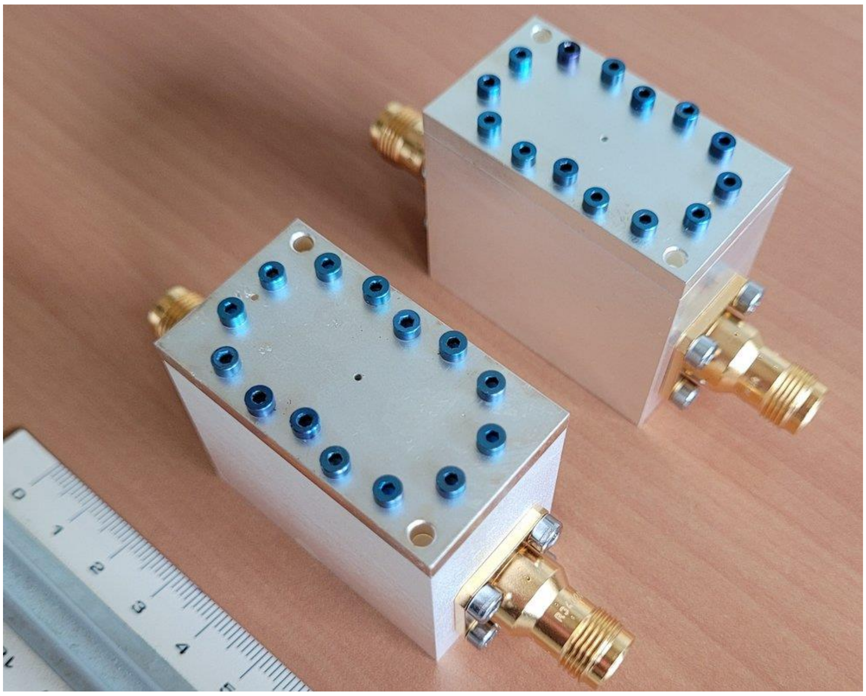

Figure III.42 Both filters assembled.

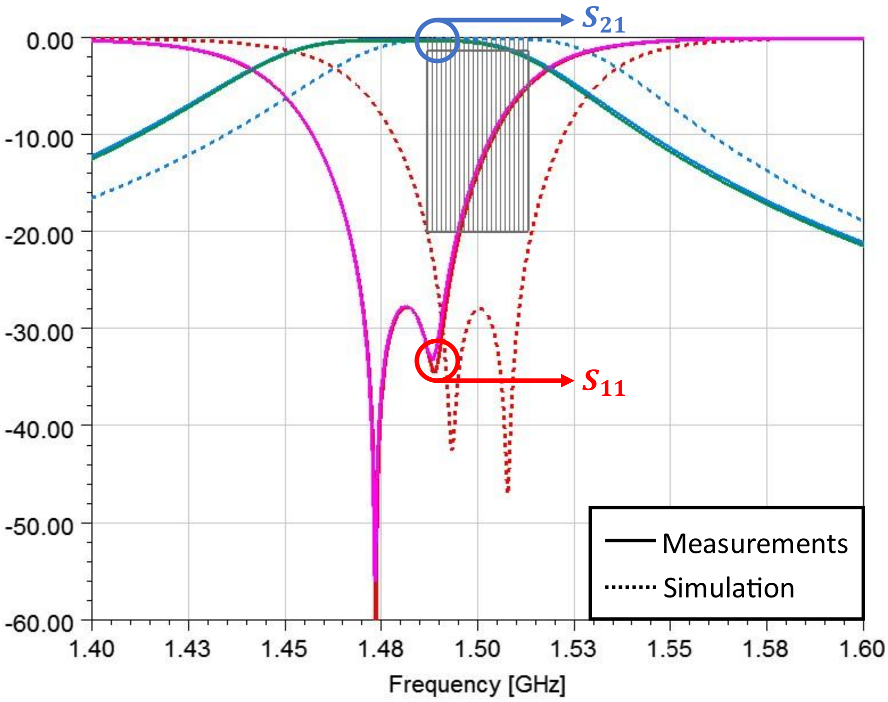

Figure III.43 Measurements and simulation of the electrical responses of the designed filters

III.8.2.b Multipactor measurements

The final structure power simulations done with CST-PIC showed a gain of 3.3 dB for the structure with the carbon coated cover as presented in Table III.13.

Table III.13 Simulated power handling for both structures

Silver cover	Carbon coated cover	Margin
37 W (45.7 dBm)	**80 W** (49 dBm)	**3.3 dB**

At measurement, Combinations between the matte and brilliant bodies were done to identify if there was a difference between both bodies. Results on Table III.14 show that the matte body had a slightly higher power handling than the brilliant body. Nevertheless, in both cases, the difference between the silver and the carbon coated covers was not significant.

Table III.14 Measured power handling for the fabricated structures.

	Silver cover	Carbon coated cover	Margin
Brilliant body	**100 W** (50 dBm)	**89 W** (49.5 dBm)	**-0.5 dB**
Matte body	**126 W** (50.7 dBm)	**126 W** (51 dBm)	**0 dB**

The TEEY measurement of the witness samples that accompanied the coated cover showed significant differences with the simulation curves. First, the maximum number of emitted electrons was higher for both cases (Figure III.44) and there is not a difference for the first crossover energy between the silver and the implemented carbon coatings (Figure III.45).

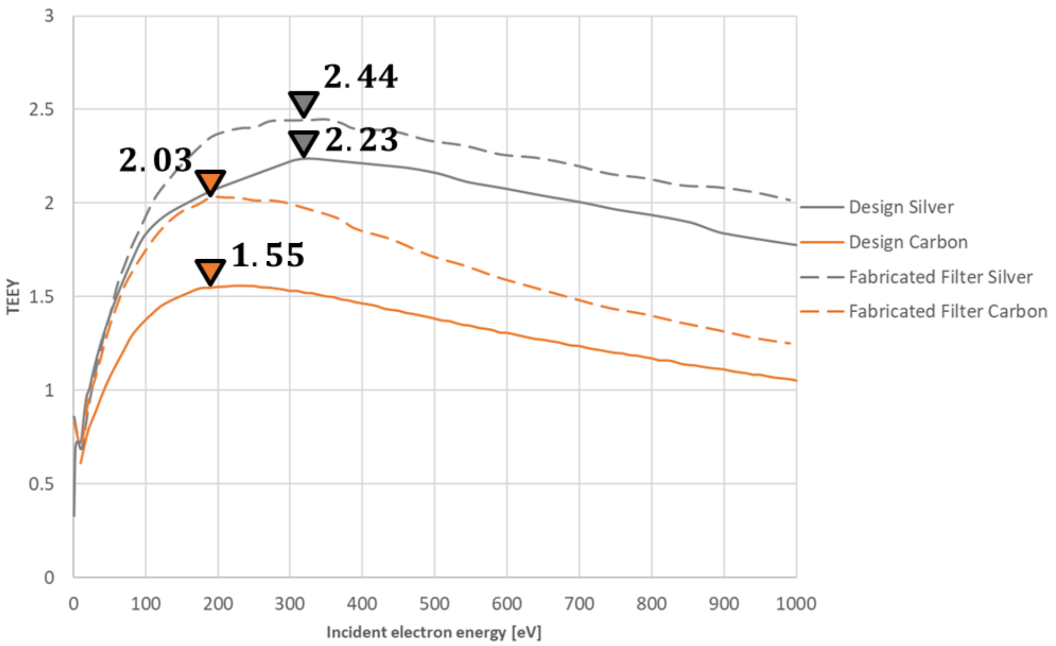

Figure III.44. TEEY curves comparison between the design and fabricated silver and carbon coatings

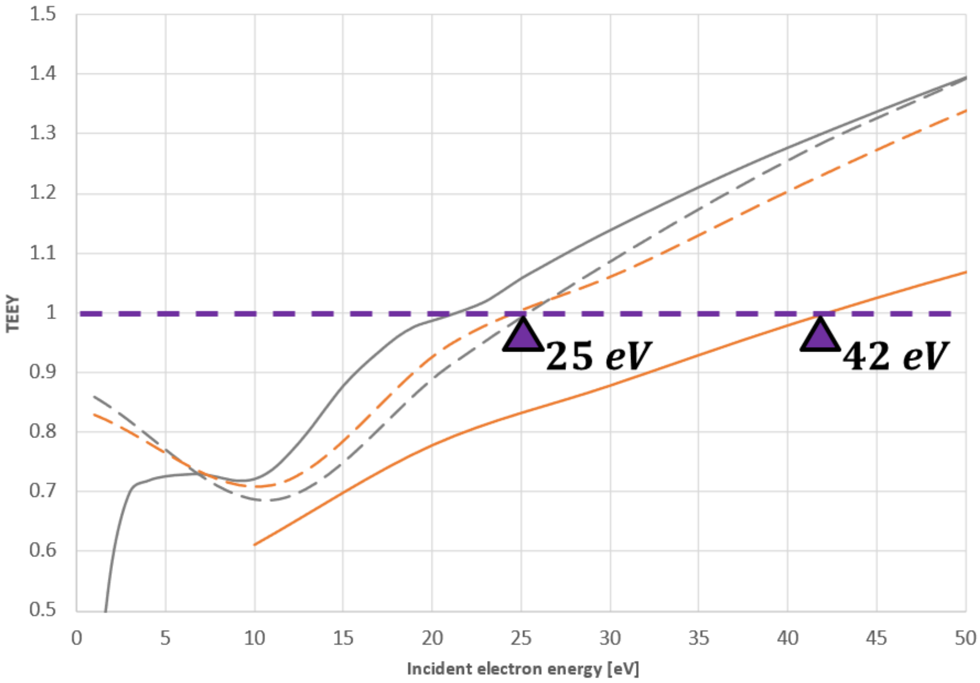

Figure III.45. Detailed vied of the TEEY curves comparison between the design and fabricated silver and carbon coatings

A retro-simulation using this new TEEY curves was done to verify if the initial gain of using carbon was maintained. Result on Table III.15 show that with the secondary emission curves of the fabricated filters a difference of 0.5 dB would be observed.

Table III.15 Comparisson between the initial power simulations and new simulations with the updated TEEY curves

	Silver cover	**Carbon coated cover**	**Margin**
Initial simulation	**37 W** (45.7 dBm)	**80 W** (49 dBm)	**3.3 dB**
Retro simulation	**36 W** (45.56 dBm)	**41 W** (46.12 dBm)	**0.56 dB**

Although the retro simulation showed that no significant difference would be found between the silver and carbon filters, the simulations results do not agree with the power break level of the measurements. The source of this difference must be determined by a detailed study of the structure and an update of the simulation model that considers all the fabrication defects.

III.9 Chapter III conclusion

This work in this chapter led to a better understanding of the power handling in coaxial Stepped Impedance Resonators. The study allowed us to identify the critical dimensions of this type of resonator, an in consequence multiple filtering structures where simulated and analyzed.

Carbon coating integration increases the device power handling for different filter configurations. The simulations showed that the use of localized carbon coatings on the coaxial SIR added a freedom degree for controlling the power handling of a filter.

The multipactor test results did not show a significant difference between the filters. The source of the difference between simulations and measurements must be determined. The identified source for these differences could be:

- Connectors welding, with an unknown secondary emission yield.
- Contamination of the critical areas when welding.
- The uncertainty of the dimensions inside the cylinders due to fabrication defects.
- An abnormal TEEY for the used carbon coatings.

In order to keep a better trace of the samples and their conditions, follow up card describing manipulations and environmental or transport conditions of all the samples must be used.

Finally, to understand the source of the difference for the TEEY curves different analysis will be implemented. The test includes surface roughness of bot silver bodies, and witness samples; visual inspection of the filters after multipactor break test to try to identify the multipactor break area; XPS measurements of the samples and try on the covers and finally an SEM study as the one done by CNES before multipactor test.

Chapter IV : Two-section coaxial SIR with parallel central sections

IV.1 Introduction

In this chapter, a new topology using inner parallel sections in a coaxial SIR is presented. To do so, first the traditional coaxial SIR and its current limitations are explained and discussed. Second, the novel resonator topology is described with its correspondent electrical model and compared with the traditional topology. Third, an analytical model for the quality factor considering the use of parallel central sections is presented and validated by eigenmode simulations, allowing to compare this new resonator with a traditional topology.

Then, the design of a 4th order filter with parallel central sections is presented. The fabricated structure measurements are contrasted with simulation results to validate this novel topology. Finally, multipactor simulations were performed to determine the power handling capabilities of the topology.

IV.2 Need to increase distance between conductors

A critical dimension in the design of the resonators is the distance between metallic walls inside the filter. Critical environments are mainly defined by the relationship $f \times d$, between frequency f and distance d as mentioned in Section I.4.1.c as this relationship increases, the power handlingof the structure can increases . The physical dimensions of the structure are linked to the electrical properties such as: quality factor, characteristic impedance of each individual section, and the impedance ratio M (IV-1).

$$M = \frac{Z_1}{Z_2} \tag{IV-1}$$

IV.3 Coaxial Stepped Impedance Resonator with parallel inner sections

IV.3.1 Coaxial Stepped Impedance Resonator

As presented in Figure IV.1, a coaxial structure has two critical dimensions, the inner conductor diameter "a" and the outter conductor diameter "b". The charecteristic impedance of a coaxial line is a function of these dimensions and of the dielectric permitivity of the filling insulator between these conductors with a relative permitivity ε_r as equation (IV-2) presents.

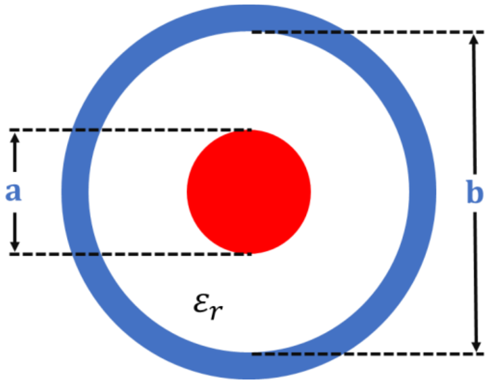

Figure IV.1 Coaxial dimensions

$$Z_i = \frac{\eta_o}{2\pi\sqrt{\varepsilon_r}} \ln\left(\frac{b}{a}\right) \qquad \text{(IV-2)}$$

In the case of space applications considering the multipactor effect, it is convenient to study the structures in terms of the distance between conductors as this is the distance where multipactor will occur. For a coaxial line, this distance is equal to b-a and the evolution of the impedance in terms of the distance between these conductors is presented in Figure IV.2.

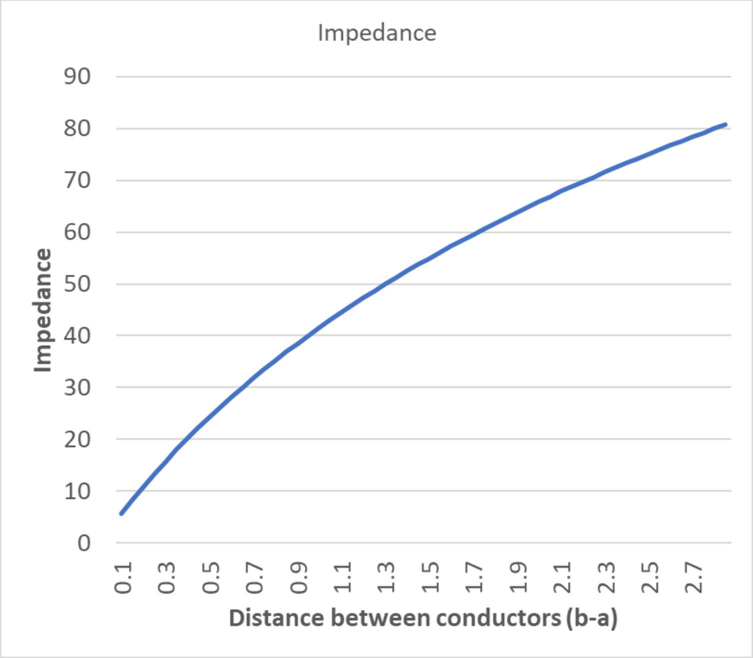

Figure IV.2 Impedance Vs distance between conductors in a coaxial line

The impedance ratio M of a coaxial Stepped Impedance Resonator is defined by the desired electrical perfomances of the filter. As M increases, the length of the resonator is reduced , and the first harmonic is rejected far from the fundamental [24]. Since the electrical length θ_0 of the resonator if a function of M a relationship between M and the first harmonic apparition can be obtained using equations (IV-3) and (IV-4) .

$$\theta_0 = \operatorname{atan}\left(\frac{1}{\sqrt{M}}\right) \tag{IV-3}$$

$$f_1 = \left(\frac{\pi}{\theta_0} - 1\right) f_o \tag{IV-4}$$

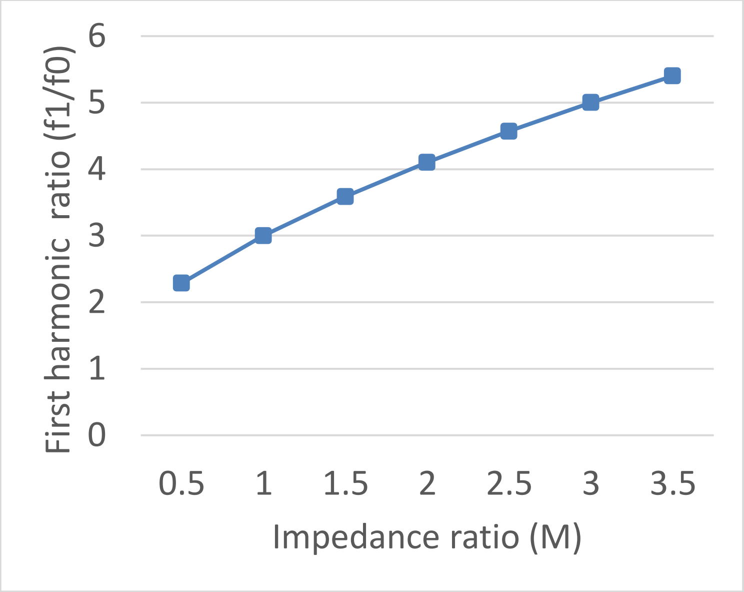

Figure IV.3 First harmonic Vs impedance ratio in a coaxial SIR

Figure IV.3 presents how the frequency of the first harmonic increases with the impedance ratio M. The impedance ratio M also has an impact on the length l of each section, since the length of the resonator in air (IV-5) is also defined by (IV-3).

$$l = \frac{c}{2\pi f_0}\theta_0 \qquad \text{(IV-5)}$$

IV.4 Parallel sections approach

For a defined structure, if a large M is desired, there are two choices. First, one can increase the outer characteristic impedance Z_1 leading to a bigger structure. However, this is not desired since the footprint of the filter is usually constrained by the available space in the system. Secondly, one can chose a smaller value for the inner characteristic impedance Z_2. This translates to a smaller distance between conductors “a” and “b” of the central section. However, a smaller gap leads to a lower $f \times d$, lower power handlings of the structure and decrease the sensibility to fabrication defects.

To solve this, a parallel impedance model is proposed by replacing the inner line of characteristic impedance Z_2 with an equivalent line made of several parallel lines of characteristic impedance Z'_2. For example, if we consider two parallel lines with a characteristic impedance Z'_2:

$$\frac{1}{Z_2} = \frac{1}{Z'_2} + \frac{1}{Z'_2} \tag{IV-6}$$

Therefore, using parallel impedances to obtain an equivalent inner impedance Z_2 using greater values of Z'_2 will lead to an increase of the distance between conductors by keeping the same structure volume. For example, an inner section with $Z_2 = 20\ \Omega$ has a gap of 0.4 mm and, a section with $Z'_2 = 40\ \Omega$, has a gap is of 0.9 mm. Hence, with two inner sections in parallel of $Z'_2 = 40\ \Omega$ each, the electrical characteristics will be kept and distances between conductors will increase.

IV.4.1 Modeling

Starting with the classical two-section coaxial Stepped Impedance Resonator, the circuit model is presented on the right of Figure IV.4 and its corresponding cross section view implementation on the left. Also, the circuit model representation on ADS is given in Figure IV.5.

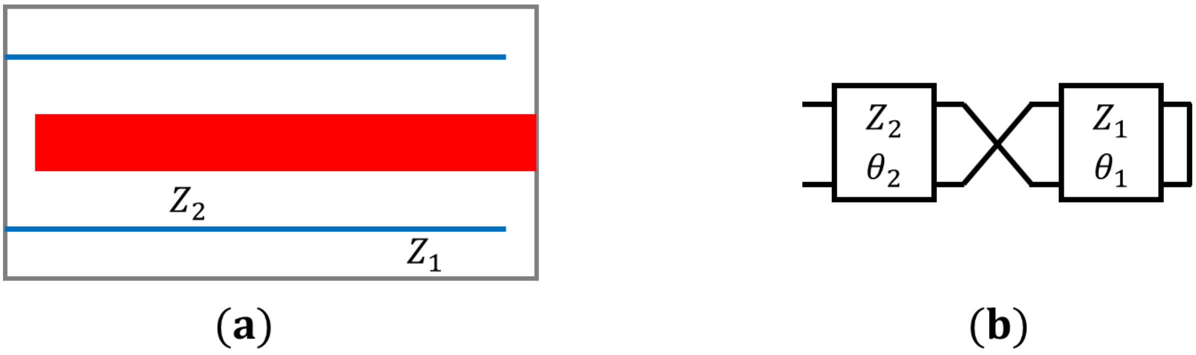

Figure IV.4 Two sections coaxial Stepped Impedance Resonator model. (a) cut view. (b) electrical model

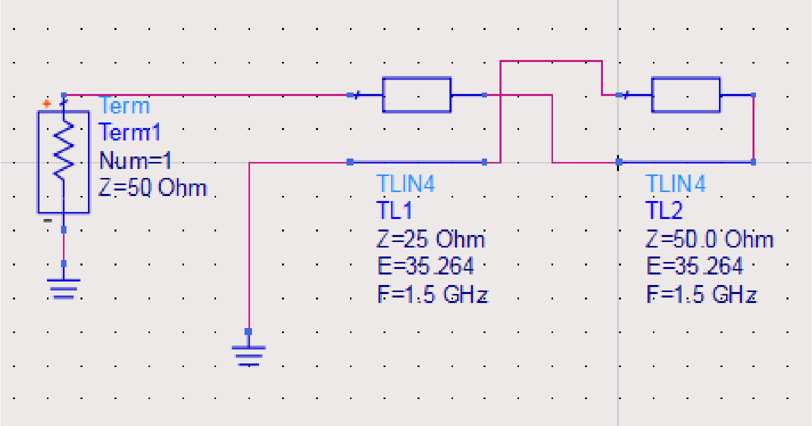

Figure IV.5 ADS model of a two-sections coaxial Stepped Impedance Resonator

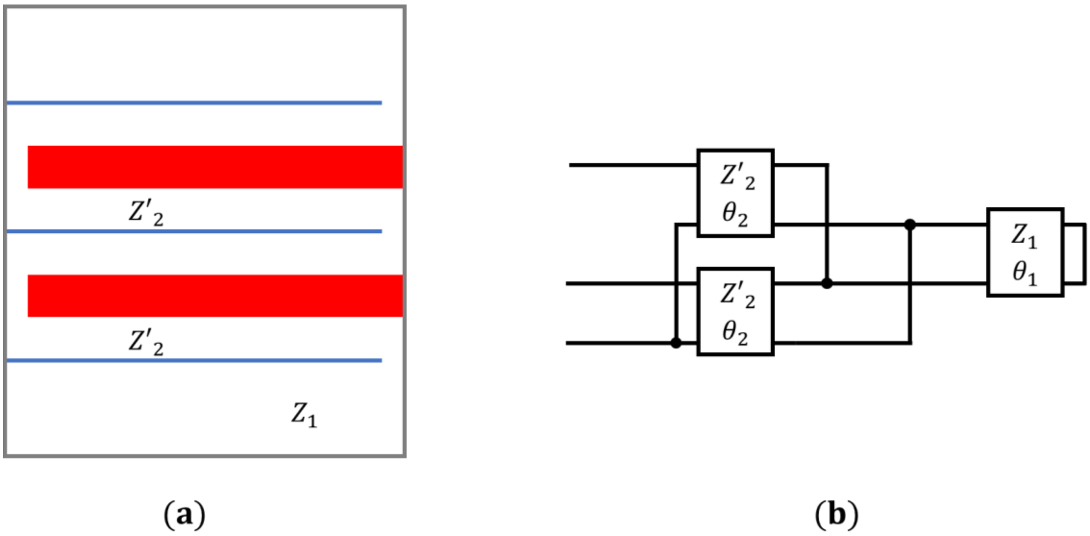

Figure IV.6 Two-sections coaxial Stepped Impedance Resonator with two inner sections in parallel (a) cut view (b) electrical model

Figure IV.6 presents a two-sections coaxial Stepped Impedance Resonator with Two inner sections in parallel, first on a circuit model, second on a lateral cut of the structure. Here it is important to note that both inner sections are in parallel and are connected to the same reference by the blue conductor. The electrical model simulation in ADS is presented in Figure IV.7.

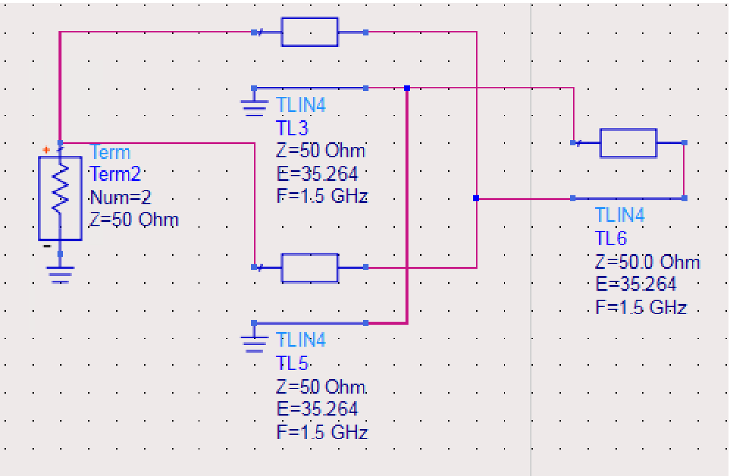

Figure IV.7 ADS model of a two-sections Coaxial Stepped Impedance Resonator with two inner sections in parallel.

When comparing the input impedance of both models, with one and two inner sections, it can be constated that they are equivalent in the vicinity of the resonance frequency as it's presented in Figure IV.8. Then, this comparison was also made on a broadband circuit analysis as presented by Figure IV.9 also showing the same behavior for the input impedances all over the band from 1 to 10 GHz.

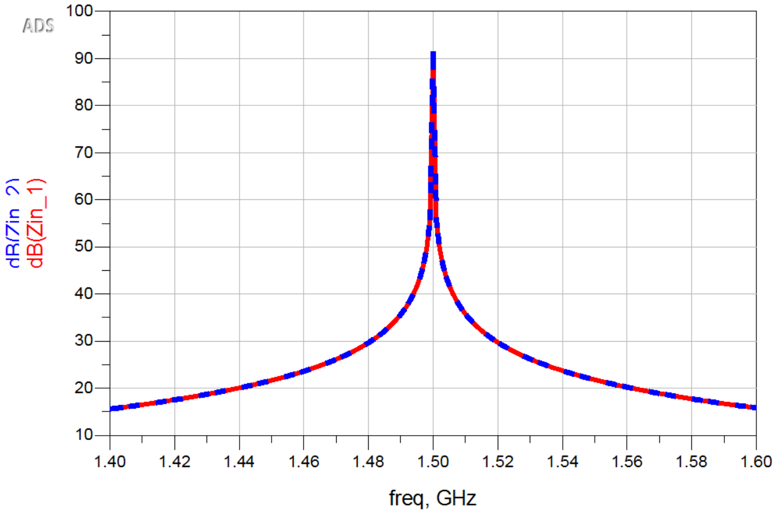

Figure IV.8 Input impedance in the vicinity of the fundamental resonance frequency

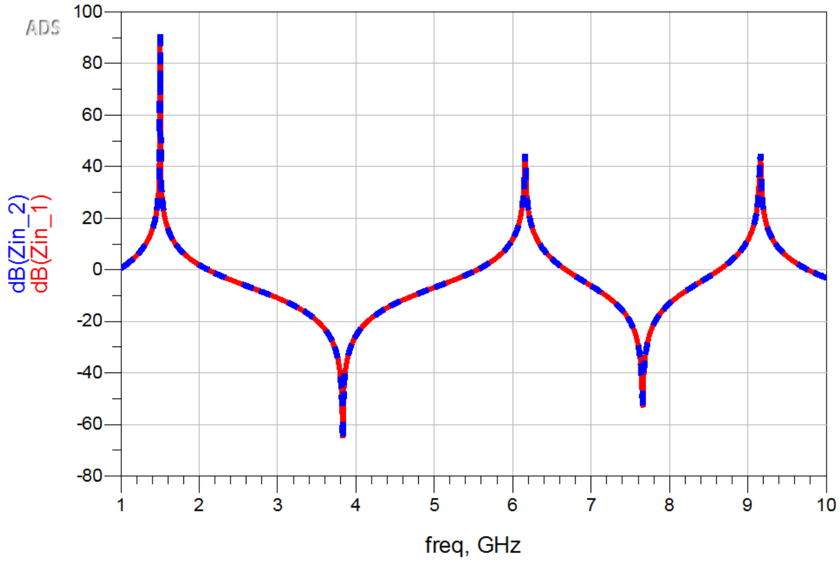

Figure IV.9 Input impedance in wideband

Finally, a 2nd order filter prototype was designed with both resonator topologies, the traditional coaxial Stepped Impedance Resonator and the one with two parallel inner sections. Figure IV.10 shows the proposed circuit model simulated on ADS for the traditional topology, and Figure IV.11 shows the circuit model for the two parallel inner sections.

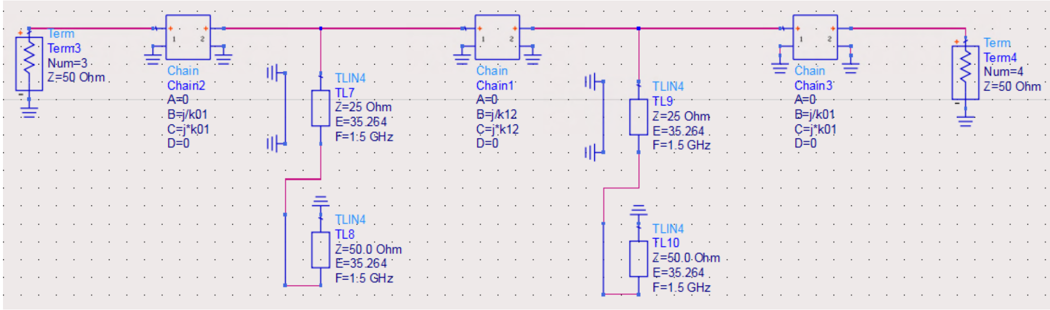

Figure IV.10 2nd order filter with traditional resonator

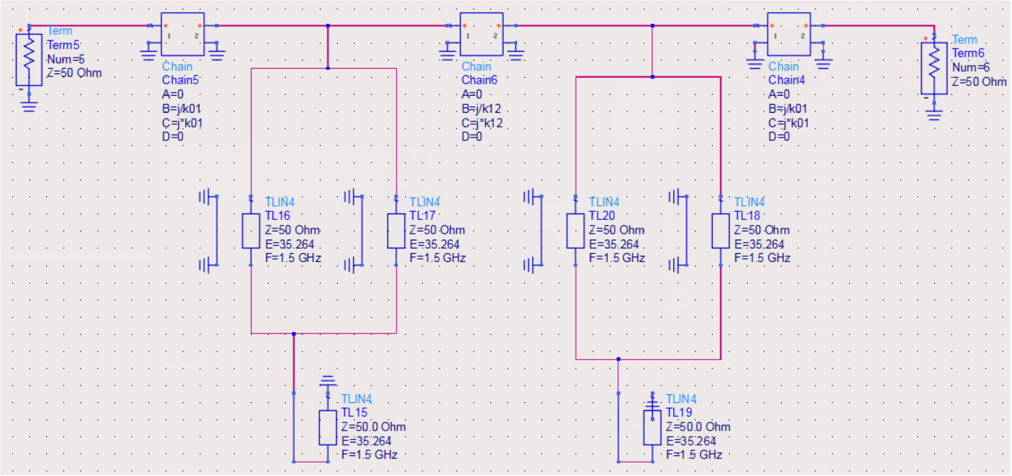

Figure IV.11 2^{nd} order filter with two inner parallel sections resonator

Finally, both responses are compared in Figure IV.12. The red and blue lines are the S11 and S21 parameters respectively of the traditional resonator topology implementation. The dashed black lines correspond to the S11 and S21 of the novel resonator topology implementation. Each dashed line is equivalent to the response they are over.

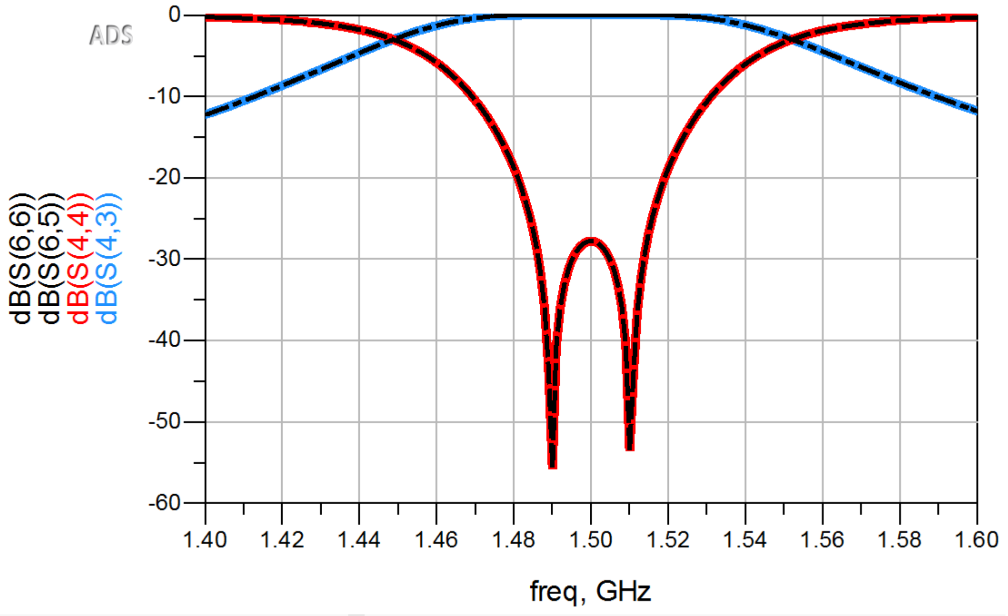

Figure IV.12 Frequency response comparison for both models

IV.5 Physical implementation

In order to maintain coherence between variables, and avoid misunderstandings in the specifications of the filter, a new variable “k” is added to the synthesis. This new variable represents the number of inner sections in parallel in a coaxial Stepped Impedance Resonator.

The first step to implement the novel topology, was to determine how with multiple inner sections in parallel, the outer section could still be kept as a coaxial section. To do so, the medium conductor of the resonator is proposed to be an entire block. In this way, multiple equal coaxial sections can be included inside without changing the geometry of the outer section. An example of this implementation is presented in Figure IV.13 for the cases k=1 as the traditional topology, k=2 and k=3 for the novel topology implementation.

Variables A_1 and A_2 correspond to the distance between conductors of different sections. A_1 for the outer section, correspondent to Z_1 and A_2 for the individual inner sections in parallel. As a reminder the impedance ratio calculation is now done with the equivalent impedance Z'_2.

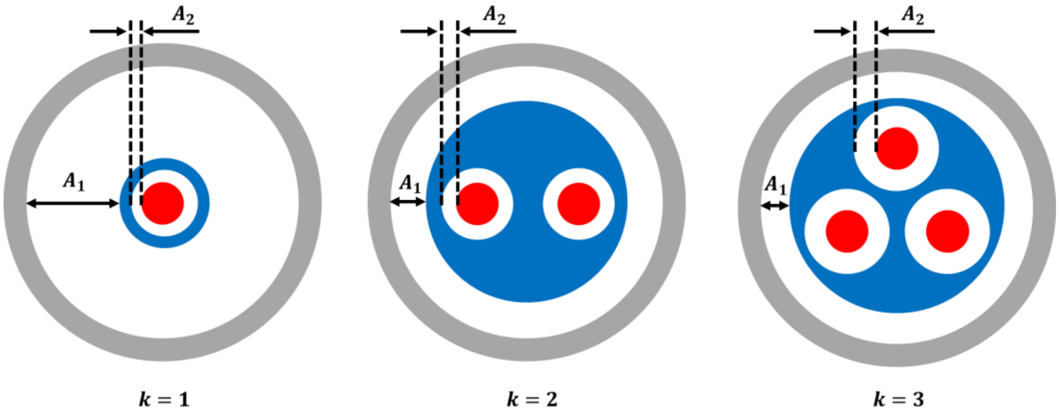

Figure IV.13 implementation representation

IV.6 Design

As shown previously, as the number of sections in parallel is increased, the air gap between conductors A_2 increases. For a resonator that keeps the same footprint, the external dimension cannot be modified. This leads to a reduction of de distance A_1 as k increases, and a change of the characteristic impedance Z_1. Since this leads to a complex modification of distances, and impedances for each step, formulas that allows the design of the structure using the initial design restrictions as parameters are proposed in (IV-7)-(IV-9).

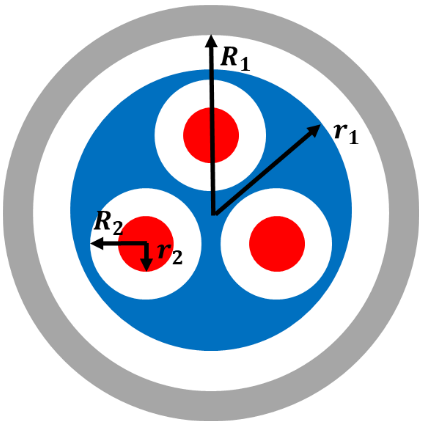

Figure IV.14 Coaxial Stepped Impedance Resonator with k=3

R_1 → Radius of the external conductor of the outer section

r_1 → Radius of the internal conductor of the outer section

R_2 → Radius of the external conductor of the inner section

r_2 → Radius of the internal conductor of the inner section

$$M = \frac{Z_1}{Z_2} = \frac{Z_1}{Z_2'/_k} = \frac{k.Z_1}{Z_2'} \qquad \text{(IV-7)}$$

$$M = \frac{k\, ln\left(\frac{R_1}{r_1}\right)}{ln\left(\frac{R_2}{r_2}\right)} \qquad \text{(IV-8)}$$

$$r_1 = R_1\left(\frac{r_2}{R_2}\right)^{\frac{M}{k}} \qquad \text{(IV-9)}$$

IV.7 Quality factor study

IV.7.1 Modeling

It is important to determine the impact of the parallel sections over the overall quality factor of the resonator. To do so, the expression presented [30] is used. Here, the expression of the quality factor of a two-section coaxial Stepped Impedance Resonator is presented.

$$Q = \frac{2\omega_0\sqrt{\mu_0\varepsilon_0}}{\frac{4R_s\sqrt{\frac{\varepsilon_0}{\mu_0}}}{l} + \frac{Res_1}{Z_1} + \frac{Res_2}{kZ_2} + \sqrt{M}\left[\frac{\frac{Res_1}{Z_1} - \frac{Res_2}{kZ_2}}{\beta l(M+1)}\right]} \qquad \text{(IV-10)}$$

Res_1 and Res_2 are the corresponding resistances per unit length length (Ω.m^{-1}) of the two sections from the circuit model of a coaxial line expressed by (IV-12), and R_s is the surface resistance expressed by (IV-11) in terms of the permeability μ_0, the resonant frequency ω_0 and the electrical conductivity of the material σ.

$$R_s = \sqrt{\frac{\omega_0\mu_0}{2\sigma}} \qquad \text{(IV-11)}$$

$$Res_i = \frac{R_s}{2\pi}\left(\frac{1}{R_i} + \frac{1}{r_i}\right) \qquad \text{(IV-12)}$$

The length of the resonator is expressed in terms of the impedance ratio M and the fundamental pulsation ω_0 when the dielectric is vacuum or air (IV-13):

$$l = \frac{c}{\omega_0} atan\left(\frac{1}{\sqrt{M}}\right) \qquad \text{(IV-13)}$$

It is important to consider the physical limitations of the structure since an infinity of solutions are possible to obtain the different characteristic impedances. As Z_1 and Z_2 are calculated separately, a possible solution wrong could be an inner section bigger than the outer section. To prevent this from happening, boundary conditions based on each geometry case were set for the cases from k=1 up to 5. For the maximum radius of r_1, it must be smaller than R_1, and for its minimum value $r_{1\,min}$, the restrictions are defined as follows:

For all the different configurations, it is important to take into account the thickness of the metallic wall $Wall_{th}$ (generally constrained by the fabrication technology). Doing this, results in a more accurate design and model.

k	$Design$	$r_{1\,min}$	
1	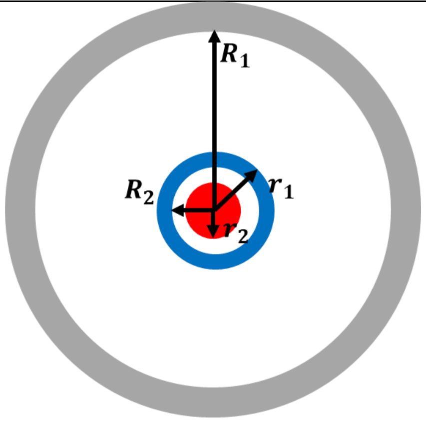 *Figure IV.15 Coaxial Stepped Impedance Resonator with k=1*	$R_2 + Wall_{th}$	(IV-14)
2	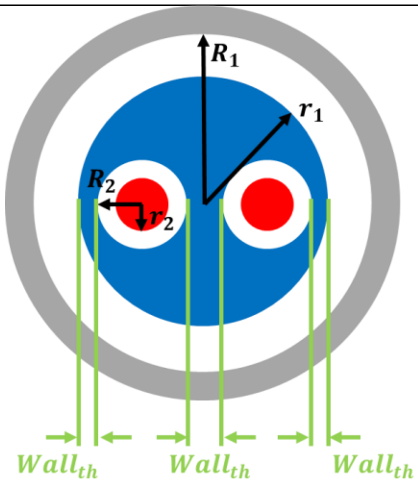 *Figure IV.16 Coaxial Stepped Impedance Resonator with k=2*	$\frac{4R_2 + 3Wall_{th}}{2}$	(IV-15)

k	*Design*	$r_{1\,min}$	
3	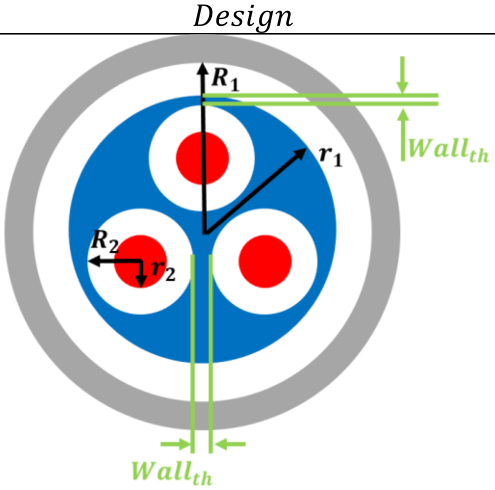 *Figure IV.17 Coaxial Stepped Impedance Resonator with k=3*	$\frac{2R_2+Wall_{th}}{\sqrt{3}}+R_2+Wall_{th}$	(IV-16)
4	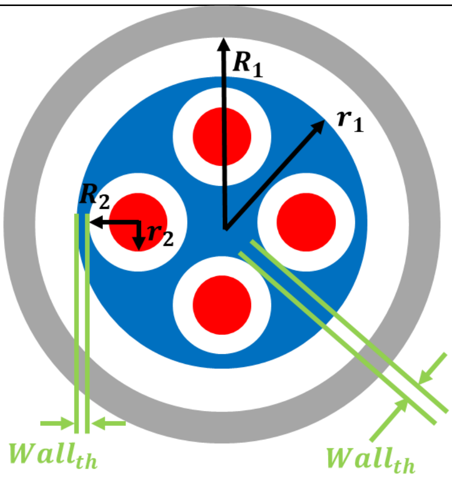 *Figure IV.18 Coaxial Stepped Impedance Resonator with k=4*	$\frac{2R_2+Wall_{th}}{\sqrt{2}}+R_2+Wall_{th}$	(IV-17)
5	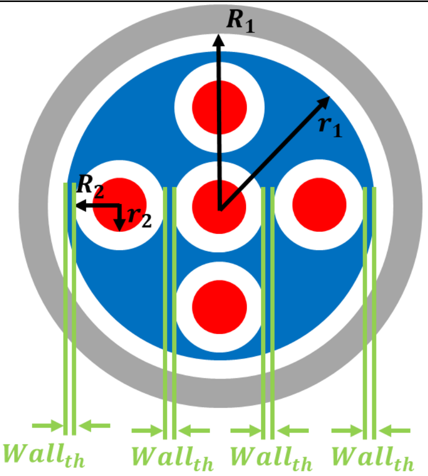 *Figure IV.19 Coaxial Stepped Impedance Resonator with k=5*	$3R_2+2Wall_{th}$	(IV-18)

IV.8 Results

First, a MATLAB routine was implemented to analyze the Quality factor of the novel topology using (IV-10). The study considered all the possible configurations for a resonator within the following conditions:

Table IV.1 Coaxial SIR characteristics for the studied resonators.

Variable	**Value**
M	2
R_1	25 mm
r_2	1 mm
$wall_{th}$	1 mm
k	1-5

The minimum vacuum gap between conductors was set at 0.5mm. With this restrictions, R_2 possible values were calculated with (IV-14) - (IV-18). The results of all the possible configurations are presented in Figure IV.20.

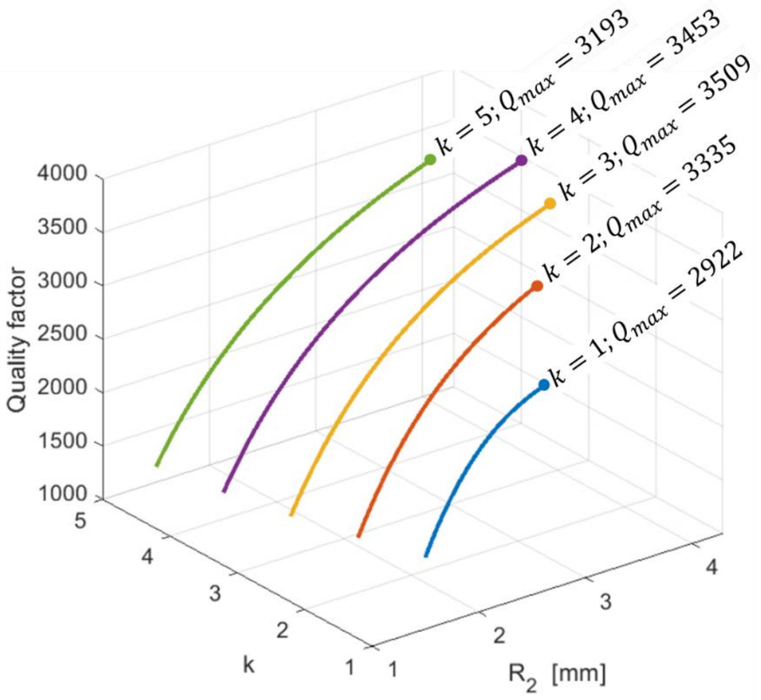

Figure IV.20 Quality factor analytical results

By observing the results presented in Figure IV.20, the following tendencies appears clearly. First, the highest Quality factor for every k configuration is when the distance between conductors of the inner section is greater. Also, the use of multiple sections in parallel allows higher quality factor for the same volume. However, this tendency is limited to a certain number of sections in parallel, as k increases, a decrease of the maximum quality factor can be observed (k=4 and k=5).

To validate these results, Eigenmode simulations were done using ANSYS HFSS. The maximum values for every configuration were chosen in order to validate that the implementation of multiple sections in parallel allowed an increase of the global Quality factor of the structure. Obtained values are presented and compared in Table IV.2.

Table IV.2 Maximum Quality factor results comparison

k	**Analytical model**	**Eigenmode Simulation**	**Relative error**
1	2922	3624	19.4 %
2	3335	4034	17.3 %
3	3509	4050	13.4 %
4	3453	3857	10.5 %
5	3193	3507	8.9 %

These results were plotted and compared in Figure IV.21, it can be seen that both estimations of the resonators quality factors follow the same behavior. The quality factor increases until a maximum estimation is obtained for k=3 and after this, the quality factor drops rapidly as the number of sections in parallel continue to increase.

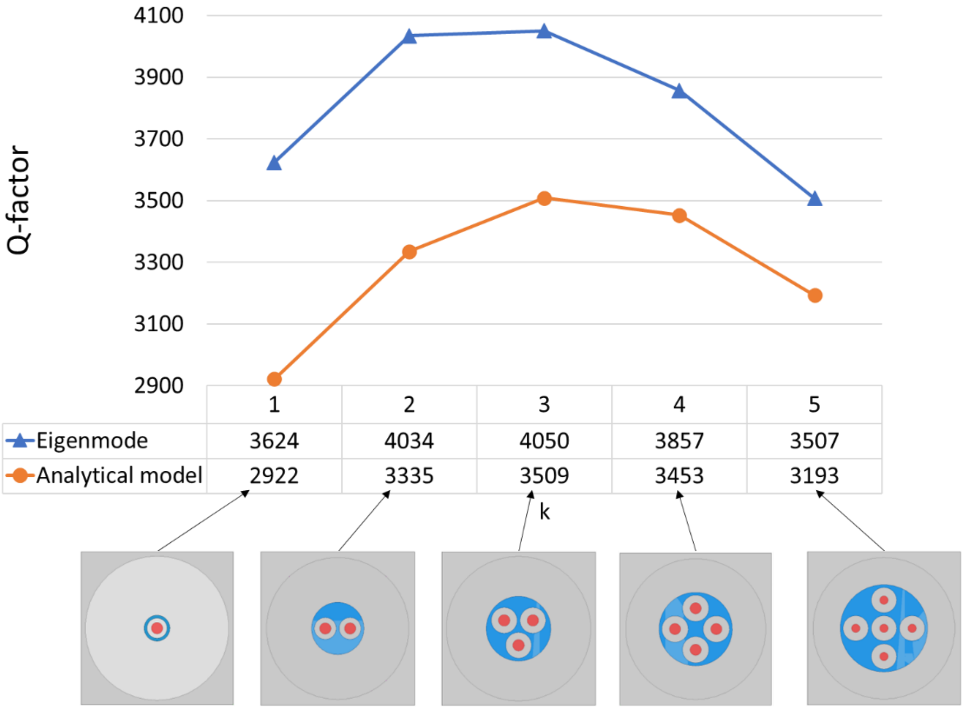

	1	2	3	4	5
▲ Eigenmode	3624	4034	4050	3857	3507
● Analytical model	2922	3335	3509	3453	3193

Figure IV.21 Q-factor comparison between eigenmode simulations and the analytical model

With the purpose of better comparing the Quality factor of the different configurations and different M ratios, the same analysis was made changing M at each run. The results of these calculations using the analytical model are presented from Figure IV.22 to Figure IV.25 showing the evolution of the Quality factor for different sections in parallel (k) at their corresponding M.

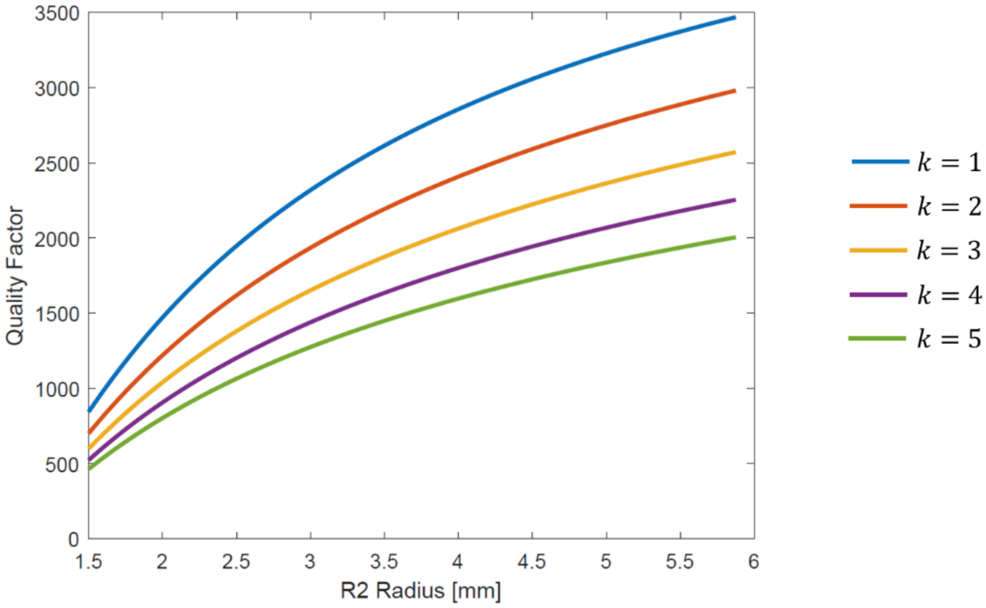

Figure IV.22 Quality factor vs Radius R_2 for M=0.5

As it can be observed in Figure IV.22, the best configuration, in terms of Quality factor, with an impedance ratio of 0.5 is the traditional topology (k=1). The use of two sections in parallel reduces de Quality factor by approximately 500 at its maximum and does not allow greater distance values for the inner sections.

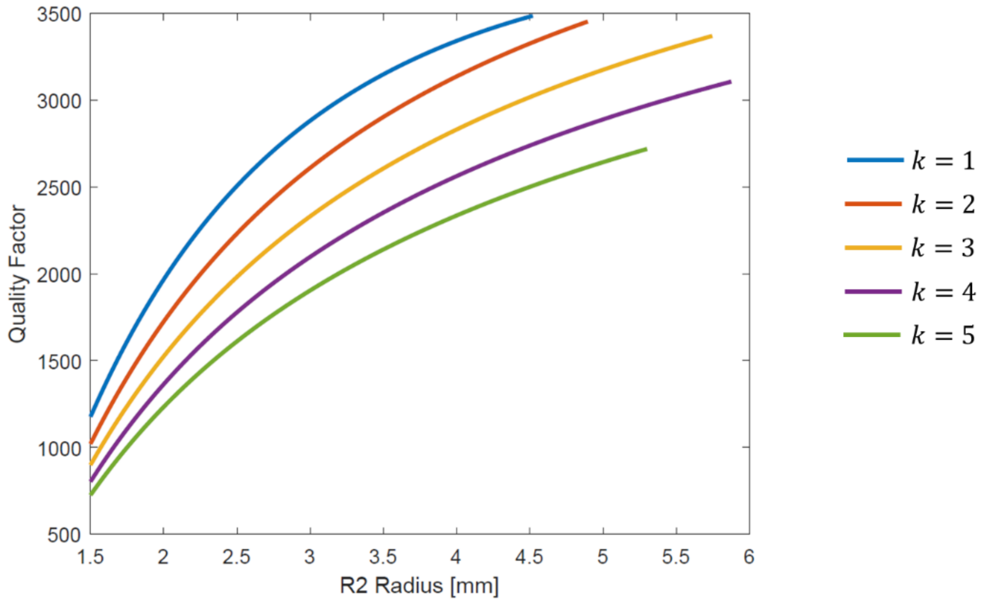

Figure IV.23 Quality factor vs Radius R_2 for M=1

From Figure IV.23, it can be observed that the k=1 topology had a maximal dimension of the radius R_2 is of 4.5 mm, while the k=3 case allows R_2 increases up to 5.7 mm without a significant decrease of the total Quality factor (around 200).

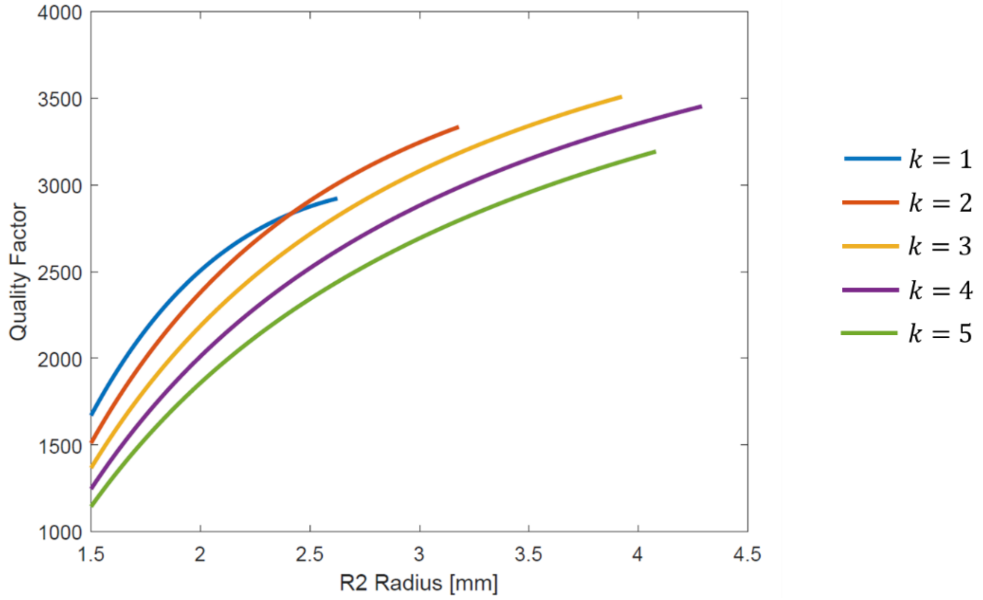

Figure IV.24 Quality factor vs Radius R_2 for M=2

In Figure IV.24 the previously described effect is more evident. The use of parallel sections will increase the quality factor and will allow larger distances between the conductors.

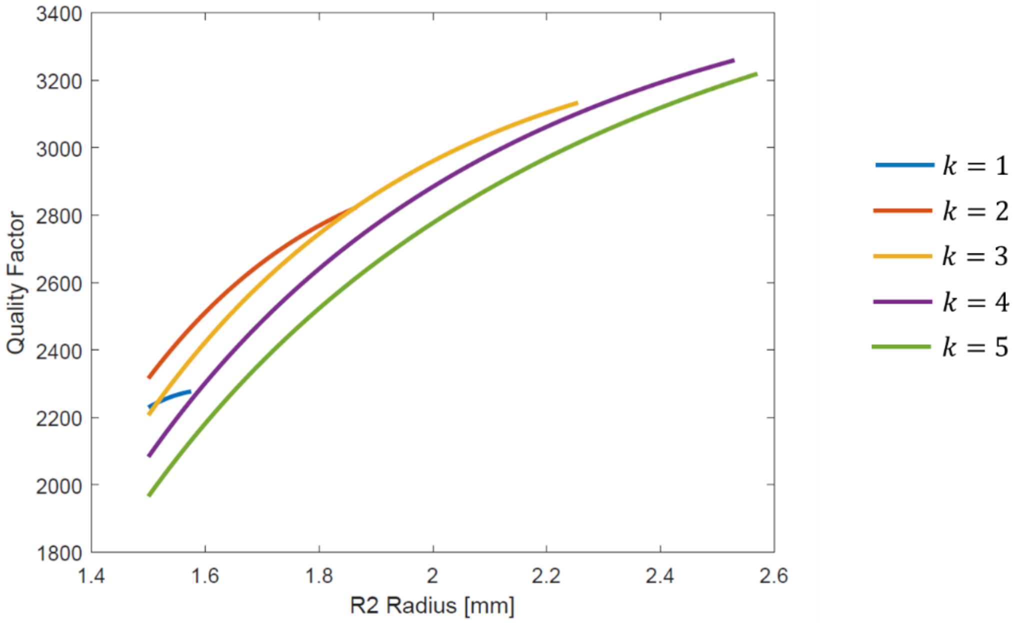

Figure IV.25 Quality factor vs Radius R_2 for M=5

Finally, the benefit of using multiple sections is clearer as M is bigger. As presented by Figure IV.25, the traditional topology does not give the best quality factor in any case. Additionally, the traditional configuration is extremely limited in the possible configurations with distances between 1.5 mm and 1.6 mm, while the use of up to 5 sections in parallel leads, to quality factors above 3000 and distances up to 2.5 mm, resulting in a better power handling compared to the k=1 case.

The use of inner parallel sections is interesting as M increases, allowing better Quality factors than the traditional topology and even allowing the implementation of impedance ratios that were not possible with the traditional topology.

IV.9 Electromagnetic modeling and simulation

An electromagnetic simulation of a 4^{th} order filter is performed to validate the novel resonator topology for use in RF filters. The simulated structure is also compared with an equivalent version of the traditional topology.

IV.9.1 Filter Specifications

An L-band filter centered at 1.5 GHz with a 25 MHz bandwidth was specified. With insertion losses lower than a -0.5 dB at the central frequency, and a matching level under -20 dB, a 4th order filter was designed with specifications presented in Table IV.3

Table IV.3 L-band filter specifications

Parameter	**Value**
Central frequency	1.5 GHz
Fractional Bandwidth	1.67 %
Insertion losses	-0.5 dB
Reflection losses	-20 dB

IV.9.2 4th order filter

Using the results previously obtained for M=2, the optimal configuration in terms of quality factor is with k=3, with a Quality factor of 3508 versus 2918 for the traditional topology. Both configurations were simulated to be compared. Figure IV.26 presents the simulated structure for the classical resonator topology (k=1) that will be used as reference, while in Figure IV.27 the filter with 3 inner sections in parallel is presented. The main characteristics of the designed filters are also presented on Table IV. 2.

Table IV.4 Characteristics of the designed filters

k	$R_1[mm]$	$r_1\ [mm]$	$R_2\ [mm]$	$r_2\ [mm]$	$l_\varepsilon[mm]$	$Z_1\ [\Omega]$	$Z_2\ [\Omega]$	M
1	25	3.62	2.62	1	4	115.8	57.75	2
3	25	10.02	3.92	1	4	54.8	81.9/3	2

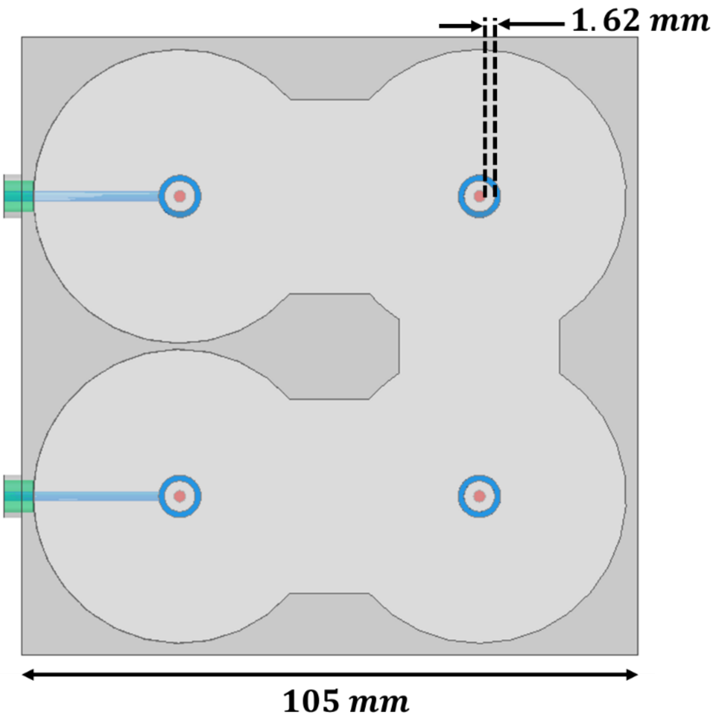

Figure IV.26 4th order filter with k=1

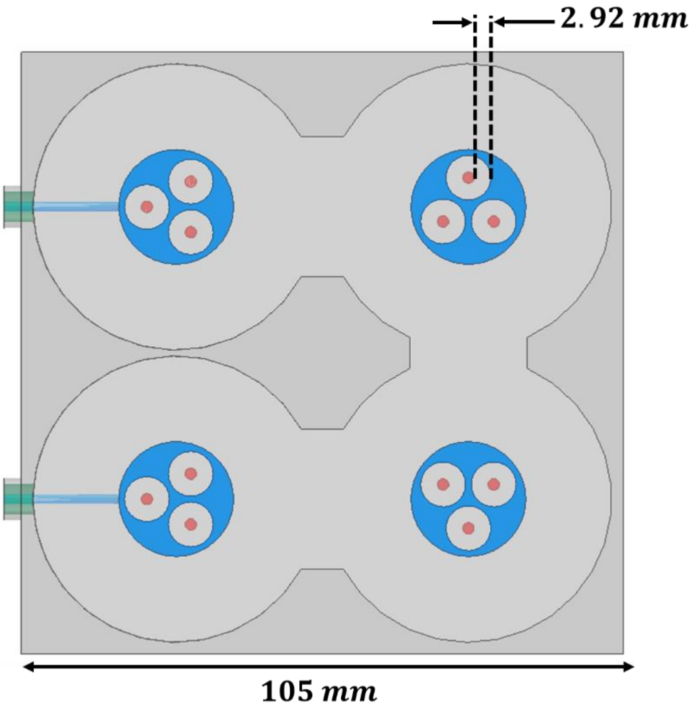

Figure IV.27 4th order filter with k=3

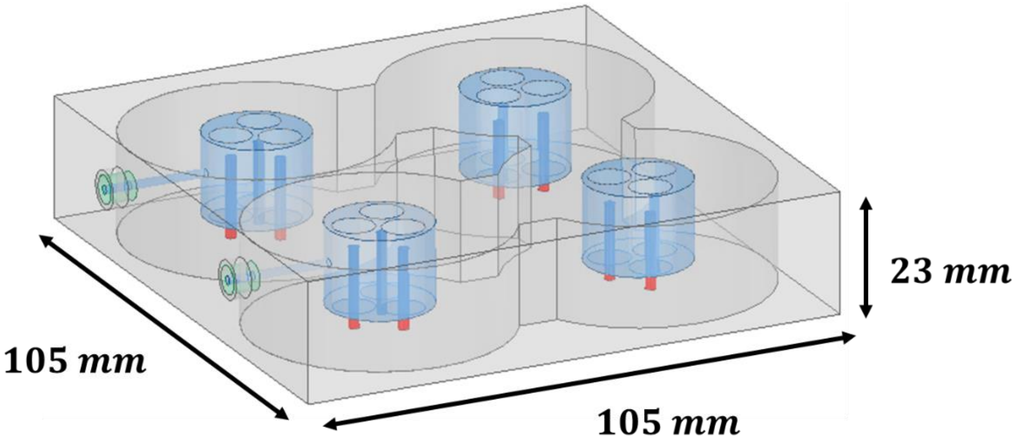

Figure IV.28 Global dimensions of the designed filter

Electromagnetic simulations were done using ANSYS HFSS, and the frequency responses of the filters are presented in Figure IV.29 for the traditional topology, and Figure IV.30 for the novel topology. A comparison between the two filters' responses is also presented in Figure IV.31.

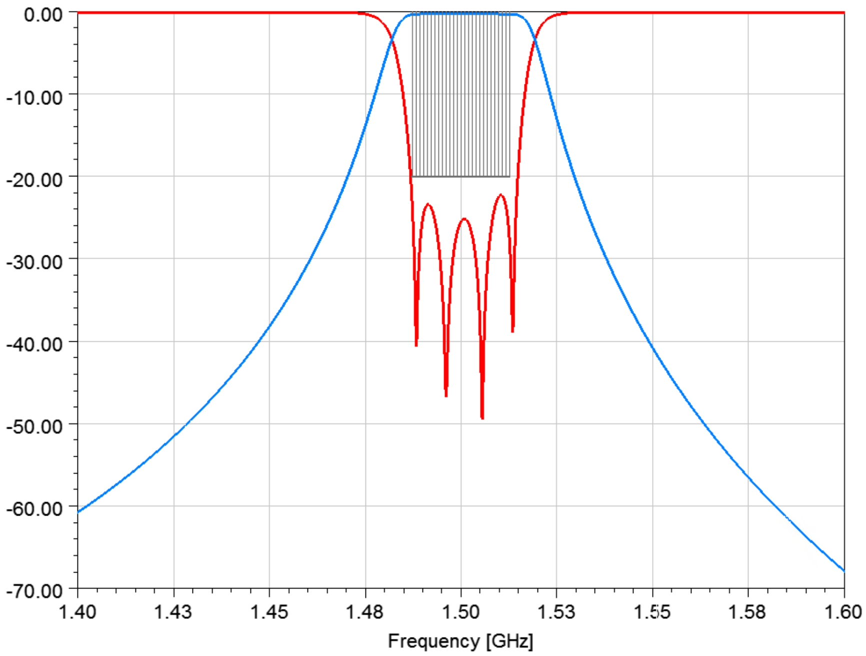

Figure IV.29 4^{th} order filter k=1 simulation response

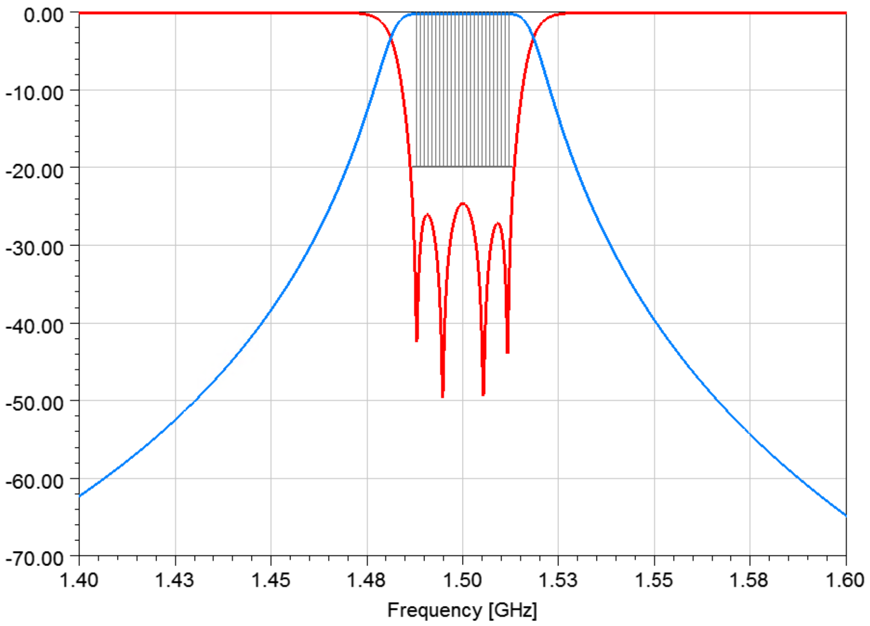

Figure IV.30 4th order filter k=3 simulation response

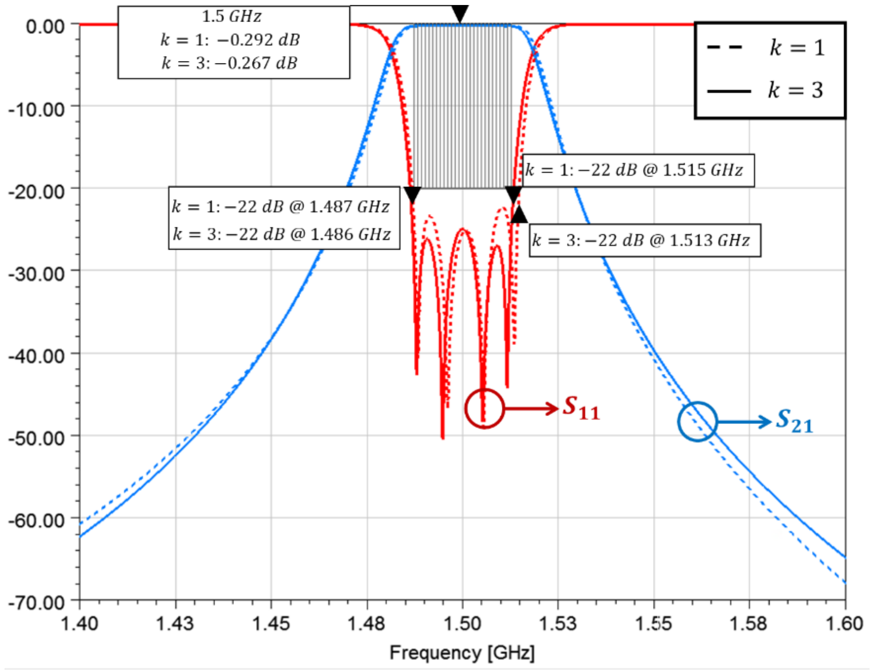

Figure IV.31 Topologies frequency responses comparison. Dashed lines represent the traditional topology (k=1), and continuous lines the novel topology (k=3)

After comparing both responses from Figure IV.*31*, it is observed that the novel topology and the traditional one have equivalent responses. In both cases, matching levels below 22 dB are obtained in the bandwidth. For the insertion losses, Figure IV.*32* shows a comparison of the transmission parameter S21 of both filters. Through the restricted band, insertion losses are above 0.5 dB in both cases although the novel topology shows a better performance than the traditional one, in coherence with a higher quality factor for the novel resonator topology.

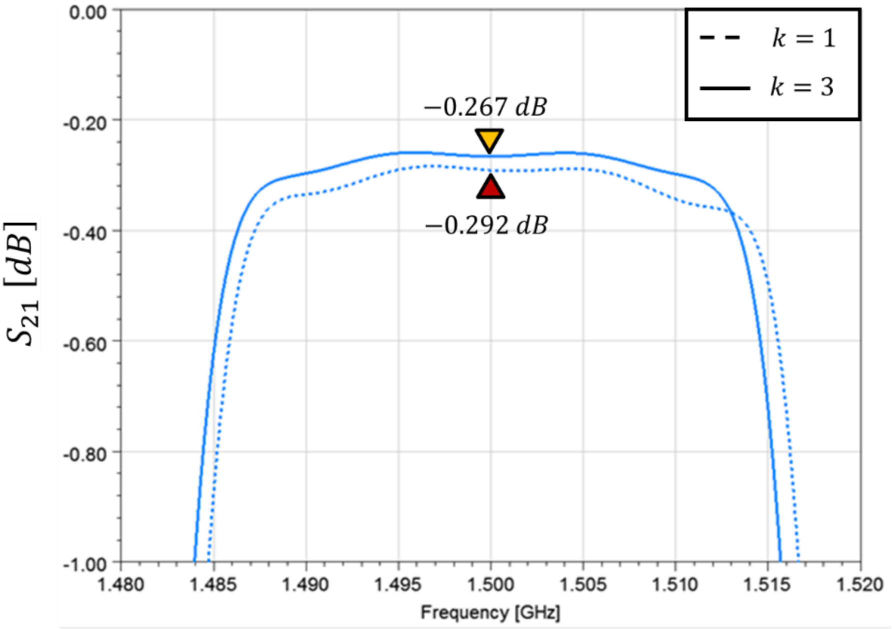

Figure IV.32 Insertion loss comparison

After the narrowband simulation, a broadband simulation between 1 GHz and 7 GHz was done to validate the broadband response of the filters and is presented in Figure IV.33. The theoretical frequency of the first harmonic obtained using (III-8) is $f_1 = 6.15\ GHz$, which agrees with the wideband response of the k=3 case, presenting a larger rejection band when compared with the traditional topology by almost 1 GHz although both cases have an impedance ratio $M = 2$. This can be explained by the higher sensibility of the traditional topology to small changes in dimensions.

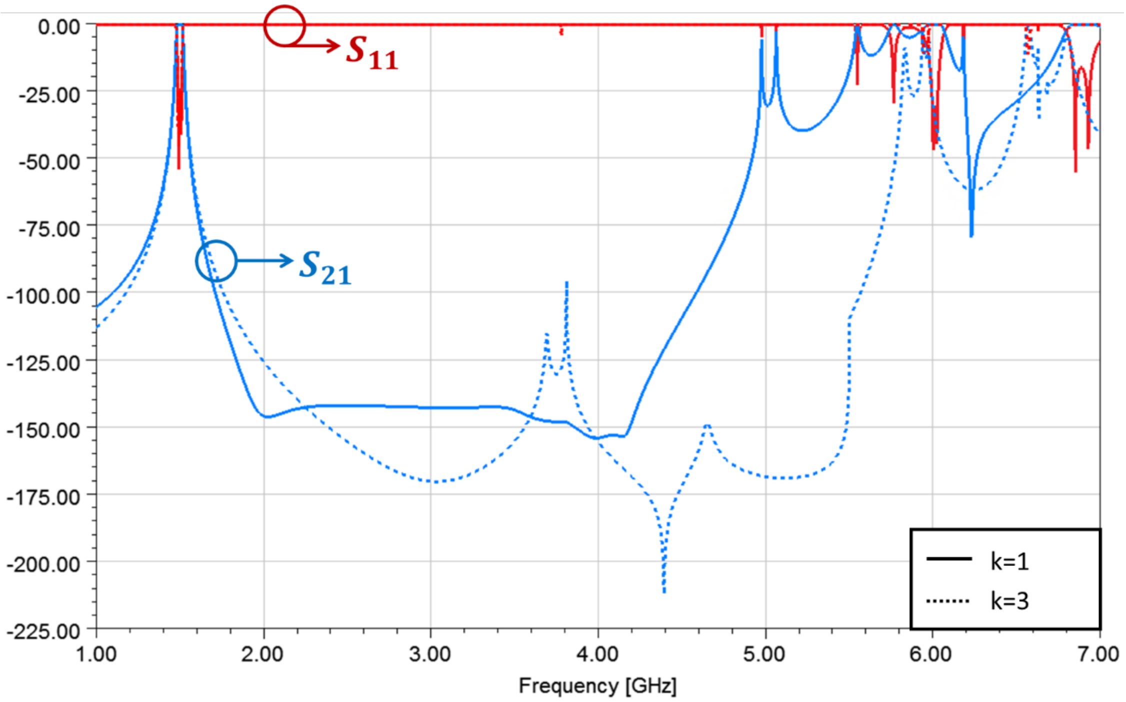

Figure IV.33 Wideband simulations for the k=1 and k=3 filters

IV.9.3 Multipactor simulations

After the validation of the novel topology, a multipactor analysis of the structure was done. Both structures were analyzed using SPARK 3D and CST-PIC considering the all-silver and a whole carbon coating variations. The results of these simulations are presented in Figure IV.34, and it can be seen that the power handling of the novel topology is approximately 10.8 dB greater than the traditional version for the all-silver configurations.

For the k=1 case, the use of carbon coating in the structure doubles the maximum power than can be handled by the filter, going from 2.5 W up to 5.4 W. With k=3 the difference between SPARK 3D and CST-PIC is important for the carbon coated case. Nevertheless, if we use PIC result as the maximum power that can be handled by the structure, the increase on this value is almost 3 times higher than the all-silver case. Finally, considering that both structures have similar dimensions, the combination of the novel topology with carbon coatings leads to a 15.3 dB gain for the multipactor threshold when compared with the traditional topology.

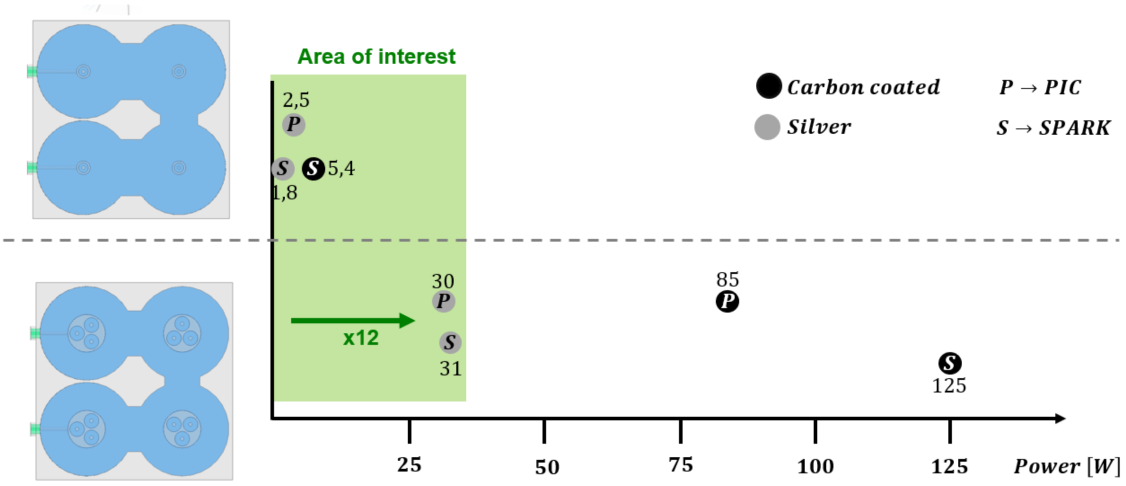

Figure IV.34 Multipactor handling results for k=1 and k=3.

For k=3, the electrons avalanche was observed with SPARK 3D (Figure IV.35) and PIC (Figure IV.36) showing that the break does occur inside the sections of the resonators. The gain on the multipactor threshold between topologies can be related to the increasement of the distance between the conductors of the inner sections.

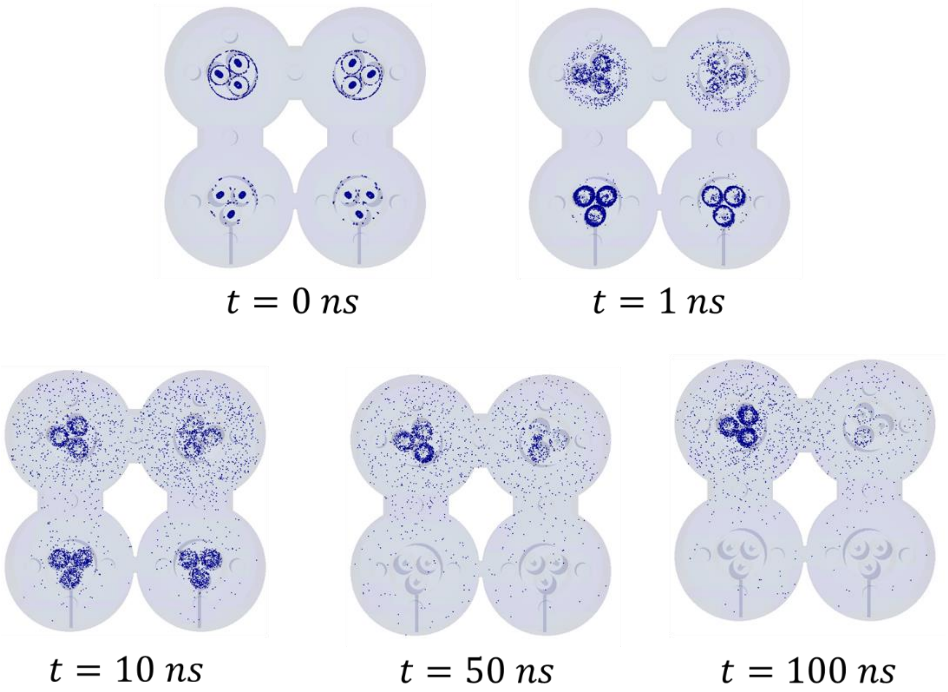

Figure IV.35 Electrons position over time on the simulated filter k=3

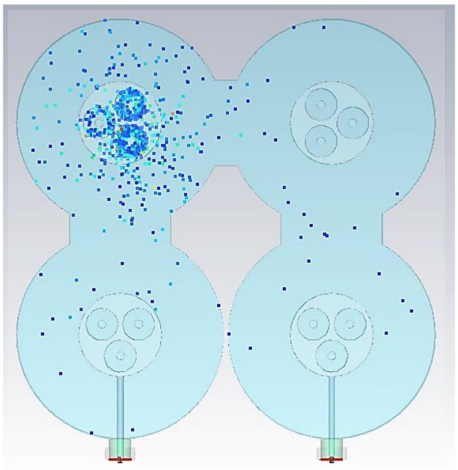

Figure IV.36 Electrons positions at 30 ns. Simulation done with CST PIC code

IV.9.4 Cross couplings and tuning screws

Before the fabrication of the filter, tuning screws that would compensate for fabrication defects were added. For each resonator, two screws make it possible to tune the frequency, and to adjust the bandwidth, one screw is set up on each iris to tune the coupling and, tunning screws for the input and output of the filter where also placed to control any defects on the conectors. These screws where placed in short circuit areas of the resonators, where their presence would not impact significantly the power handling of the structure. If tuning screws are placed wrongly, the power handling of the structure would be degraded.

Also, the possibility of a cross coupling between resonators 1 and 4 was conceived in order to show that this type of coupling could be integrated with the coaxial SIR with parallel sections. Figure IV.37 shows a top view of the 3D model with the tuning screws and the cross-coupling rod between the first and last resonators.

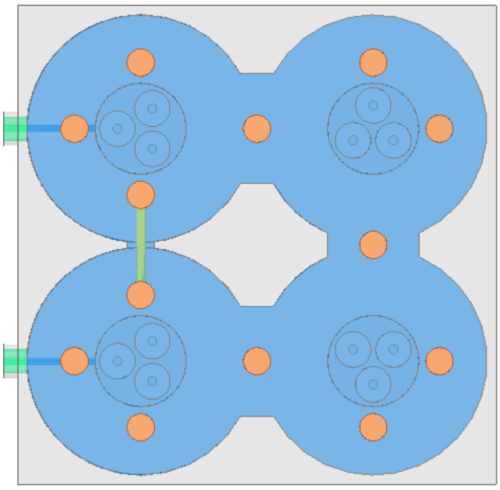

Figure IV.37 3D model of the k=3 filter with tuning screws and cross coupling

First, Figure IV.38 presents the simulated frequency response of the filter with tuning screws and without the cross coupling, it can be seen that the filter matches the desired specifications.

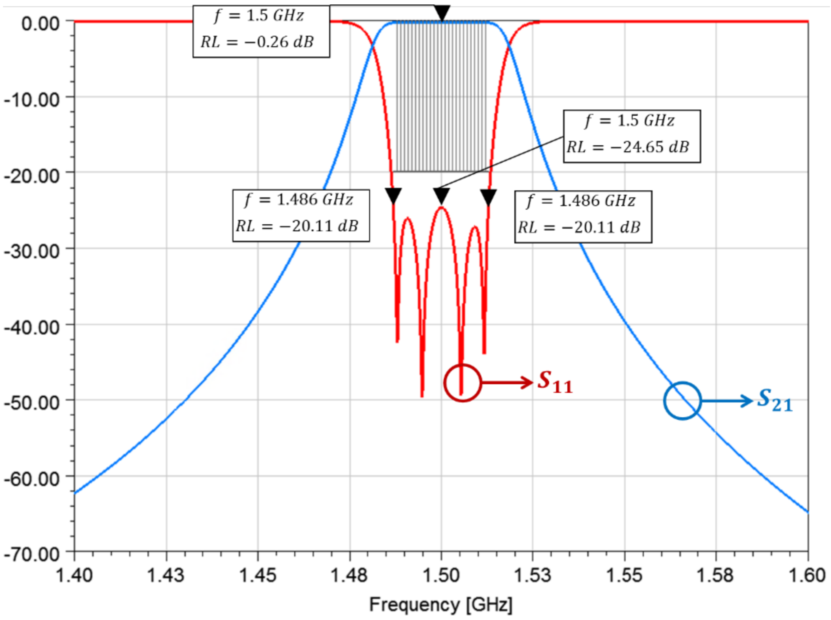

Figure IV.38 Simulated response of the filter with tuning screws

Then, in Figure IV.39 the impact of adding the cross coupling is presented. The two transmission zeros at 1.461 GHz and 1.53 GHz are clearly marked. Although the reflection parameter has been modified, the central frequency of the filter is kept, as the bandwidth of the filter. Since the addition of the cross coupling modifies the interaction of electromagnetic fields inside the structure, it is normal that it was slightly perturbated. A later tuning of the structure would result in a well-matched filter.

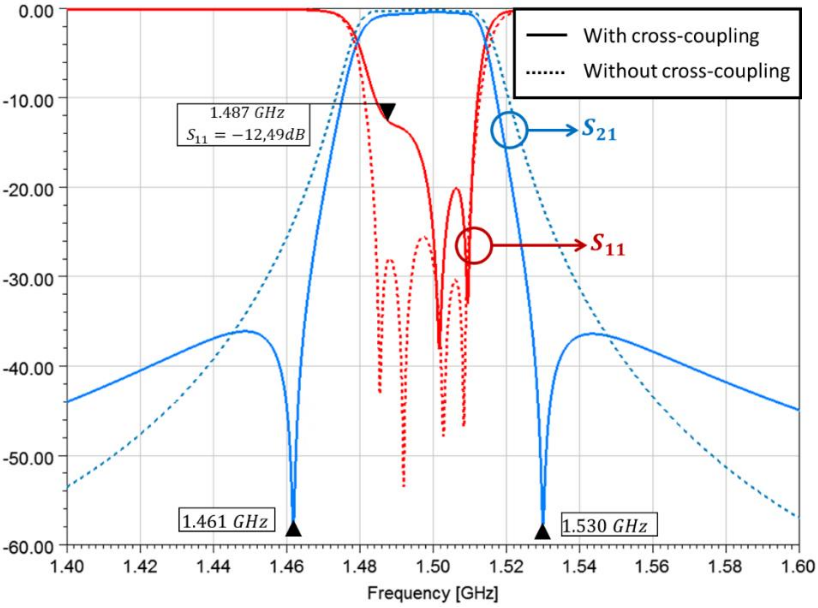

Figure IV.39 Simulated response of the filter with cross coupling

IV.9.5 Fabrication and measurement

The filter k=3 was fabricated entirely in aluminum and tested. For its fabrication, a process with tolerance of $\pm 50\mu m$ was used, the structure was manufactured in two blocks (body and cover) by Breizh usinage [29]. Also, 27 screws were added to hermetically close the RF volume. Pictures of the two parts of the filter are presented in Figure IV.40.

Figure IV.40 Fabricated filter k=3. Body (left) and cover (right) parts

First, narrowband measurements of the filter were done, and they are presented in Figure IV.41, showing a good agreement between the simulation and measurement, with a matching level below 29 dB for the measurements. Insertion losses of the measured filter are of 0.703 dB, while the simulated value was of 0.467 dB. This difference can come from different factors as the surface roughness of the fabrication process, the fillets of the tuning screws and that they are not hermetic, the contact between connectors and the structure since they were not soldered and possible calibration faults.

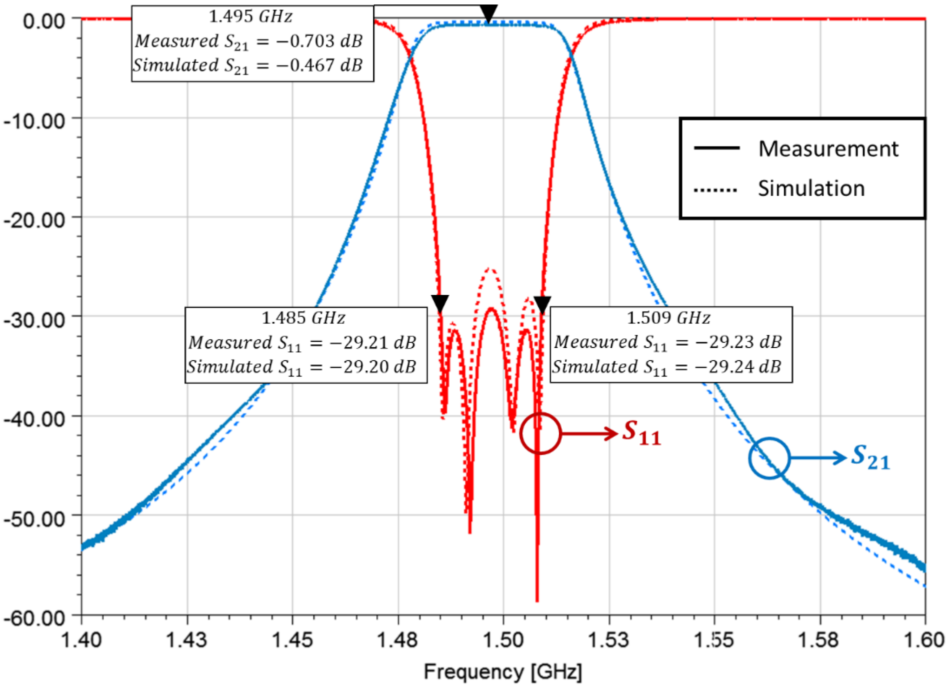

Figure IV.41 Narrowband measurement and simulation

Additionally, a broadband measurement of the structure was done, and compared to the wideband simulation of the fabricated structure in Figure IV.42. Here, a good agreement is also seen between the measurement and the simulations all over the band.

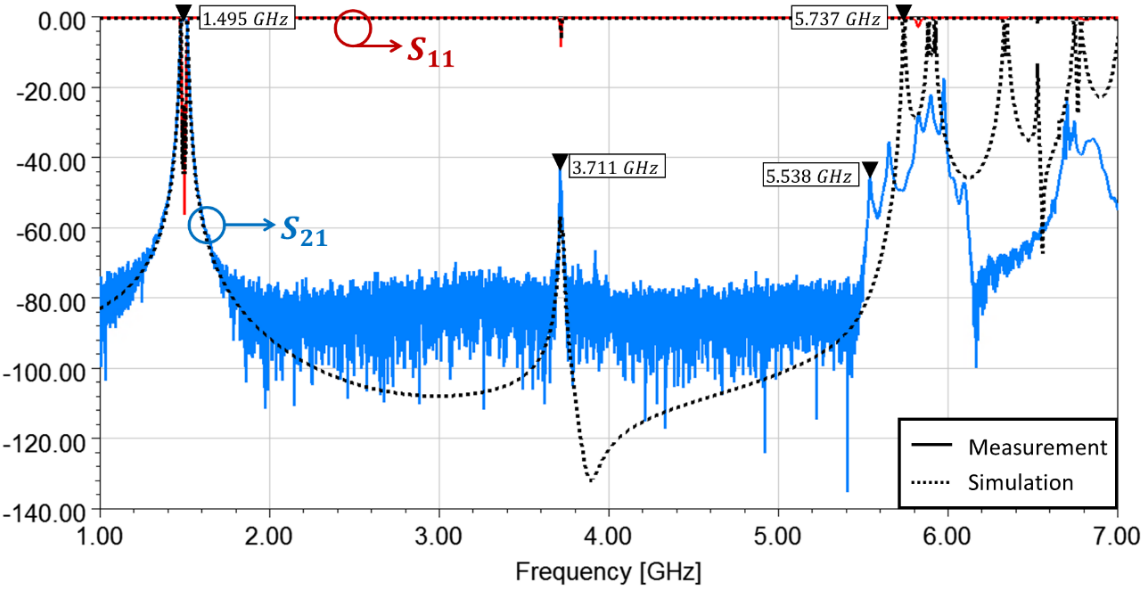

Figure IV.42 Wideband measurement and simulation comparison of the fabricated structure

As observed, a resonance appears at 3.71 GHz both in simulation and measurement. First, the electrical field was plotted inside the structure at this frequency to identify the resonance region as seen in Figure IV.43. From this figure, it was observed that the resonance does not correspond to a TEM coaxial mode of the resonator as the electrical field's distribution does not correspond to the one of a TEM mode.

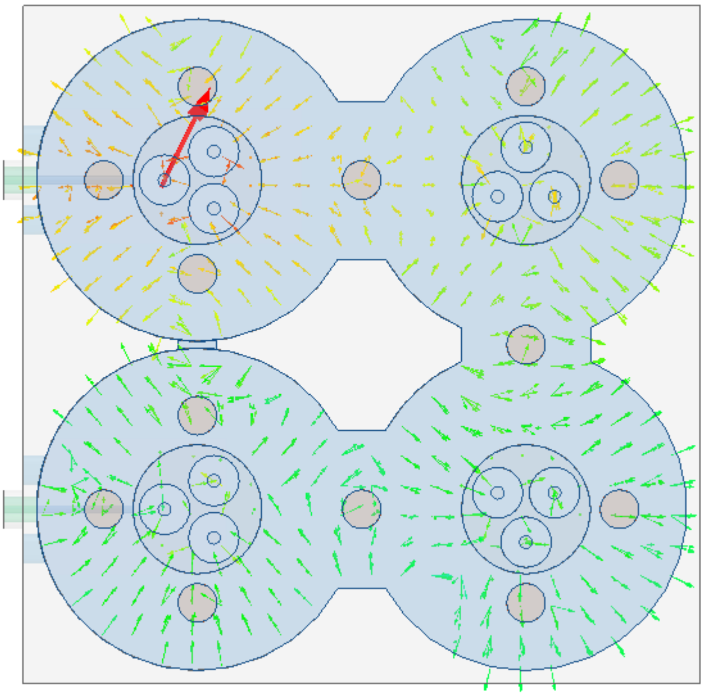

Figure IV.43 Electrical field of the k=3 filter with tunning screws at 3.71 GHz

Hence, eigenmode simulation of a single resonator was performed to better study this resonance and identify the source of this resonance. The results of this simulation are presented in Table IV.5, and two resonances (f_1 and f_2) at 3.81 GHz are presented between the fundamental resonant frequency of the resonator (f_0) at 1.5 GHz and the first harmonic (f_3) at 5.88 GHz. The plot of the electric field at f_1 is presented in Figure IV.44 presenting the same fields distribution as it was previously seen on the complete filter. In this figure it can be seen that the inside sections do present a TEM fields' distribution and with a higher intensity that on the outer section.

Table IV.5 Resonant frequencies of the k=3 resonator

$\boldsymbol{Frequency}$	$f_0\ [GHz]$	$f_1\ [GHz]$	$f_2\ [GHz]$	$f_3\ [GHz]$	$f_4\ [GHz]$	$f_5\ [GHz]$
$\boldsymbol{k=3}$	1.5	3.81	3.81	5.88	6.75	6.75

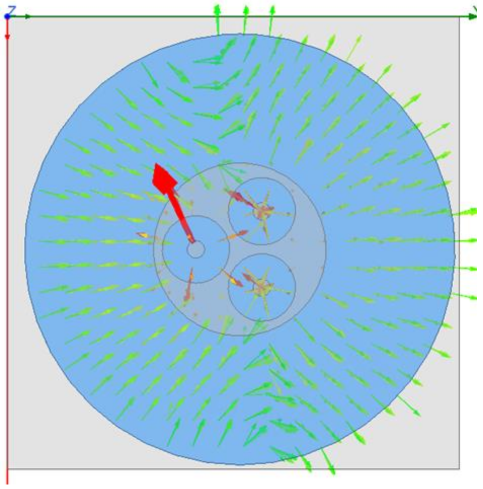

Figure IV.44 Electric field distribution at 3.81 GHz on the k=3 resonator

The source of the resonances can be explained by the existence of a TE_{111} resonance appearing in the external section of the resonator, and the interaction of TEM modes inside the internal C_2 cylinders generating a pseudo $\lambda/2$ resonator. One hypothesis suggest that these modes interact between them creating the hybrid parasitic resonances.

To verify if the first hypothesis was feasible, we should first determine if the TE_{11} mode (as shown in Figure IV.46) could propagate on a coaxial waveguide with the dimensions of the outer section at this frequency, then a TE_{111} resonance could be established. Figure IV.45 shows the cutoff frequencies on a coaxial transmission line with external radius $R_1 = 25\ mm$ and internal radius $r_1 = 10.02\ mm$. The cutoff frequency for the TE_{11} mode in a coaxial transmission line of the stated dimensions is of 2.77 GHz, meaning that a resonance at 3.71 GHz could appear.

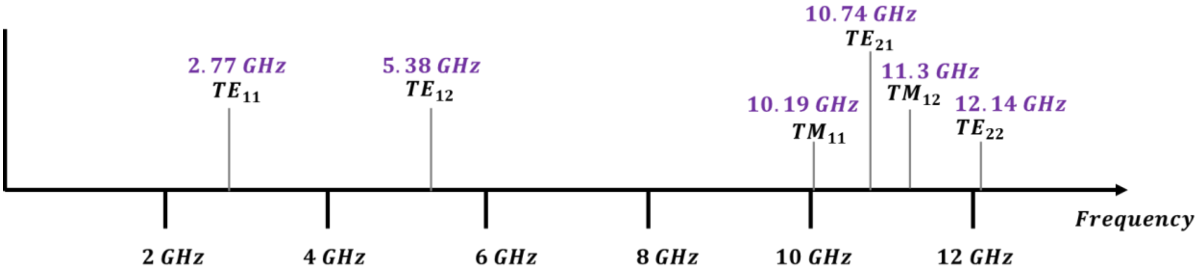

Figure IV.45 Cutoff frequencies on a coaxial transmission lines with dimensions $R_1 = 25\ mm$ *and* $r_1 = 10.02\ mm$

Although the TE_{111} resonance can exist at 3.71 GHz it is unlikely that this mode resonates at the same time with a TEM resonance in the inner sections allowing the energy to be transferred from one resonator to another throughout the filter.

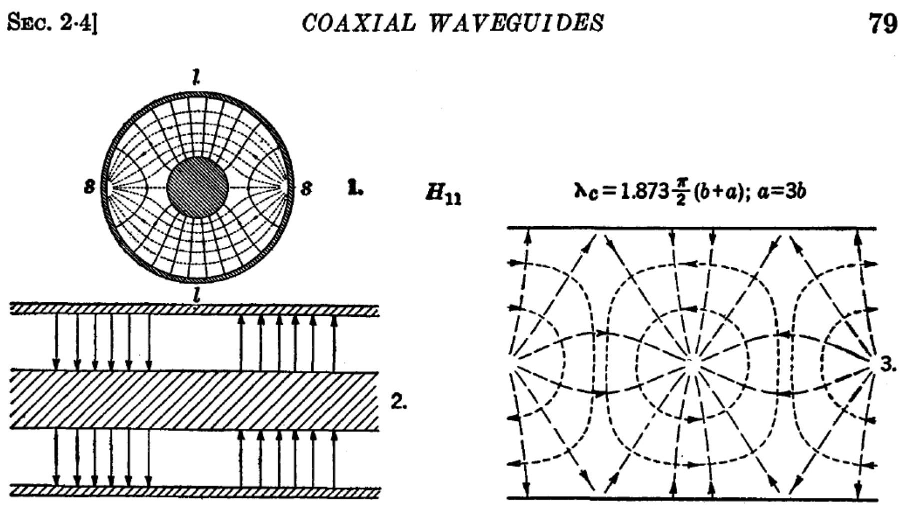

Figure IV.46 TE_{11} mode on a coaxial waveguide taken from [31]

For the second hypothesis, eigenmode simulations of a single resonator were performed from k=1 to k=5. Results of this simulations are presented in Table IV.6 showing the length l of every resonator section for the different configurations, and its corresponding fundamental resonance frequency f_0 at 1.5 GHz (blue). In agreement with equation (IV-4), the first harmonic for a M=2 is around 5.8 GHz. However, as the number of inner sections in parallel increases, additional resonances appear between the TEM resonances. When analyzing the case k=3, two resonances at 3.81 GHz are identified by the eigenmode simulation, in agreement with the measured resonance at 3.71 GHz. It is important to note that as an additional section is added in parallel, a new parasitic resonance appears following a tendency of k-1 parasitic resonance frequencies, reinforcing the hypothesis that these resonances come from an interaction between the inner parallel sections.

Table IV.6 Eigenmode simulation results for the two-section coaxial SIR resonant frequencies M=2

	$k = 1$	$k = 2$	$k = 3$	$k = 4$	$k = 5$
$l[mm]$	12.8	11.5	11.1	11.1	10.9
$f_0\ [GHz]$	1.5	1.49	1.5	1.49	1.48
$f_1\ [GHz]$	5.76	3.73	3.81	3.54	3.36
$f_2\ [GHz]$	6.9	5.76	3.81	3.54	3.36
$f_3\ [GHz]$	7.55	6.84	5.88	4.17	3.97
$f_4\ [GHz]$	7.55	7.31	6.75	5.9	4.20
$f_5\ [GHz]$	7.87	8.18	6.75	6.54	5.92

Then, as a first validation, the external impedance of the resonator was modified, in order to obtain different resonant frequencies for the fundamental and the first harmonic. If these additional resonances come from only the internal section, these resonant frequencies would be at the same frequency, or very close. Table IV.7 shows the results for a resonator with an impedance ratio M=2.4, with a resonant frequency $f_0 = 1.38$ GHz and the first harmonic at 5.69 GHz, for the k=3 case. As the impedance ratio is larger, f_0 is lower and the first harmonic will appear at a higher frequency, as presented by the results on Table IV.7. In addition, the parasitic resonant frequencies did not shift significantly.

Table IV.7 Eigenmode solution for the resonant frequencies on a coaxial SIR resonator with M=2.4

	$k = 1$	$k = 3$
$l[mm]$	12.8	11.1
$f_0\ [GHz]$	1.43	1.38
$f_1\ [GHz]$	5.16	3.788
$f_2\ [GHz]$	6.26	3.789
$f_3\ [GHz]$	6.23	5.69
$f_4\ [GHz]$	3.33	6.45
$f_5\ [GHz]$	7.65	6.45

Then, a resonator with a lower impedance ratio M=0.89 was simulated and Table IV.8 shows the results for this simulation. For an impedance ratio M smaller than 1, the fundamental resonant frequency f_0 of the resonator will be larger and the first harmonic will appear before in the frequency band as presented in the results of Table IV.8. The frequency ratio between the first harmonic and the fundamental resonant frequency of this configuration is of 2.8, that compared to the theoretical ratio of 2.85 calculated with the help of (III-8), shows that the frequencies at 3.9 GHz correspond to the internal sections.

Table IV.8 Eigenmode solution for the resonant frequencies on a coaxial SIR resonator with M=0.89

	$k = 1$	$k = 3$
$l[mm]$	12.8	11.1
f_0 $[GHz]$	1.74	2.10
f_1 $[GHz]$	5.98	3.90
f_2 $[GHz]$	8.61	3.90
f_3 $[GHz]$	8.61	5.88
f_4 $[GHz]$	9.45	6.97
f_5 $[GHz]$	11.97	6.97

Following the hypothesis that the parasitic resonant frequencies come from the interactions between the internal parallel sections, it was proposed that a pseudo-half wave resonator was established between each on the sections. As shown in Figure IV.47 for a case k=2, the length of the pseudo-half wave resonator will be 2 times the length of the internal sections l and the distance l_ε.

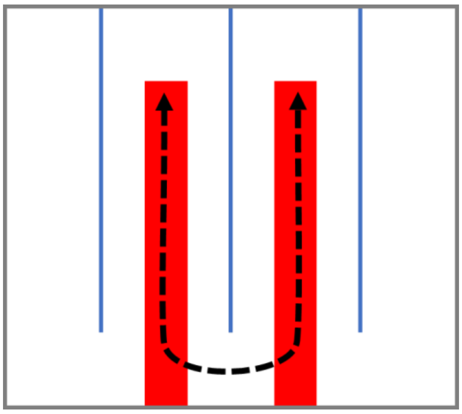

Figure IV.47 $\lambda/2$ resonator model between internal parallel sections

To confirm this model, eigenmode simulation of only the internal sections of the k=3 resonator was done to identify the first resonant frequency of the resonator. The first resonant frequency was found to be at 3.79 GHz, and the electrical field distribution of the field showed that this resonance corresponded to a TEM mode as presented in Figure IV.48.

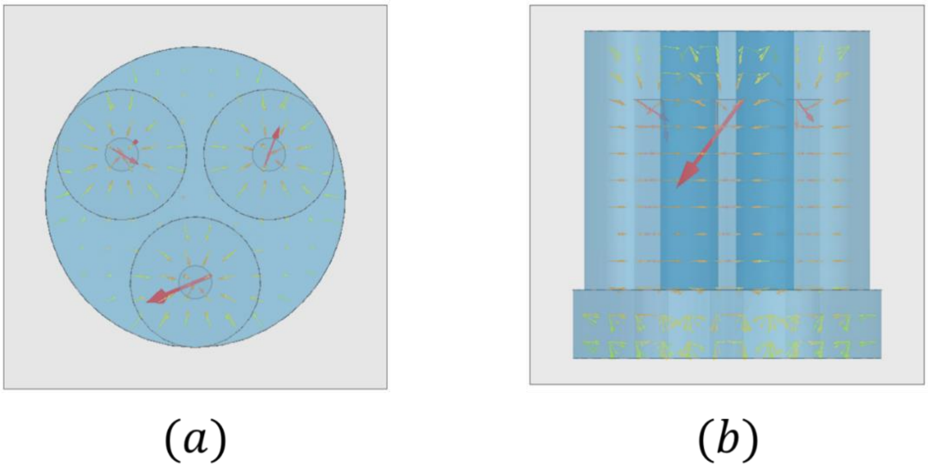

Figure IV.48 Top (a) and front (b) view of the electrical field distribution in a resonator with 3 sections in parallel at 3.79 GHz

As a last study, the internal characteristic impedances were modified in a way that the global impedance ratio was kept at M=2, but the impedance $Z_2 = 27.3\ \Omega$ was not obtained from 3 identical sections with characteristic impedances $Z'_{2\,a} = Z'_{2\,b} = Z'_{2\,c} = 81.9\ \Omega$. Instead, two of them would be equal and one of the characteristic impedances would be different but keeping the same equivalent impedance $Z_2 = 27.3\ \Omega$ ($Z'_{2\,a} = Z'_{2\,b} \neq Z'_{2\,c}$) as shown in Figure IV.49, the corresponding values are $Z'_{2\,a} = Z'_{2\,b} = 123.45\ \Omega$ and $Z'_{2\,c} = 49.04\ \Omega$.

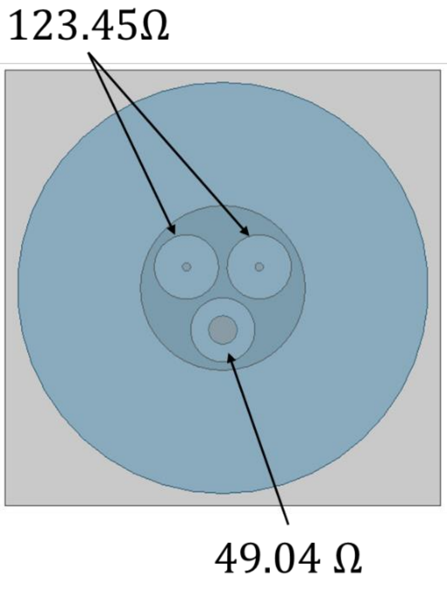

Figure IV.49 Coaxial SIR resonator with k=3 and $Z'_{2\,a} = Z'_{2\,b} \neq Z'_{2\,c}$ configuration

If a resonator between parallel sections is formed, the parasitic resonant frequencies should be different since an SIR effect would appear between the sections with different characteristic impedances. Table IV.9 presents the resonant frequencies result of eigenmode simulations of the structure. With a fundamental resonant frequency $f_0 = 1.50\ GHz$ and the first harmonic at

5.81 GHz, in agreement with theory, even though the resonator is not symmetrical anymore. For the parasitic resonances, 2 resonances appear at different frequencies each one, first a resonance at 3.74 GHz, corresponding to the interaction between the sections with a different characteristic impedance as it can be observed in Figure IV.50 (a). The second parasitic resonant frequency appears at 4.05 GHz, and as observed in Figure IV.50 (b) is governed by the sections with a same characteristic impedance.

Table IV.9 Eigenmode solutions for a coaxial SIR resonator with k=3 and $Z'_{2\,a} = Z'_{2\,b} \neq Z'_{2\,c}$ *configuration*

	$k = 3$
$l[mm]$	11.1
$f_0\ [GHz]$	1.50
$f_1\ [GHz]$	3.74
$f_2\ [GHz]$	4.05
$f_3\ [GHz]$	5.81
$f_4\ [GHz]$	6.66
$f_5\ [GHz]$	6.84

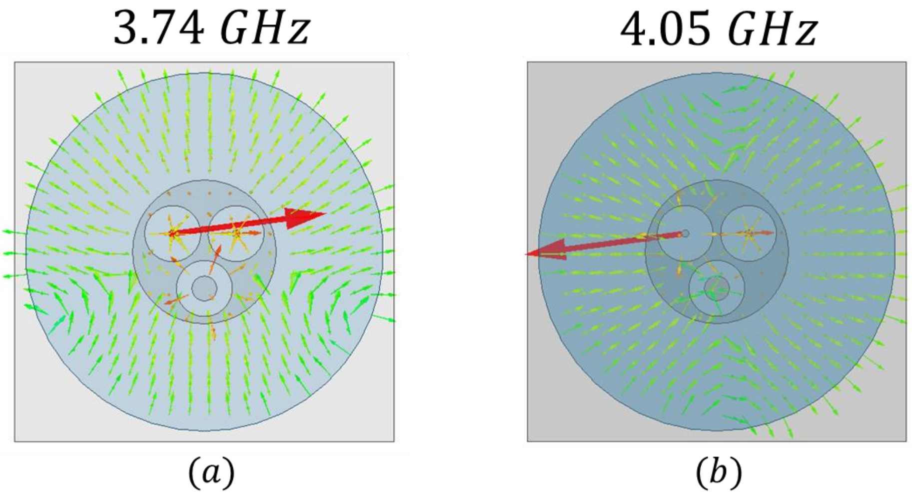

Figure IV.50 Electrical field distribution for a coaxial SIR resonator with k=3 and $Z'_{2\,a} = Z'_{2\,b} \neq Z'_{2\,c}$ *configuration at 3.74 GHz (a) and 4.21 GHz (b) resonant frequencies.*

With the given information, the most feasible explanation for the parasitic resonances seems to be the interaction between parallel inner sections. As the number of parallel sections increases, each new resonance frequency will correspond to a new type of interaction between sections as shown in Figure IV.51. For k=2 and k=3, only one type of interaction can exist between resonators, while for k=4 and k=5, 2 and 4 different types of interactions can exist in terms of the distance between the sections, respectively.

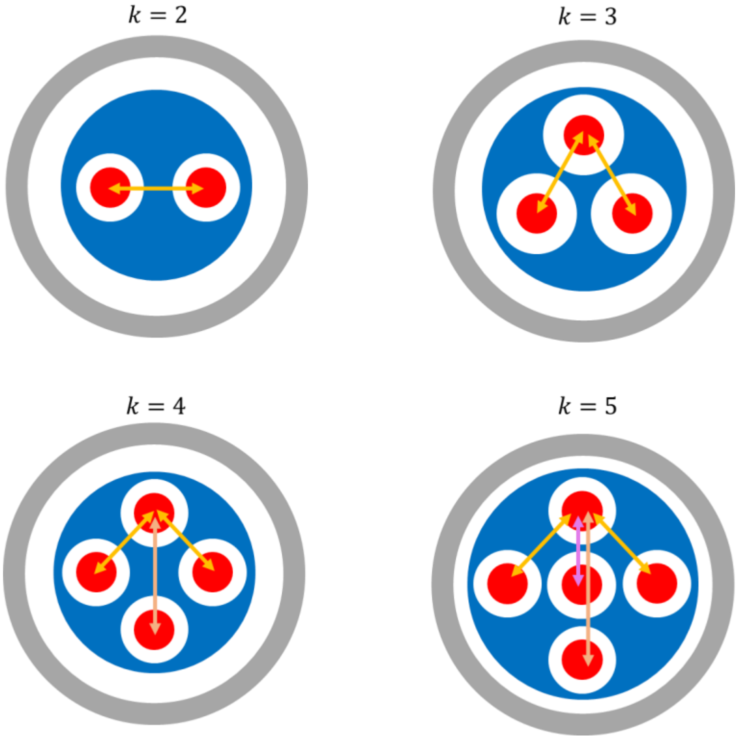

Figure IV.51 Types of interactions between parallel sections

After that, a cross-coupling rod between resonators 1 and 4 was added to increase the rejection around the passband by introducing two transmission zeros on each side of the bandpass. It was fabricated using a copper rod with a diameter of 1.8 mm, and a low-density foam to keep it in place and isolate it from the body of the filter. This cross-coupling rod was added to the tuned filter without later tuning as presented in Figure IV.52.

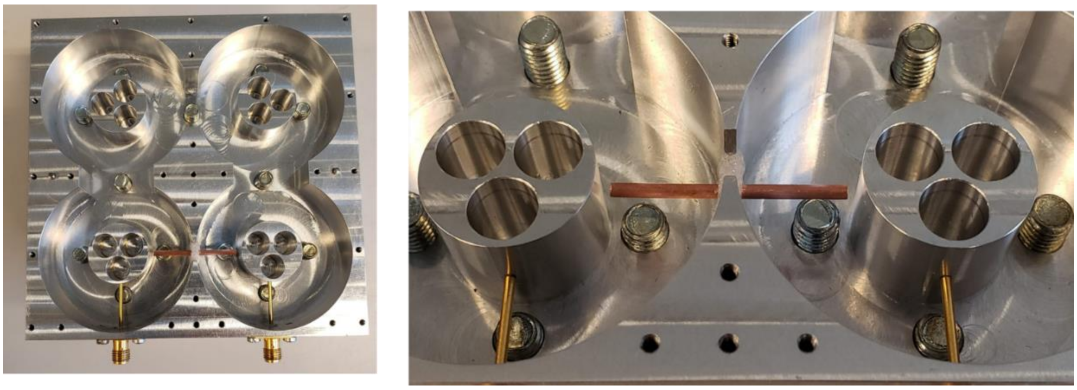

Figure IV.52 Cross coupling rod between resonators 1 and 4

When adding this coupling rod, the filter response is modified as it can be seen in Figure IV.53, and the filter can be easily tuned back to a more appropriate response. However, the most important thing, is the apparition of the transmission zeros, and the good agreement between the simulation and the final measurement.

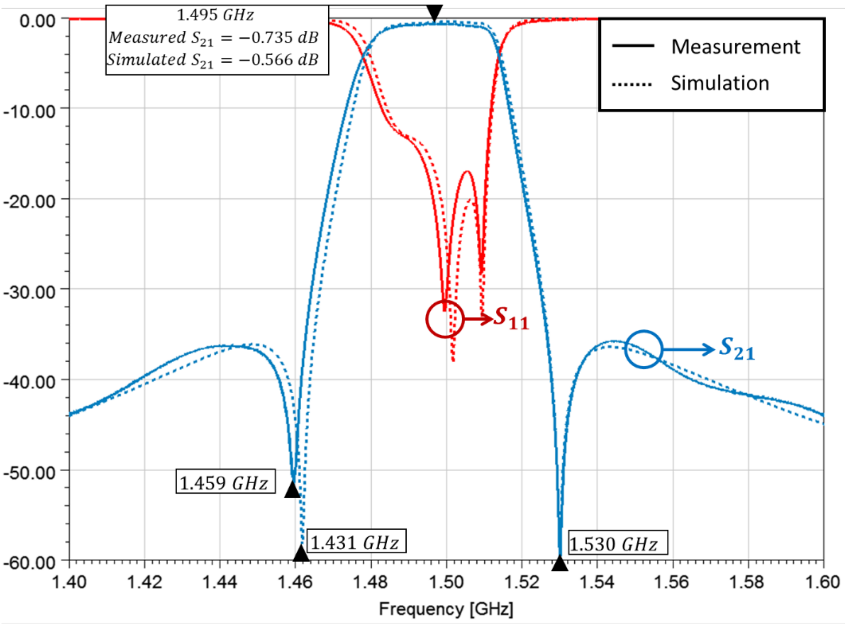

Figure IV.53 Measurement and simulation of the tuned filter with cross couplings

Finally, the cross coupling can be modified by changing the length of the coupling rod, and so the gaps between the rod and the central cylinder. A second rod with a different length of 28.48 mm was manufactured to make a second cross coupling with the transmission zeros placed at different frequencies. A comparison of the measured filter responses with these two couplings is presented in Figure IV.54.

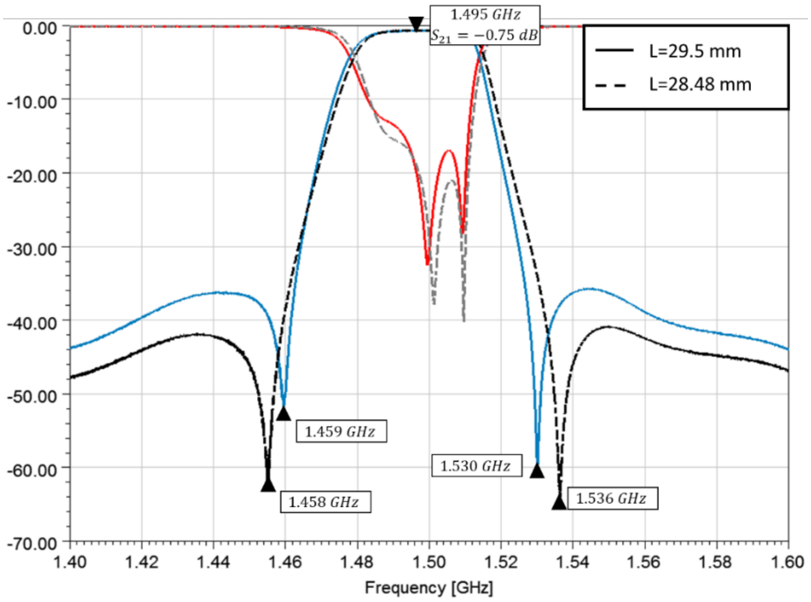

Figure IV.54 Measurement of the tuned filter with different cross couplings

IV.10 Chapter IV conclusion

The parallel internal sections approach showed to have an electrical response equivalent to the traditional coaxial SIR in both simulation and measurements. This new topology also allows the use of cross couplings for their use in more complex filter topologies other than linear. In addition, this topology allows to optimize a resonator's quality factor resulting in lower insertion losses on a filter with the same dimnesions. The model used for the modeling of the quality factor agrees with eigenmode simulations and allow the determination of an optimal solution without the need of a 3D simulation.

On the other hand, the parallel inner sections resonator is less sensitive to fabrication defects or tolerances since physical constrains are lowered by increasing the distance between conductors. The larger distance between conductors also translates in better power handlings of the filters, resulting in a gain greater than 10 dB for the studied case, and more than15 dB gain if we consider a carbon coating on the structure.

However, with this topology, parasitic resonances might appear at undesired frequencies, as it was the case of this study. Although this resonance was badly coupled (under -40 dB) is it important to consider it for future implementations. Also, although it proposed that this parasitic resonance comes from the interaction of the parallel sections, a more detailed study must be done to better understand how to mitigate the apparition of these resonances or use them for future filter implementations.

Chapter V : Dielectric filling

V.1 Introduction

In this chapter, a preliminary study of the impact of dielectric materials inside critical areas was performed. As a multipactor discharge occurs in the vacuum, by filling these gaps with a dielectric a discharge cannot occur. In this chapter we will present the results of a 2nd and a 4th order filter that were studied and the impact of using dielectrics within them. It is important to note that the dielectric will also have an impact on the dimensions and electrical performances of the filter [32] - [33].

V.2 Dielectric modelling

The first step before running simulations was to know the characteristics of different dielectric materials that could be used. In terms of electrical performance, the selected dielectric should have a low loss tangent to decrease its impact on the overall losses of the filter. As expected, the redhibitory effect of using dielectric materials in resonators or filter is the reduction of the quality factor. Table V.1 presents the dielectric properties of commonly used dielectrics.

Table V.1 Dielectric properties of commonly used dielectrics

$\boldsymbol{Dielectric}$	$\boldsymbol{\varepsilon_r}$	$\mathbf{tan}\ (\boldsymbol{\delta})$
FR4	4.4	0.02
Teflon	2.1	0.001
Alumina	9.8	0.0003-0.003
Rexolite (quartz)	3.78	0.0066

Additionally, the SEY characteristics of the dielectrics must be known, as this will impact the power performance of the device. Information about the SEY of some dielectrics is presented in the Table V.2. In addition to this table, the information presented in [34] reported similar results.

Table V.2 SEY properties of different dielectric materials [32]

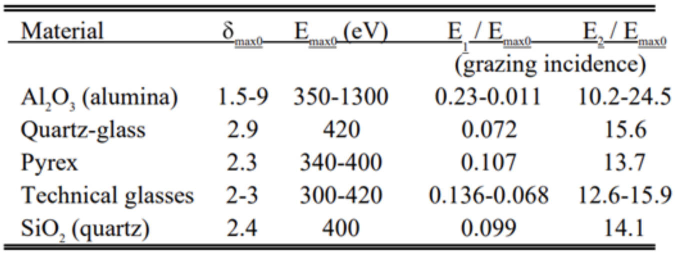

Material	δ_{max0}	E_{max0} (eV)	E_1 / E_{max0}	E_2 / E_{max0}
			(grazing incidence)	
Al_2O_3 (alumina)	1.5-9	350-1300	0.23-0.011	10.2-24.5
Quartz-glass	2.9	420	0.072	15.6
Pyrex	2.3	340-400	0.107	13.7
Technical glasses	2-3	300-420	0.136-0.068	12.6-15.9
SiO_2 (quartz)	2.4	400	0.099	14.1

Additional to the SEY of the dielectric, a new factor must be considered in the multipactor simulations. The dielectric material will charge and induce a DC field that will interact with the RF field of the structure as presented in Figure V.1. The interaction of these fields modifies the conditions for multipactor to occur, changing the direction and intensity of the overall field. This increases the complexity of modeling the multipactor breaks inside RF structures and the simulation of this phenomena. In our case, after consulting with specialist at Thales Alenia Space, the impact of the DC field was not considered for multipactor simulations due the higher complexity of integrating this, into the simulations and the high incertitude that this leads to the results. In practice, as the incertitude of the electromagnetic modeling of these structures with dielectric material increases, the security margin to consider a simulation result to be acceptable, or interesting as a potential multipactor mitigation technique, is leveled up to 12 dB.

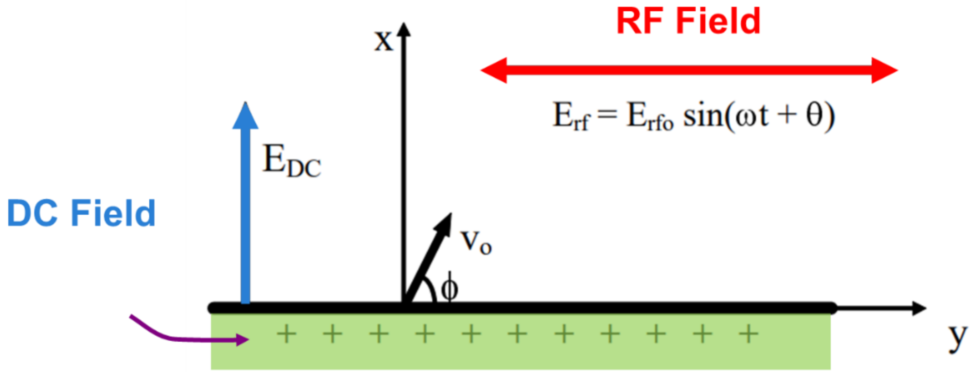

Figure V.1 interaction between the RF and DC fields [32].

V.3 Structure design with dielectric filling

V.3.1 2nd order filter

First, a second order filter was tested to evaluate the impact of having a dielectric filling as multipactor mitigation technique. The designed filter corresponds to the same configuration as the one chosen for the power handling test structure in Chapter IV. For this design, the coupling distance $l\varepsilon$ was set to 1 mm as presented by Figure V.2 to create a critical region in this area. The corresponding frequency response of this structure is presented in Figure V.3.

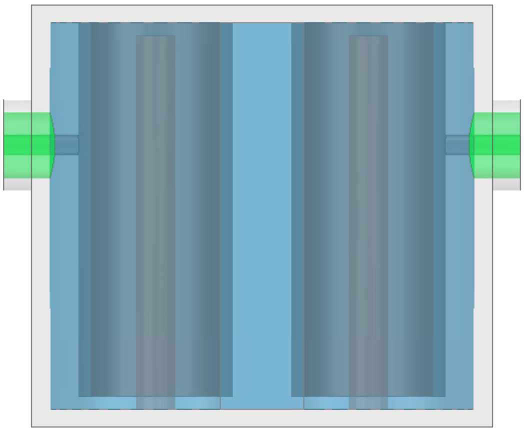

Figure V.2 Front view of the 2nd order two-section coaxial SIR filter with $l\varepsilon = 1\ mm$

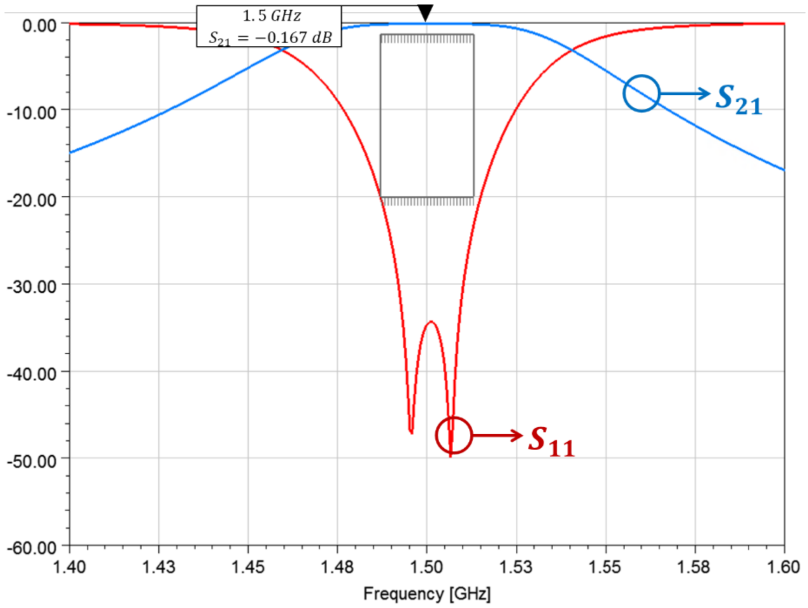

Figure V.3 Frequency response of the filter with $l\varepsilon = 1\ mm$

Once the filter was tuned, the power handling simulations were performed using SPARK3D. With a power handling of 2.47 W, the multipactor break was observed to occur in the coupling $l\varepsilon$ region environment as expected and presented in Figure V.4. It is important to remember that the original structure with $l\varepsilon = 4\ mm$ presented a power handling of 37 W and the break occurred between the conductors of the inner section.

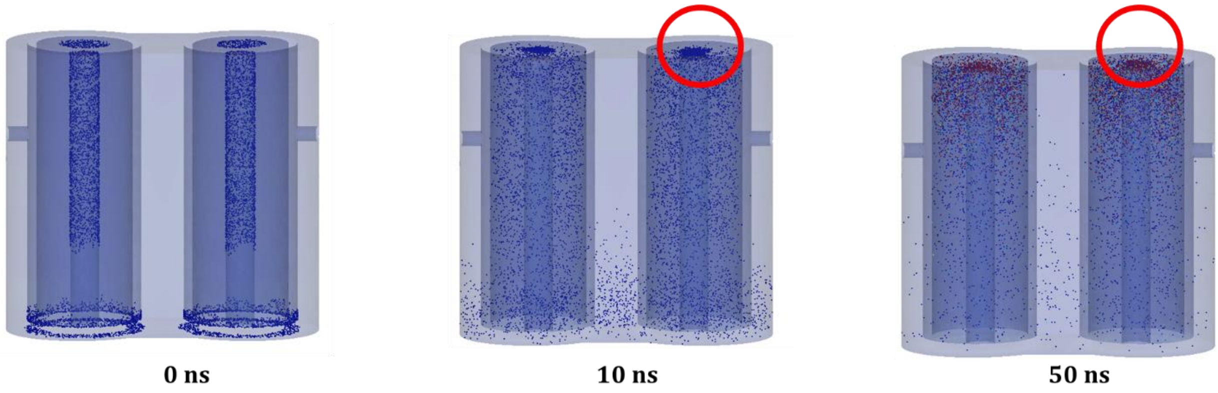

Figure V.4 Electrons position in the 2nd order filter with $l\varepsilon = 1\ mm$

Additional to the SPARK3D simulations, the structure was simulated with CST-PIC to ensure a good meshing in the 1 mm gap as presented in Figure V.5. As a result of this simulation a maximum power handling of 2.2 W was determined, a difference of 0.5 dB was observed between both simulations, a difference that can be neglected.

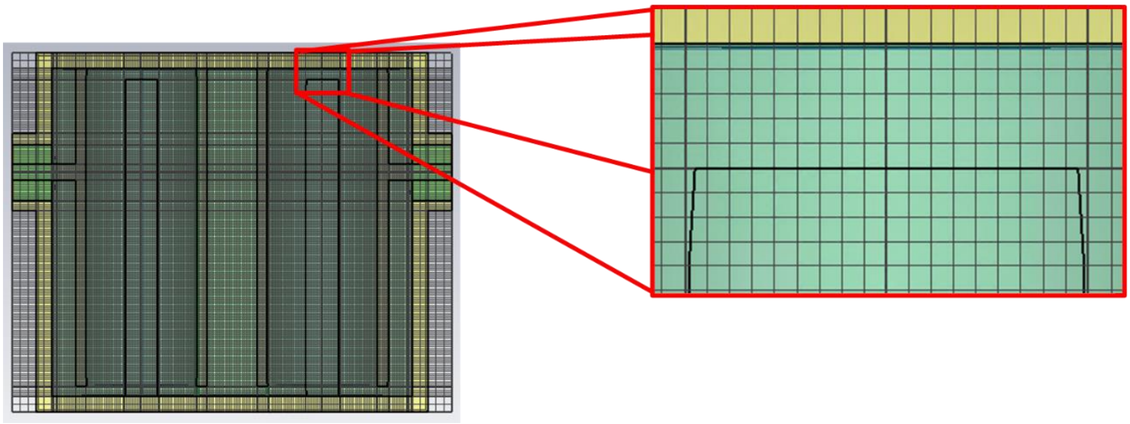

Figure V.5 Front cut view of the CST model and meshing for multipactor simulations of the 2nd order filter

By using particle monitor of CST, we could confirm that the break occurred in the coupling $l\varepsilon$ region of the inner section in accordance as seen on Figure V.6 with the results obtained with SPARK3D.

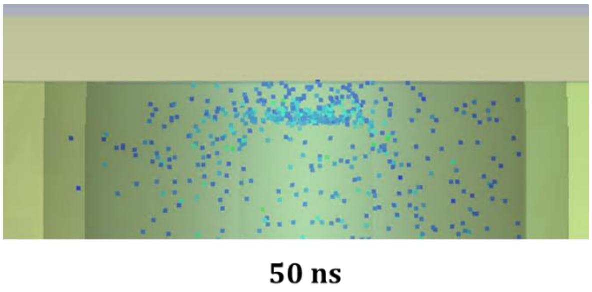

Figure V.6 Detailed view of the electrons position at 50 ns in the 2nd order filter

With a reference value of 2.2 W for the power handling, and with a break in the coupling $l\varepsilon$ region of the inner section, a dielectric disc and a dielectric ring were added in the two open-ended coupling section of each resonator as presented in Figure V.7. Ideally, these dielectric fillings will impeach the apparition of a break in these regions.

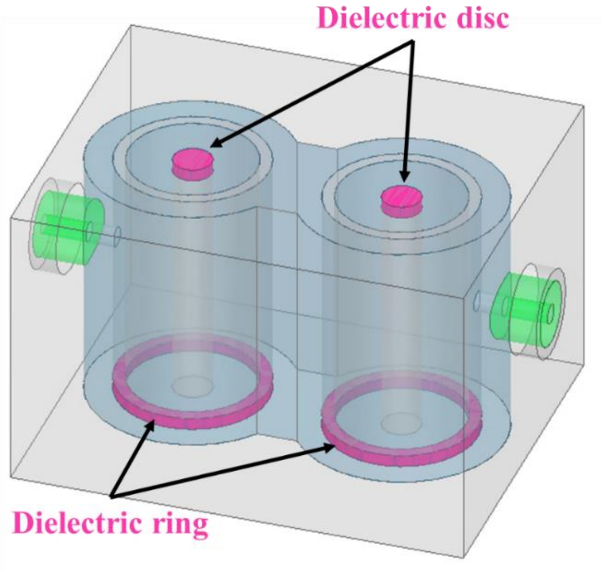

Figure V.7 2nd order two-section coaxial SIR filter will dielectric fillings

Depending on the chosen dielectric, the length of the resonator must be modified as the dielectric impacts the electrical length of the resonator, and this must be adjusted. On a first approach, Alumina was chosen as it is currently used for space applications. As a result, the total heigh of the structure was reduced by 19.7%, resulting in a heigh of 24.2 mm compared to the original 34.45 mm. Both responses are compared in Figure V.8 showing that both configurations have similar frequency responses. Even though the dielectric discs and rings were included, the difference in the insertion losses is lower than 0.5 dB when compared with the filter with no dielectric insertions, while using a loss tangent $tan(\delta) = 0.0004$.

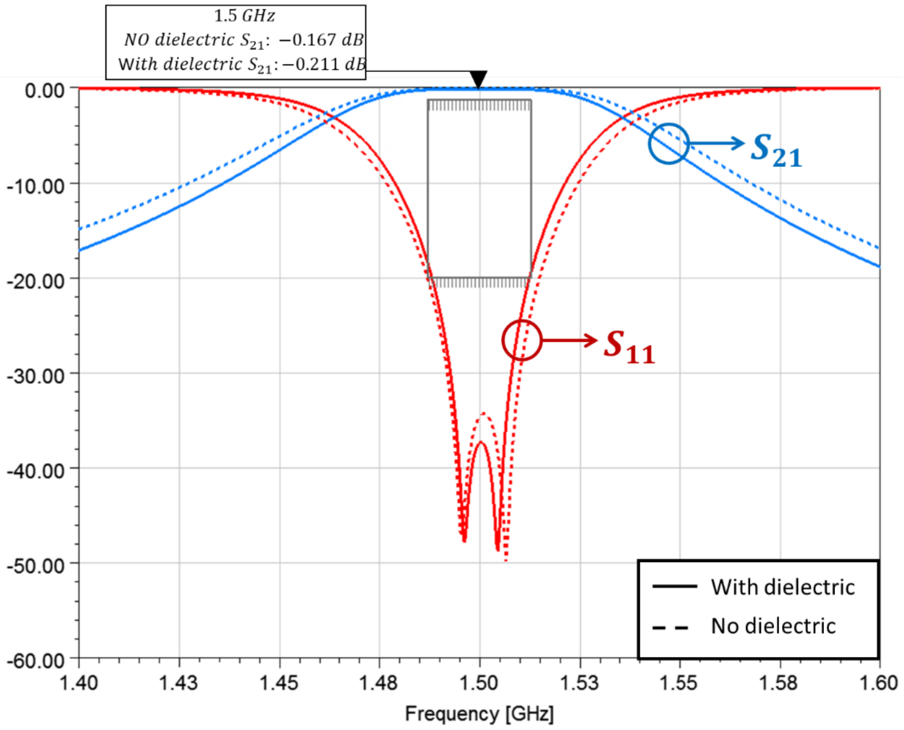

Figure V.8 Frequency response comparison between the filter without (dashed) and with (continuous) dielectric fillings

For the multipactor simulations, the chosen SEY parameter for the alumina are a first crossover energy $E_1 = 22.2$ eV , a maximum SEY $\delta_{max} = 7.01$ and an $E_{max} = 923$ eV. A comparison between SEY curves of alumina and the Silver is presented in Figure V.9. It can be seen that the dielectric has higher values and could lead to a break in a vicinity the region of the dielectric.

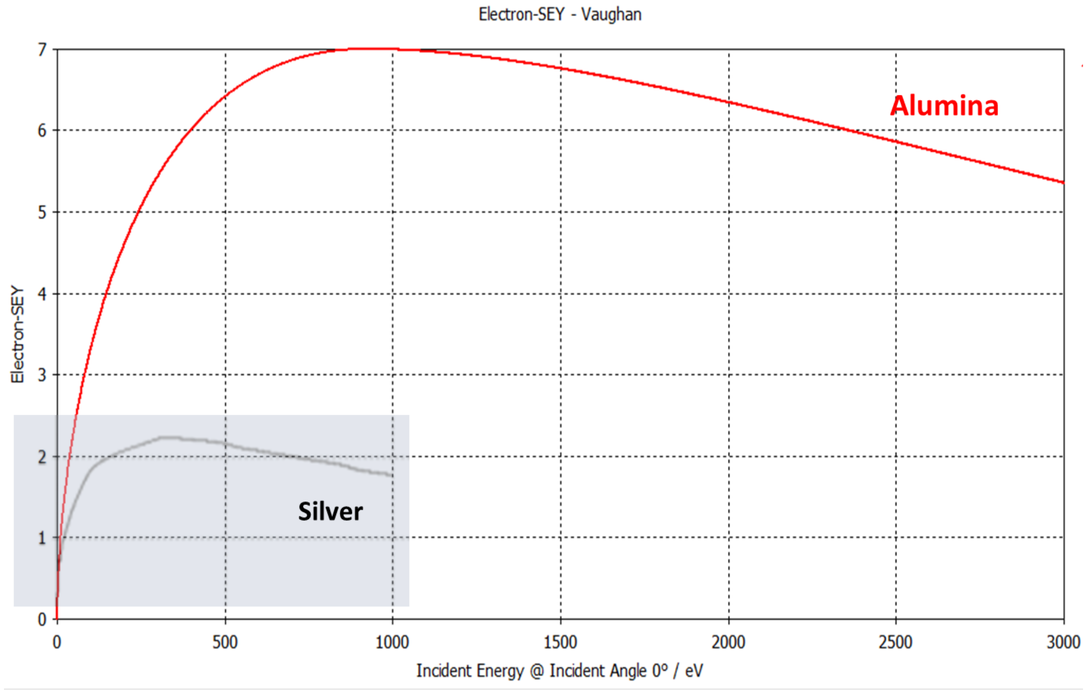

Figure V.9 SEY comparison between Alumina (red) and Silver (grey)

Power handling simulations showed that the power handling of the filter was increased by 14.36 dB, superior to the security margin of 12 dB, resulting in a maximum power of 60 W. Particles tracking using the position monitor of CST showed that the break occurred between the walls of the inner coaxial section of resonator in a uniform way all along the section as presented in Figure V.10.

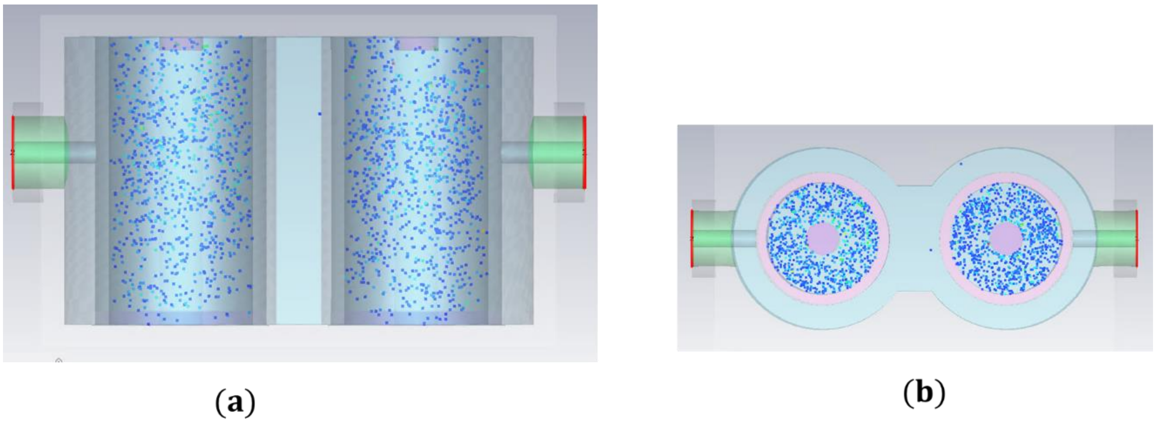

Figure V.10 Particle tracing (a) front view,(b) top view.

The use of dielectric filling structures on critical environments of the structure appears to be an effective way to prevent power breaks inside the structures. Although the SEY characteristics of the added dielectrics allowed to think that a break would occur around these structures, the results showed that the avalanche occurred through all the structure and not in a localized environment.

V.3.1.a Size of the dielectric disk

Based on the effect of adding dielectric filling in critical areas, a more detailed study regarding the size of these dielectric fillings on the critical areas was performed. As previous results showed that the most critical region was the coupling section of the inner section of the resonators only the radius of the dielectric disc of the inner section was modified.

In terms of electrical responses of the filter, depending on the diameter of the dielectric disc, the total length of the resonator must be modified to obtain an adequate filter response on each case. The power handling simulations for these structures were performed with CST, since the meshing around the disc could be modified for a higher precision.

Two cases were evaluated for the variations on the size of these dielectric fillings. The first case corresponds to a disc smaller than the open-ended central conductor of the inner section, and the second case considers a dielectric disc bigger than the same conductor. Both cases are presented in Figure V.11 (a) and (b).

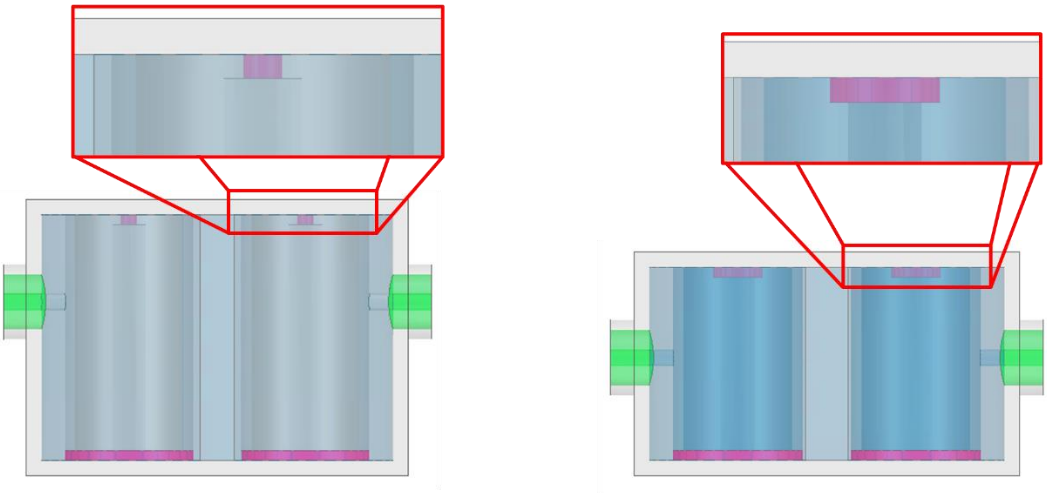

(a)

(b)

Figure V.11 Variation on the size of the dielectric disc on the open-ended area of the inner section. (a) small, (b) big.

A comparison between all the studied cases is presented in Table V.3. Here, it can be seen that the addition of a dielectric filling on the critical areas of the filter increases the power handling of the structure by replacing the critical region in vacuum-only environments. In table V.3 it is also observed that a significant improvement of 10.6 dB in the power handling of the structure occurs between the small disc and the normal disc configurations. A comparison between the normal disc and bigger disc cases showed that the increase of the power handling was only of 0.82 dB.

Table V.3 Power handling results and comparison for the 2^{nd} order filter

$\boldsymbol{Case}$	$\boldsymbol{l_\varepsilon}\ [\boldsymbol{mm}]$	$\boldsymbol{\varepsilon_r}$	$\boldsymbol{l}\ [\boldsymbol{mm}]$	$\boldsymbol{D_3}\ [\boldsymbol{mm}]$	$\boldsymbol{D_{disc}}\ [\boldsymbol{mm}]$	$\boldsymbol{Power}\ [\boldsymbol{W}]$	$\boldsymbol{Gain}\ [\boldsymbol{dB}]$
No disc	1	1	39	2.8	-	2.2	-
Small disc		9.8	27.2		1.4	5.2	3.74
Normal disc		9.8	24.2		2.8	60	14.36
Big disc		9.8	21.8		4.2	72.5	15.17

V.3.2 4th order filter

As for the carbon coating case, we wanted to determine the impact of the dielectric filling structures on filters of different orders. In this case the 4th order filter with k=1 was selected. The structure corresponds to the same filter compared to the k=3 case in Chapter IV. Alumina discs and rings were added to the coupling areas of the 4 resonators and the length was adjusted to match the correct electrical length at 1.5 GHz. A size reduction of 46.22 % was observed, going from a total heigh of the initial filter of 25.3 mm to a height of 13.46 mm for the structure with dielectric fillings. The top and side view of the resulting structure are presented in Figure V.12 (a) and (b).

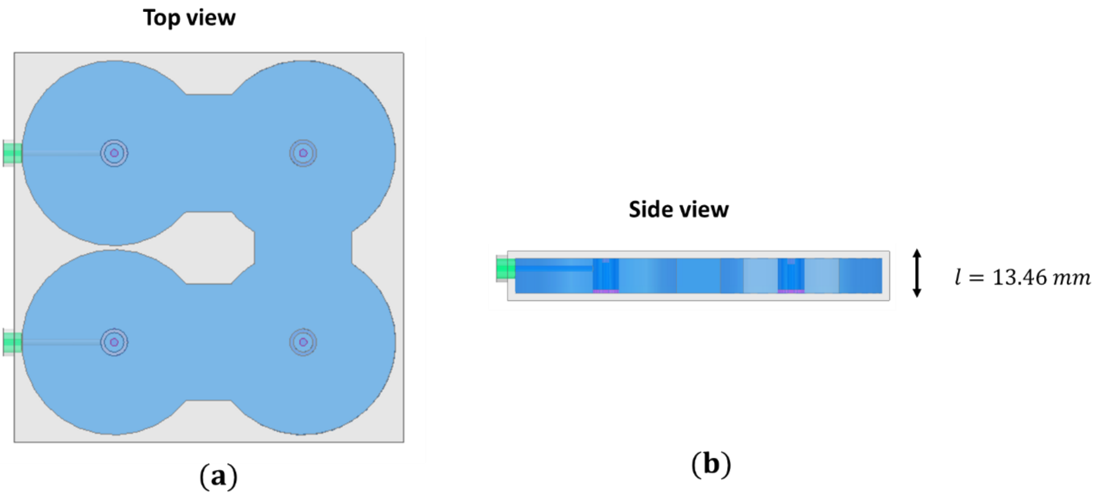

Figure V.12 Top (a) and side (b) views of the 4th order filter with dielectric fillings.

A comparison of the frequency response of the filter with and without dielectric fillings in the critical areas is presented in Figure V.13, and a comparison of the losses in the passband is also presented in Figure V.14. A difference of 0.069 dB was observed between both filters which can be explained from the size reduction of 46% and losses in the dielectric. However, the losses degradation can be considered as weak.

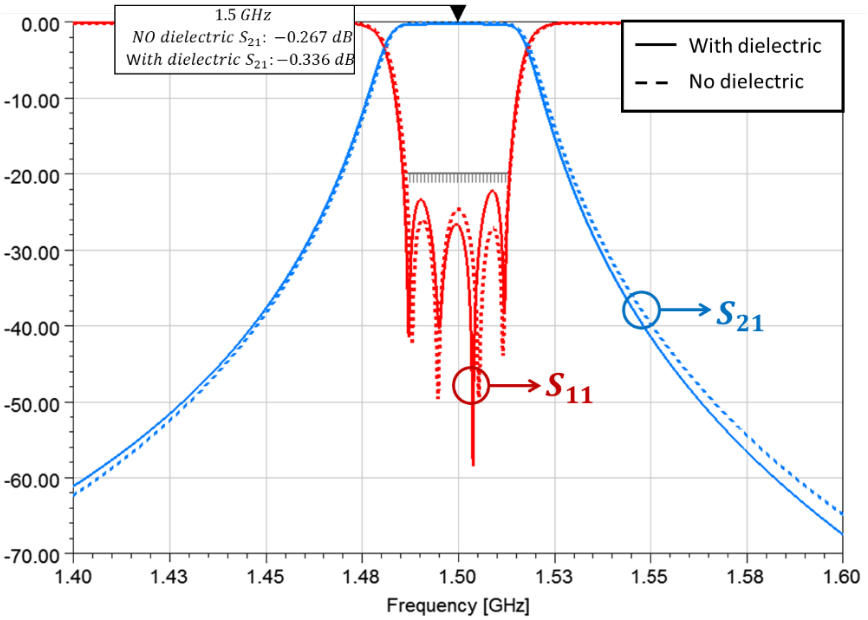

Figure V.13 4th order filter with k=1 comparison with and withoud dielectric

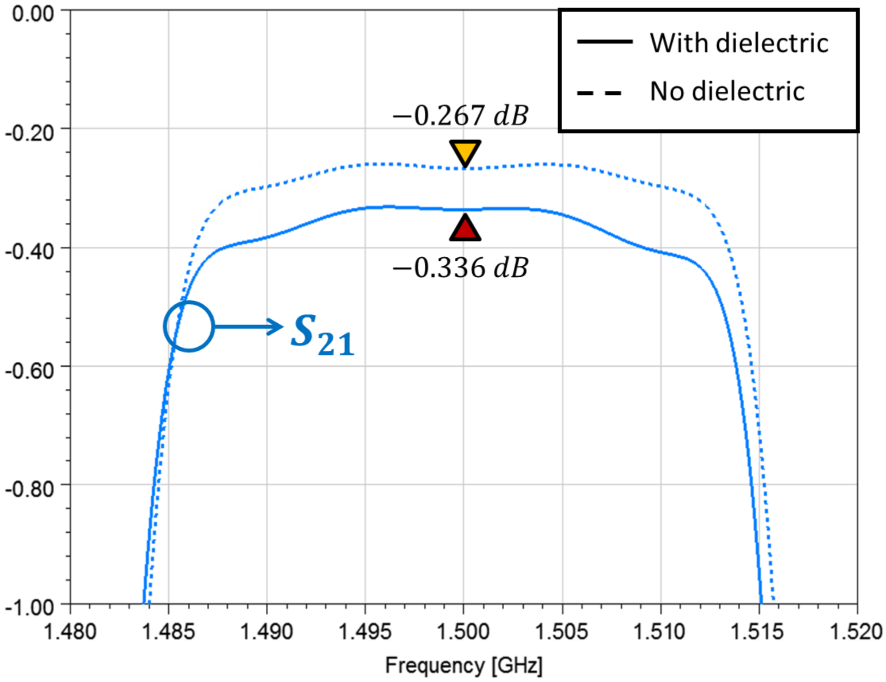

Figure V.14 Instersion loss comparison for the 4th order filter with k=1 with and withoud dielectric

In terms of power handling of both filters, the traditional filter had a maximum power handling of 2.5 W determined by CST. On the other hand, the new filter with dielectric fillings has a maximum power handling of 5.1 W also determined by PIC. Electrons tracking showed that the break on the filter with dielectric fillings occurred on the inner section of the resonators and on an uniform distribution all along the resonators as it was the case for the 2nd order filter, the images of the electron distributions inside the structure are presented in FigureV.15 and FigureV.16.

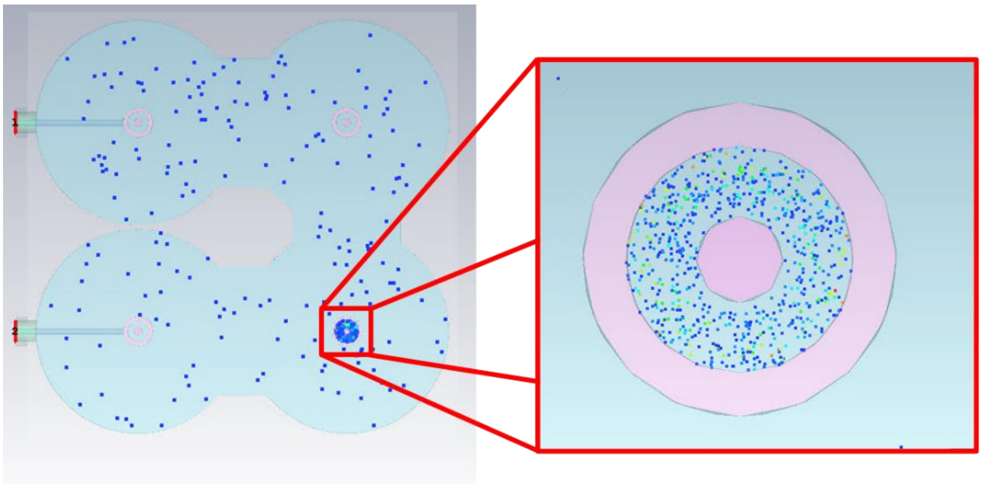

Figure V.15 Top view of the multipactor break on the 4th order filter with dielectric

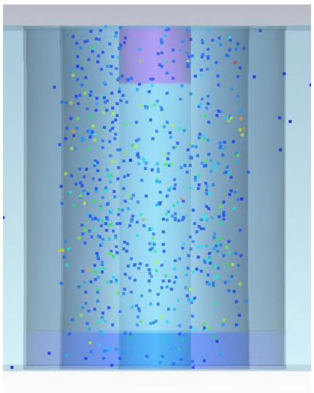

Figure V.16 Front view of the multipactor break on the 4th order filter with dielectric

V.4 Chapter V conclusion

The results presented in this chapter show the interest of using dielectric fillings inside high-power RF structures as a multipactor mitigation technique. However, more complex studies must be done since the effect of dielectric charging, and the perturbation is caused on the field between metallic conductors, were not contemplated in the simulations due the high complexity of doing so.

However, using the same simulation procedure as for structures without dielectrics, the preliminary results show that the use of dielectrics allows the size reduction of the structure maintaining similar electrical performances and comparable power handlings when compared with the traditional structures.

On the other hand, the use of dielectrics introduces some limitations as they increase the losses on the structures impeding the fulfillment of the electrical specifications, and the size reduction of the structure reduces the margin for tuning a structure.

Conclusion and Perspectives

This work presented the study of the multipactor effect on microwave filters using coaxial Stepped Impedance Resonators. In this study, a better understanding of the multipactor effect in this type of structure was obtained and a design suggestion, in terms of power, was proposed.

Also, the designed characterization structures successfully allowed the measurements of the electrical conductivity of the samples with a high precision and repeatability, with a maximum dispersion of 5.3 %. These measurements showed that the impact of these coatings does not represent a significant decrease of the samples' conductivity. In addition, since the thickness of the coatings is of 20 nm, on its thickest area, a value that is relatively thin when compared with the skin depth at 14 GHz (536 nm), the width of these coatings is not critical for the superficial losses.

On the other hand, the 20 nm thickness was enough to modify the silver SEY and reduce the number of secondary electrons of the coated samples, since this electrons' interaction occurs on the first 5 to 10 nm of the surface. In addition, the amorphous carbon coating presented not only a lower δ_{max}, but a higher first crossover energy, meaning that more energy will be needed to start an electrons avalanche, increasing the power handling of a RF structure.

In terms of power handling, the use of carbon coatings leads to an increase of the maximum power handling of all the studied structures. This increase on the power handling can be achieved either by partial of complete coatings of the structure as shown on the study made on chapter III. Being able to do partial coatings of a structure adds an additional freedom degree in the design of microwave structures.

For these coatings, further investigation on more complex 3D surfaces must be done, supported not only by simulations but by power handling measurements. Limitations like samples' shape and size and the coatings' real thickness must be solved so that the carbon coatings solution can become a repeatable and trustable procedure. Up to today, the achievement of uniform coatings over large and/or complex geometries is hard to obtain. The cost of the infrastructure for achieving the desired coatings is still elevated due to the specificity of the technological material required for this.

The novel topology with internal parallel sections and its study allows to optimize a resonator's quality factor resulting in lower insertion losses on a filter in the same form factor. With an analytical model that has good agreement with eigenmode simulations, the design and dimensioning of microwave filters with this topology is optimized and has good agreement with simulations and measurements. This topology allows the increase of the distance between metallic conductors at critical areas inside the filter, this increase results in a higher power handling of the structure. In addition, this topology allows the use of cross couplings to improve the selectivity of the electrical response of the filter.

Additionally, the apparition of parasitic resonant frequencies between the fundamental TEM resonant frequency and its first harmonic must be analyzed at a higher level of detail. Although for the filter presented on this work it was not an inconvenience, the placing of these parasitic frequencies might be useful for even more complex filtering structures.

Finally, the preliminary studies of microwave filters with dielectric fillings present encouraging results as a size reduction of the filter, increasing the maximum power handled by these devices. A deeper study of this work is proposed in order to correctly determine the impact of the fields coming from dielectric inside the structures and how the dielectric can be fully integrated to microwave filters inside critical areas.

If multipactor tests results agree with the simulation responses, a deeper development of the carbon coatings should be done. These coatings should be reproductible, and the thickness mastered at the nanoscale level, leading to uniform coating in different structures. In addition, the coating technique should allow to coat complex 3D geometries according to the different coating areas of filter topologies.

In addition, more studies, and analyses like aging, grip and thermomechanical should be done to characterize the mechanical properties of the carbon coatings. These studies could allow the technology to be space qualified and be part of the available multipactor impeaching techniques.

In the filter case, the study of new topologies with and without carbon should be done. For example, a 3 sections k=3 filter should be studied and compared to a 3 sections k=1 filter to see if the quality factor improvement in this case is also feasible. Additionally, novel solutions as the use of coaxial SIR distributed in multiple levels and more than 3 sections should be studied. Concerning the parasitic modes discussed in chapter IV, how they could be controlled and used in new innovant and exigent filtering solutions.

Annexes

Table 0.1 Conductivity estimation results for silver and carbon coating

Sample	Orientation	Q	S21 max	$\sigma_{14\,GHz}\ [MSm^{-1}]$	File_Name
Ag_1	1	14,304	-35.1154	46.6748	Ag_E1_O1_V1.S2P
	1	14,305	-35.0804	46.6891	Ag_E1_O1_V2.S2P
	1	14,415	-35.0374	48.3142	Ag_E1_O1_V3.S2P
	2	14,124	-35.3961	44.1652	Ag_E1_O2_V1.S2P
	2	14,060	-35.4061	43.3069	Ag_E1_O2_V2.S2P
	2	14,175	-35.3565	44.1759	Ag_E1_O2_V3.S2P
	3	14,103	-35.4381	43.8404	Ag_E1_O3_V1.S2P
	3	14,018	-35.4501	42.7269	Ag_E1_O3_V2.S2P
	3	14,040	-35.4353	42.9948	Ag_E1_O3_V3.S2P
	4	14,418	-34.9037	48.4051	Ag_E1_O4_V1.S2P
	4	14,329	-34.932	47.0971	Ag_E1_O4_V4.S2P
	4	14,507	-34.8814	49.7653	Ag_E1_O4_V4.S2P
Ag_2	1	14,610	-35.1029	51.4831	Ag_E2_O1_V1.S2P
	1	15,031	-35.0266	58.7304	Ag_E2_O1_V2.S2P
	1	14,613	-35.0291	51.5175	Ag_E2_O1_V3.S2P
	2	14,663	-35.0227	52.1329	Ag_E2_O2_V1.S2P
	2	14,595	-35.021	51.0418	Ag_E2_O2_V2.S2P
	2	14,527	-35.0381	49.9758	Ag_E2_O2_V3.S2P
	3	14,662	-35.065	52.1119	Ag_E2_O3_V1.S2P
	3	14,871	-35.0069	55.634	Ag_E2_O3_V2.S2P
	3	14,528	-35.0022	49.9928	Ag_E2_O3_V3.S2P
	4	14,754	-34.8898	53.8256	Ag_E2_O4_V1.S2P
	4	14,615	-34.9542	51.541	Ag_E2_O4_V4.S2P
	4	14,707	-34.9213	53.0407	Ag_E2_O4_V4.S2P
Ag_Carbon_1	1	14,302	-35.2065	46.6082	Carbon_E1_O1_V1.S2P
	1	14,390	-35.1945	47.8879	Carbon_E1_O1_V2.S2P
	1	14,367	-35.2169	47.5536	Carbon_E1_O1_V3.S2P
	2	14,586	-35.0806	51.1874	Carbon_E1_O2_V1.S2P
	2	14,475	-35.0652	49.4406	Carbon_E1_O2_V2.S2P
	2	14,475	-35.0626	49.44	Carbon_E1_O2_V3.S2P
	3	14,360	-35.19	47.7485	Carbon_E1_O3_V1.S2P
	3	14,295	-35.1911	46.79	Carbon_E1_O3_V2.S2P
	3	14,404	-35.1768	48.4054	Carbon_E1_O3_V3.S2P
	4	14,299	-35.2199	46.6585	Carbon_E1_O4_V1.S2P

Sample	**Orientation**	**Q**	**S21 max**	$\boldsymbol{\sigma_{14\,GHz}}$ $[\boldsymbol{MSm^{-1}}]$	**File_Name**
	4	14,234	-35.2521	45.7191	Carbon_E1_O4_V4.S2P
	4	14,409	-35.2087	48.2671	Carbon_E1_O4_V4.S2P
Ag_Carbon_2	1	14,427	-35.0737	48.5073	Carbon_E2_O1_V1.S2P
	1	14,504	-35.026	49.6674	Carbon_E2_O1_V2.S2P
	1	14,549	-35.0276	50.3577	Carbon_E2_O1_V3.S2P
	2	14,502	-35.0656	49.6596	Carbon_E2_O2_V1.S2P
	2	14,637	-35.0614	51.7873	Carbon_E2_O2_V2.S2P
	2	14,413	-35.0842	48.3009	Carbon_E2_O2_V3.S2P
	3	14,347	-35.1172	47.3026	Carbon_E2_O3_V1.S2P
	3	14,325	-35.124	46.9811	Carbon_E2_O3_V2.S2P
	3	14,480	-35.1063	49.283	Carbon_E2_O3_V3.S2P
	4	14,280	-35.185	46.3382	Carbon_E2_O4_V1.S2P
	4	14,412	-35.1669	48.2606	Carbon_E2_O4_V4.S2P
	4	14,258	-35.2006	46.0208	Carbon_E2_O4_V4.S2P

References

[1] G. Maral y M. Bousquet, Satellite Communications Systems. Systems, Techniques and Technology, John Wiley & Sons Ltd., 2009.

[2] P. Vallerotonda, L. Pelliccia, C. Tomassoni, F. Cacciamani, R. Sorrentino, J. Galdeano y C. Ernst, «Compact Waveguide Bandpass Filters for Broadband Space Applications in C and Ku-Bands,» de *2019 European Microwave Conference in Central Europe (EuMCE)*, 2019.

[3] E. Laplanche, N. Delhote, A. Périgaud, O. Tantot, S. Verdeyme, S. Bila, D. Pacaud y L. Carpentier, «Tunable Filtering Devices in Satellite Payloads: A Review of Recent Advanced Fabrication Technologies and Designs of Tunable Cavity Filters and Multiplexers Using Mechanical Actuation,» *IEEE Microwave Magazine,* vol. 21, nº 3, pp. 69-83, 2020.

[4] Alén Space, "A Basic Guide to Nanosatellites," [Online]. Available: https://alen.space/basic-guide-nanosatellites/. [Accessed 20 03 2022].

[5] Space Foundation, «The space briefing book,» 2019. [En línea]. Available: https://www.spacefoundation.org/briefingbook/. [Último acceso: 20 05 2022].

[6] J. Benedicto, E. Rius, J.-F. Favennec, D. Pacaud, L. Carpentier y J. Puech, «A compact L-band bandpass filter based on SIR coaxial resonators with high multipactor threshold,» *International Journal of Microwave and Wireless Technologies,* vol. 14, nº 3, pp. 270-281, 2021.

[7] European Space Agency, «TECHNOLOGY HARMONISATION DOSSIER, Power RF Measurements & Modelling,» 2021.

[8] J. Rodney y M. Vaughan, «Multipactor,» *IEEE Transactions on Electron Devices,* vol. 35, nº 7, pp. 1172-1180, July 1988.

[9] A. Iqbal, P. Y. Wong, J. P. Verboncoeur y P. Zhang, «Frequency-Domain Analysis of Single-Surface Multipactor Discharge With Single- and Dual-Tone RF Electric Fields,» *IEEE TRANSACTIONS ON PLASMA SCIENCE,* vol. 48, nº 6, pp. 1950-1958, 2020.

[10] A. Woode y J. Petit, «Diagnostic Investigations into the Multipactor Effect, Susceptibility Zone,» *ESA/ESTEC Working Paper No. 1556,* 1989.

[11] J. Rodney y M. Vaughan, «A New Formula for Secondary Emission Yield,» *IEEE TRANSACTION ON ELECTRON DEVICES,* vol. 36, nº 9, pp. 1963-1967, 1989.

[12] C. Vicente, M. Mattes, D. Wolk, B. Mottet, H. Hartnagel, J. Mosig y D. Raboso, «Multipactor Breakdown Prediction in Rectangular Waveguide Based Components,» *Microwave Symposium Digest,* pp. 1055-1058, 2005.

[13] M. Furman y M. Pivi, «Probabilistic model for the simulation of secondary electron emission,» *Physical Review Special Topics- Accelerators and Beams,* vol. 5, nº 124404, pp. 1-18, 2002.

[14] S. A. Rice y J. P. Verboncoeur, «A Comparisson of Multipactor Predictions Using Two Popular Secondary Electron Models,» *IEEE Transactions on Plasma Science,* vol. 42, nº 6, pp. 1487-1487, 2014.

[15] C. González, C. Alcaide, R. Cervera, M. Rodríguez, Ó. Monerris, J. Petit, A. Rodríguez, A. Vidal, J. Vague, J. V. Morro, P. Soto y V. E. Boria, «Multipactor Threshold Estimation Techniques Based on Circuit Models, Electromagnetic Fields, and Particle Simulators,» *IEEE Journal of Microwaves,* vol. 1, pp. 57-77, 2022.

[16] O. A. Ivanov, M. A. Lobaev y A. L. Vikharev, «Suppressing and initiation of multipactor discharge on a dielectric by an external dc bias,» *Physical Review Special Topics - accelerators and beams,* vol. 13, nº 32, 2010.

[17] A. Valfells, L. K. Ang, Y. Y. Lau y R. M. Gilgenbach, «Effects of an external magnetic field, and of oblique radio-frequency electric fields on multipactor discharge on a dielectric,» *: Physics of Plasmas,* vol. 7, pp. 750-757, 2000.

[18] D. González-Iglesias, A. M. Pérez, S. Anza, J. V. Cardona, B. Gimeno, V. E. Boria, D. Raboso, C. Vicente, J. Gil, F. Caspers y L. Conde, «Multipactor Mitigation in Coaxial Lines by Means of Permanent Magnets,» *IEEE Transactions on Electron Devices,* pp. 4224-4231, Dec 2014.

[19] V. Baglin, J. Bojko, O. Gröbner, B. Henrist, N. Hilleret, C. Scheuerlein y M. Taborelli, «THE SECONDARY ELECTRON YIELD OF TECHNICAL MATERIALS AND ITS VARIATION WITH SURFACE TREATMENTS,» de *Proceedings of EPAC*, Vienna, Austria, 2000.

[20] G. Troncoso, J. M. García-Martín, M. U. González, C. Morales, M. Fernández-Castro, J. Soler-Morala, L. Galán y L. Soriano, «Silver nanopillar coatings grown by glancing angle magnetron sputtering for reducing multipactor effect in spacecrafts,» *Applied Surface Science,* vol. 526, 2020.

[21] L. Olano, M. E. Dávila, J. M. Rojo, P. Martín-Iglesias y I. Montero, «Nanostructured Coatings of Low-Secondary Electron Emission to Avoid Multipactor Discharge in High-Power Microwave Devices,» de *IEEE MTT-S International Microwave Workshop Series on Advanced Materials and Processes for RF and THz Applications (IMWS-AMP)*, 2019.

[22] D. Wu, J. Ma, Y. Bao, W. Cui, T. Hu, J. Yang y Y. Bai, «Fabrication of Porous Ag/TiO2/Au Coatings with Excellent Multipactor Suppression,» *Scientific Reports,* vol. 7, nº 1, p. 43749, 2017.

[23] F. Cemin, Élaboration de couches minces pas HiPIMS: proprités structurales et aspects énergetiques, Paris, 2018.

[24] H. Aouidad, Etude de filtres hyperfréquences miniatures et performants sur la base de résonateurs coaxiaux, Brest: Université de Bretagne Occidentale, 2014.

[25] C. Hallet, Étude et réalisation de filtres matriochkas pour des applications spatiales, Brest: Université de Bretagne Occidentale, 2018.

[26] T. Hirano, «Relationship between Q factor and complex resonant frequency: Investigations using RLC series circuit,» *IEICE Electronics Express,* vol. 14, nº 21, pp. 1-5, 2017.

[27] O. Feuray, O. Tantot, E. Sorolla y N. Delhote, «Détermination Non Destructive de la Conductivité Electrique de Depots Conducteurs,» de *14emes Journées de Caracteérisation Microondes et Matériaux*, Calais, 2016.

[28] D. M. Pozar, Microwave Engineering, third ed., Massachusetts: John Wiley, 2005, p. 83.

[29] Breizh usinage. Groupe STIndustries, [Online]. Available: https://stiudustries.fr/.

[30] J. Benedicto, J. F. Favennec, A. Buitrago Bernal y E. Rius, «A Modelization Methodology for the Quality Factor of Quarter-Wavelength n-Section Coaxial Stepped Impedance Resonators,» *IEEE Journal of Microwaves, Submitted July 2022,* 2022.

[31] N. Marcuvitz, «Coaxial Waveguides,» de *Waveguide handbook*, Lexington, MA, Boston Technical Publishers, 1964, pp. 72-80.

[32] Y. Y. Lau, R. A. Kishek, L. K. Ang y R. M. G. a. A. Valfells, «Multipactor discharge on a dielectric,» de *IEEE International Conference on Plasma Science*, 1998.

[33] P. Vallerotond, F. Cacciamani, L. Pelliccia, F. Aquino, C. Tomassoni, P. Martìn-Iglesias y V. Tornielli di Crestvolant, «Ceramic-loaded Barrel-shaped Ku-band filter for High-power Satellite Applications,» de *IEEE MTT-S International Microwave Filter Workshop (IMFW)*, Perugia, Italy, 2021.

[34] ESA, «Anti-Multipactor Treatment for Dielectrics, Ferrite and Metals,» [En línea]. Available: https://www.esa.int/Enabling_Support/Space_Engineering_Technology/Anti-Multipactor_Treatment_for_Dielectrics_Ferrites_and_Metals. [Último acceso: 16 02 2022].

[35] I. M. Montero, L. Olano, M. Aguilera y U. Dávila, «Low-secondary electron emission yield under electron bombardment of microstructured surfaces, looking for multipactor effect suppression,» *Journal of Electron Spectroscopy and Related Phenomena,* 2019.

[36] A. Sounas, E. Sorolla y M. Mattes, «Analysis of Multipactor Effect in Coaxial Lines,» 2011.

[37] G. van Eden, D. Verheijde y J. Verhoeven, «Secondary electron emission yield measurements of dielectrics based on a novel collector-only method,» *Nuclear Instruments and Methods in Physics Research Section B: Beam Interactions with Materials and Atoms,* vol. 511, pp. 6-11.

[38] T. Hamelin, Validation d’un nouveau logiciel de simulation tridimensionnel du Multipactor, Paris: Université Paris Sud, 2015.

[39] V. Nistor, L. A. González, L. Aguilera, I. Montero, L. Galán, U. Wochner and D. Raboso, "Multipactor suppression by micro-structured gold/silver coatings for space applications," *Applied Surface Science,* pp. 445-453, 2014.

[40] E. R. a. S. Division, Space engineering Multipaction design and test, he European Space Agency for the members of ECSS, 2013.

[41] Thales Alenia Space, «"REVETEMENTS CARBONE NANOMETRIQUE POUR L’AMELIORATION DE LA TENUE EN PUISSANCE D’EQUIPEMENTS RF" L-Band Filters, Multipactor test Report,» 2022.

DOCTORAT
BRETAGNE
LOIRE / MATHSTIC

UBO
Université de Bretagne Occidentale

Titre : Revêtements carbones nanométriques pour la protection multipactor d'équipements RF embarqués dans les satellites

Mots clés : Multipactor, Revêtements carbones, Filtres RF, Résonateurs coaxiaux aux sautes d'impédance.

Résumé : Dans les communications par satellite, des nouveaux cahiers des charges avec des puissances plus élevées sont une conséquence des débits de données élevés et plusieurs utilisateurs. Tout dans des plateformes moins encombrantes et plus légères.

Un des inconvénients dans des équipements plus petits et une puissance élevée est l'effet multipactor. L'effet multipactor se présente dans le vide sous certains conditions électromagnétiques en résultant en une décharge d'électrons entre les murs métalliques des composants RF. Les décharges d'électrons peuvent endommager les différents composants et même le système complet, résultant en las mise hors du service du satellite.

Ce travail présente l'étude des revêtements nano-carbones comme solution pour empêcher l'apparition de l'effet multipactor dans des composants RF.

Les propriétés de ces revêtements, comme la conductivité électrique et l'émission secondaire d'électrons, ont été caractérisées et prises en compte dans de simulations électromagnétiques et de puissance des différents filtres hyperfréquences. Les résultats de ces simulations, ont montré l'intérêt d'utiliser ces revêtements comme stratégie pour empêcher l'apparition de l'effet multipactor.

Finalement, dans ce travail l'intégration des ces revêtements dans des diffèrent topologies de filtres a aussi été étudié et comparée.

Title : Nanoscale carbon coating for Multipactor protection of RF equipment's embedded in satellites

Keywords : Multipactor, Carbon coatings, RF filters, Coaxial Stepped Impedance Resonators

Abstract: In the field of satellite telecommunications, the requirement for an increase of transmission power is a consequence of an increase in the digital bit rates and number of users. This is also accompanied by the need of more compact devices in order to reduce the size and weight of the satellites.

The main inconvenience in high power requirements and smaller sizes is the multipactor effect. This effect is manifested in the vacuum and under certain electromagnetic conditions, resulting in an electron discharge inside the RF devices. These discharges can damage the devices and the complete system, causing the satellite to be out of service.

This work presents the study of nanoscale carbon coatings as a solution method for increasing the maximum power handling in microwave structures and particularly RF filters in Tx stage.

The nanoscale carbon coatings properties, like electrical conductivity and secondary emission yield, were characterized and integrated in RF and power simulations of different RF filters.

Results showed that these coatings are an efficient way for protecting structures from multipactor discharges.

In addition, this work considers the integration of these coatings in different filtering structures and discussed their limitations.